Thermal effects on thermoplastic composites welded joints

A physical and mechanical characterisation

Koutras, N.

DOI
10.4233/uuid:8bdf06e6-8e42-463a-af45-20a56e0e2022

Publication date
2020

Document Version
Final published version

Citation (APA)
Koutras, N. (2020). *Thermal effects on thermoplastic composites welded joints: A physical and mechanical characterisation*. [Dissertation (TU Delft), Delft University of Technology].
https://doi.org/10.4233/uuid:8bdf06e6-8e42-463a-af45-20a56e0e2022

THERMAL EFFECTS ON THERMOPLASTIC COMPOSITES WELDED JOINTS: A PHYSICAL AND MECHANICAL CHARACTERISATION

Dissertation

for the purpose of obtaining the degree of doctor
at Delft University of Technology
by the authority of the Rector Magnificus, Prof. dr. ir. T.H.J.J. van der Hagen
chair of the Board for Doctorates
to be defended publicly on
Monday, 23rd November 2020 at 10:00 hours

by

Nikolaos KOUTRAS

Master of Science in Engineering
Polymer and Polymer Composite Science and Engineering,
The University of Sheffield, United Kingdom
born in Patra, Greece

This dissertation has been approved by the promotors.

Composition of the doctoral committee:

Rector Magnificus	Chairperson
Prof.dr.ir. R. Benedictus	Delft University of Technology, promotor
Dr. I. Fernandez Villegas	Delft University of Technology, promotor

Independent members:

Prof. dr. ir. K.M.B. Jansen	Delft University of Technology
Prof. dr. A. Maffezzoli	University of Salento, Italy
Prof. dr. ir. L.E. Govaert	University of Twente
Prof. dr. P. Weaver	University of Bristol, United Kingdom
Prof. dr. C. Bisagni	Delft University of Technology, reserve member

Dr. R.M. Groves of Delft University of Technology, has, as supervisor, contributed significantly to the preparation of this dissertation.

This research was part of the Thermoplastic Affordable Primary Aircraft Structure 2 (TAPAS 2) project, supported by the Netherlands Enterprise Agency of the Ministry of Economic Affairs.

Keywords:	Thermoplastic composites, Temperature, Resistance welding, Ultrasonic welding, Crystallinity, PPS
Printed by:	Ipskamp Printing (http://www.ipskampprinting.nl/)
Front cover:	Fracture surface of polyphenylene sulphide after lap shear testing of an ultrasonically welded carbon fibre polyphenylene sulphide joint. The image was taken using a scanning electron microscope. Thesis cover design by Didem Yerli.

ISBN: 978-94-6421-144-3

An electronic version of this dissertation is available at
http://repository.tudelft.nl/

Life would be tragic if it weren't funny.

(Stephen Hawking)

Summary

The use of high performance thermoplastic composites (TPCs) in the aviation industry has increased over the last years. TPCs have significant advantages such as superior damage tolerance, excellent chemical resistance and the ability to be welded. To date, mechanical fastening, primarily, and adhesive bonding are the two traditional joining methods used in aviation industry. However, welding of TPCs has attracted significant attention due to its advantageous qualities such as the very short cycle times and the minimised stress concentrations. Most of the research published on welding of TPCs concerns process optimization and the evaluation of the mechanical performance at room temperature (RT) conditions. However, aircraft operate in a wide range of temperatures, typically between -50 °C to 70 °C and depending on the conditions, even up to 93 °C. Considering the temperature dependency of polymer composites properties, the weld performance of TPCs at low and high temperatures needs to be addressed. To the author's knowledge, prior to the year 2014 there was no available literature assessing the influence of temperature on the mechanical performance of TPCs welded joints and since then, only a few publications have addressed this topic. The primary objective of this thesis was to not only fill the literature gap but also to obtain deeper knowledge and clear understanding of the behaviour of thermoplastic composites welded joints at low and high temperatures. In other words, to understand the phenomena dictating the weld performance which, in turn, would pave the way for further improvement of material properties and weld design.

This thesis presented a fully experimental work on the influence of temperature on the mechanical performance of TPCs welded joints. The work was carried out on two of the most promising welding techniques, namely resistance welding and ultrasonic welding. The heating element used in resistance welding was a stainless steel mesh. The polymer matrix was polyphenylene sulphide (PPS) while glass fibres (GF) and carbon fibres (CF) prepregs were used to produce GF/PPS and CF/PPS composites, which were used in resistance welding and ultrasonic welding, respectively. The mechanical performance was investigated by performing lap shear tests on single lap joints at various temperatures ranging between -50 °C and 150 °C. The mechanical tests were complemented by detailed fractographic inspection which provided important information on the failure mechanisms of the welded joints. Extensive thermal analysis was also performed in order to elucidate the effects of temperature on the weld performance. Furthermore, considering the very fast cycle times of the ultrasonic welding process, the crystallinity at the weldline of the ultrasonically welded CF/PPS joints was investigated. Fast Scanning Calorimetry (FSC) was employed in order to investigate the crystallinity dependency on the cooling rates. Nanoindentation measurements were also carried out in order to evaluate the modulus and the hardness of PPS at the weldline as well as at the resin rich areas of the CF/PPS adherends. Thanks to the methodology followed in this research, the mechanical performance of both resistance welded (RW) and ultrasonically welded (UW) joints was possible to be correlated to the properties of both weldline and adherends.

The lap shear strength (LSS) of RW GF/PPS joints decreased with increasing temperature, except for the region between 50 °C and 90 °C where it remained constant. The effect was found to be more significant above the glass transition temperature (Tg) of PPS. Fibre/matrix debonding was identified as the main failure mechanism at all temperatures while the connection between the heating element and the matrix was not the weakest link at the weldline. Fibre/matrix interfacial strength was identified as the main factor affecting the LSS

of RW GF/PPS joints and it was found that the fibre/matrix interfacial strength diminished with increasing temperatures.

The effect of the ultrasonic welding process on the crystallinity degree of PPS at the weldline was investigated with respect to welding force and vibration amplitude. It was demonstrated that the fast welding process, using high welding force and high vibration amplitude, yielded predominantly amorphous PPS. Using low welding force and low vibration amplitude resulted in a slower welding process and yielded PPS of moderate crystallinity and of higher modulus and hardness. Yet, the cooling rates of the slow welding process were still very high. It was suggested that despite the very high cooling rates, which in quiescent conditions would have suppressed crystallization according to the FSC measurements, PPS was probably able to crystallize due to the very high strain rates occurring during ultrasonic welding. This phenomenon, known as strain-induced crystallization, would orient the molecular chains in the melt and favour the formation of nuclei.

The mechanical performance of UW CF/PPS joints was studied on three series of varying crystallinities at the weldline, at temperatures ranging from -50 °C to 120 °C. The first (as-welded) series consisted of predominantly amorphous PPS, the second (as-welded) series consisted of PPS of moderate crystallinity and the third series consisted of PPS of the highest possible crystallinity (obtained via annealing). The overall trend of the lap shear tests was decreasing LSS with increasing temperature with the exception of two temperature regions, -50 °C to 50 °C for the annealed series, and 90 °C to 120 °C for the two as-welded series, where the LSS remained fairly constant. As in the case of RW GF/PPS joints, the temperature was found to have a more pronounced effect above the Tg of PPS. Between RT and 70 °C the differences in LSS among the three series were not significant. The main failure mechanism of both as-welded series above RT was identified as fibre/matrix debonding, which became more pronounced with increasing temperature. At -50 °C their failure mechanism was primarily matrix fracture. The annealed series also exhibited fibre/matrix debonding as a failure mechanism but mainly at elevated temperatures. The results indicated that at temperatures at and above the Tg of PPS, higher degree of crystallinity at the weldline would be beneficial for the LSS due to the higher fibre/matrix interfacial strength compared to amorphous PPS. On the contrary, at -50 °C the higher toughness and ductility of amorphous PPS would be advantageous for the mechanical performance.

This research also allowed for a comparison between the two welding techniques to take place as well as between GF/PPS and CF/PPS composites. The LSS of welds produced with ultrasonic welding, either with amorphous or with semi-crystalline weldline, were consistently higher than the welds produced with resistance welding, independently of the testing temperature. With respect to the composites comparison, it was suggested that the higher interfacial strength between CF and PPS compared to the one of GF and PPS was the main reason for the higher LSS of the UW CF/PPS joints.

In conclusion, this thesis was able to establish a qualitative relationship between the weld strength, the failure mechanisms and the constituents of the joints, namely the fibres, the thermoplastic matrix and the weldline.

Samenvatting

Het gebruik van high-performance thermoplastische composieten (TPC'en) in de luchtvaartindustrie is de afgelopen jaren toegenomen. TPC'en hebben significante voordelen: superieure schade tolerantie, excellente chemische weerstand en mogelijkheid om gelast te worden. Tot op heden zijn voornamelijk mechanische, maar ook verlijmde verbindingen de traditioneel gebruikte verbindingsmethodes in de luchtvaartindustrie. Echter, het lassen van TPC'en heeft veel aandacht getrokken door zijn gunstige eigenschappen zoals een zeer korte doorlooptijd en de minimale spanningsconcentraties. Het meeste onderzoek gepubliceerd over het lassen van TPC'en gaat over procesoptimalisatie en de evaluatie van de mechanische eigenschappen bij condities op kamertemperatuur (KT). Vliegtuigen opereren echter in een brede temperatuur range, typisch tussen de -50 °C en 70 °C en afhankelijk van de condities zelfs tot 93 °C. Met inachtneming van de temperatuursafhankelijkheid van polymeer composieten eigenschappen is het nodig om aandacht te besteden aan de eigenschappen van TPC-lassen bij lage en hoge temperaturen. Naar het beste weten van de auteur, was er voor het jaar 2014 geen literatuur beschikbaar waarin de invloed van temperatuur op de mechanische eigenschappen van TPC-lassen werd geëvalueerd. Enkel een paar publicaties hebben dit onderwerp aangestipt. Het hoofddoel van dit proefschrift was niet alleen om deze literatuurkloof te dichten, maar ook om een dieper inzicht en een beter begrip te krijgen van het gedrag van gelaste thermoplastische composieten verbindingen bij lage en hoge temperaturen. In andere woorden, om de fenomenen te begrijpen die de laseigenschappen dicteren en op hun beurt de weg zullen wijzen voor verdere verbeteringen van de materiaaleigenschappen en het ontwerp van de las.

Deze thesis presenteerde een volledig experimenteel werk over de invloed van temperatuur op de mechanische eigenschappen van de TPC gelaste verbindingen. Het werk was uitgevoerd voor twee van de meest veelbelovende lastechnieken, namelijk weerstand lassen en ultrasoon lassen. Voor het weerstand lassen werd een roestvrijstalen gaas als verwarmingselement gebruikt. Prepregs met een polymeermatrix van polyfenyleensulfide (PPS) in combinatie met glasvezel (GF) en koolstofvezel (CF) werden gebruikt om GF/PPS- en CF/PPS-composieten te maken. Deze werden respectievelijk gebruikt voor het weerstand lassen (RW) en ultrasoon lassen (UW). De mechanische eigenschappen waren onderzocht door het uitvoeren van afschuiftesten van enkelvoudig overlappende verbindingen bij verschillende temperaturen variërend tussen de -50 °C en 150 °C. De mechanische testen werden aangevuld met een gedetailleerde breukvlakinspectie, hetgeen belangrijke informatie verschafte over de faalmechanismen van de lasverbindingen. Uitgebreide thermische analyses waren uitgevoerd om de effecten van de temperatuur op de laseigenschappen te verhelderen. Daarnaast was, gezien de zeer snelle procestijd van het ultrasoon lassen, de kristalliniteit van de lasnaad onderzocht van de ultrasoon gelaste CF/PPS-verbindingen. Snel scannende calorimetrie (FSC) was gebruikt om de afhankelijkheid van de koelsnelheden op de kristalliniteit te bepalen. Nano-indentatie-experimenten werden uitgevoerd om ook de modulus en de hardheid van zowel de PPS in de lasnaad als de PPS in de harsrijke gebieden van het CF/PPS-composiet zelf te bepalen. Dankzij de methodologie gevolgd in dit onderzoek, konden de mechanische eigenschappen van zowel ultrasoon als weerstand gelaste verbindingen worden gerelateerd aan de eigenschappen van de lasnaald en het gelaste composiet zelf.

De overlap afschuifsterkte (LSS) van RW CF/PPS-verbindingen nam af met een toenemende temperatuur, behalve binnen de range van 50 °C tot 90 °C waar het gelijk bleef. Het effect was significanter bevonden boven de glastransitietemperatuur (Tg) van PPS. Het onthechten van

vezel en matrix was geïdentificeerd als het hoofdzakelijke faalmechanisme bij alle temperaturen, terwijl de verbinding tussen het verwarmingselement en de matrix niet de zwakste schakel was in de lasnaad. De vezel/matrix grensvlakstrekte was geïdentificeerd als de voornaamste factor die invloed had op de LSS van RW GF/PPS-verbindingen en het was geconstateerd dat de vezel/matrix grensvlaksterkte afnam bij toenemende temperaturen.

Het effect van het ultrasone lasproces op het percentage kristalliniteit van PPS in de lasnaad was onderzocht voor de laskracht en de amplitude van de vibraties. Het was aangetoond dat een snel lasproces, gebruikmakende van een hoge laskracht en lage amplitude voor de vibraties, resulteerde in hoofdzakelijk amorf PPS. Een lage laskracht in combinatie met een lage amplitude voor de vibraties resulteerde in een langzamer lasproces dat resulteerde in PPS met een matige kristalliniteit en een hogere modulus en hardheid. Echter, de koelsnelheden waren nog steeds zeer hoog. Er was voorgesteld dat ondanks de zeer hoge koelsnelheden, die in een ongestoorde conditie de kristallisatie zouden hebben onderdrukt volgens FSC-metingen, de PPS waarschijnlijk instaat was te kristalliseren door de zeer hoge reksnelheden die behaald werden tijdens het ultrasoon lassen. Dit fenomeen, bekend als door rek geïnduceerde kristallisatie, zou de molecuulketens in de smelt oriënteren ten gunste van nuclei formatie.

De mechanische eigenschappen van UW CF/PPS-verbindingen waren bestudeerd bij temperaturen tussen -50 °C en 120 °C voor drie series met een variërende kristalliniteit van de lasnaad. De eerste (als-gelast) serie bestond voornamelijk uit amorf PPS, de tweede serie (als-gelast) bestond uit PPS met een matig percentage kristalliniteit, de derde serie bestond uit PPS met de hoogste mogelijke kristalliniteit (verkregen door temperen). De algemene trend van de afschuiftesten van de enkelvoudig overlappende verbindingen was een afnemende LSS voor een toenemende temperatuur met uitzonderingen waarbij de LSS redelijk constant bleef: de getemperde serie bij het temperatuursgebied tussen 50 °C en 90 °C en voor de twee als-gelaste series bij het temperatuursgebied van 90 °C tot 120 °C. Net zoals in het geval bij de RW GF/PPS verbindingen, had de temperatuur een prominenter effect boven de Tg van PPS. Tussen RT en 70 °C waren de verschillen in LSS tussen de series onderling niet significant. Het hoofdzakelijke faalmechanisme van beide als-gelaste series boven RT was geïdentificeerd als het onthechten van vezel en matrix, hetgeen nog duidelijker werd met een toenemende temperatuur. Bij -50 °C was het voornaamste faalmechanisme het breken van de matrix. De getemperde serie had ook het onthechten van vezel en matrix als voornaamste faalmechanisme, maar met name bij verhoogde temperaturen. De resultaten duidden aan dat bij temperaturen bij en boven de Tg van PPS een hoger percentage kristalliniteit in de lasnaad gunstig zou zijn voor de LSS door de hogere vezel/matrix grensvlaksterkte in vergelijking met amorf PPS. Integendeel, bij – 50 °C zou de hogere taaiheid en ductiliteit van de amorfe PPS voordelig zijn voor de mechanische eigenschappen.

Dit onderzoek maakte het ook mogelijk om zowel twee lastechnieken als om CF/PPS- en CF/PPS-composieten te vergelijken. De LSS van de lassen geproduceerd met ultrasoon lassen, zowel met een amorfe als met een semi-kristallijne lasnaad, waren onafhankelijk van de test temperatuur consistent hoger dan de lassen geproduceerd met weerstand lassen. Voor de vergelijking tussen de composieten, was de hogere grensvlaksterkte tussen de CF en de PPS ten opzichte van de GF en PPS voorgesteld als de voornaamste reden voor de hogere LSS van de UW CF/PPS-verbindingen.

Samenvattend, deze thesis maakte het mogelijk om een kwalitatieve relatie tot stand te brengen tussen de lassterkte, de faalmechanismen en de componenten van de verbindingen, namelijk de vezels, de thermoplastische matrix en de lasnaad.

Contents

Nomenclature

List of symbols

A_c	*Projected area of the indenter tip*	nm^2
E	*Elastic modulus*	Pa
E'	*Storage modulus*	Pa
E''	*Loss modulus*	Pa
F	*Force*	N
G_{IC}	*Mode-I critical strain energy release rate*	J/m^2
H	*Hardness*	Pa
h	*Indentation displacement*	nm
m	*Mass*	g
T	*Temperature*	$°C$
Tg	*Glass transition temperature*	$°C$
t_r	*Reptation time*	s
X_C	*Degree of crystallinity*	$\%$
ΔCp	*Specific heat capacity*	$J/(g·°C))$
ΔH	*Melting enthalpy*	J
ΔH_C	*Specific energy associated with cold crystallization*	J/g
ΔH_f^0	*Specific melting enthalpy of an ideal crystal*	J/g
ΔH_m	*Specific melting enthalpy*	J/g
θ	*Bragg angle*	$°$

Acronyms

3PB	*Three-point bending*
AMR	*Amorphous*
ANN	*Annealed*
ASW	*As-welded*
CF	*Carbon fibre*
CFRP	*Carbon fibre reinforced polymers*
CO_2	*Carbon dioxide*
CON	*Conditioned*
CoV	*Coefficient of variation*
CSM	*Continuous stiffness measurement*
CTE	*Coefficient of thermal expansion*
DMA	*Dynamic mechanical analysis*
DSC	*Differential scanning calorimetry*
ED	*Energy directors*
ETC	*Embedded thermocouple*
FSC	*Fast scanning calorimetry*
GF	*Glass fibre*

HAZ	*Heat affected zone*
HDPE	*High density polyethylene*
IFSS	*Interfacial shear strength*
IPS	*In-plane shear*
LSS	*Lap shear strength*
PEEK	*Poly ether ether ketone*
PEI	*Polyetherimide*
PEKK	*Poly ether ketone ketone*
PPS	*Polyphenylene sulphide*
Ref	*Reference*
RT	*Room temperature*
RW	*Resistance welded*
SEM	*Scanning electron microscope*
SLS	*Single lap shear*
TMA	*Thermomechanical analysis*
TPCs	*Thermoplastic composites*
UW	*Ultrasonically welded*
WAXD	*Wide-angle X-ray diffraction*
WWII	*World war II*
ΔT	*Temperature gap between stress-free temperature and test temperature*

List of figures

1 Introduction

The Earth wanted plastic for itself.
Didn't know how to make it. Needed us.

(George Carlin)

Materials development and materials processing are amongst the oldest forms of science and engineering disciplines. Materials have been instrumental in the development of new technologies and in the progress of civilisation. Metals, glasses and clay-based ceramics were materials commonly used in early civilisations [1]. For example, joining of metals was a technology already used in the Bronze Age, while a recent study reported that 5000 year old Egyptian iron beads were made from meteoritic iron and formed into shape by carefully hammering the metal [2]. One of the most commonly used class of materials that play a crucial role in our daily lives are polymers. Polymers derive their name from the Greek words "πολύ" (poly meaning "many") and "μέρος" (meros meaning "part"), essentially meaning a material consisting of many parts. Polymers consist of repeating long chain molecules of very high molecular weight, which has granted them the term "macromolecules" [3]. The term was proposed in the 1920s by Hermann Staudinger against the common theory at that time that polymers were substances of low molecular weight, held together through physical interactions between the small molecules [3][4]. Polymers can be found in nature and typical examples are cellulose, proteins and even our own complex molecule that contains our genetic code and the information needed to build and reproduce, the deoxyribonucleic acid (DNA). However, the polymers that dominate our daily lives today are synthetic polymers (or so-called "man-made polymers") and have been around for not more than two centuries. The inventions of Bakelite (by Leo Baekeland in 1909) and Nylon (by Wallace Carothers in 1935) were pivotal in the field of Polymer Science and Engineering, as both materials found use in many applications, pushing the Chemical Industry to invest more in the research and development of new polymers. As with many technological innovations that shaped the world in the 20th century – notoriously in the chemical industry – the outbreak and aggression of World War II (WWII) played an instrumental role in the development and production of polymers. A typical example of polymer application in WWII was the use of nylon in parachutes and ropes. Since then, numerous new polymers have been invented and implemented in many technological innovations. The two main categories of synthetic polymers are thermoplastics and thermosets. Thermosets are polymers that harden and solidify above a critical temperature. This irreversible phenomenon is known as curing and can be promoted by curing agents. The main characteristic of a thermoset is that during curing it forms chemical cross-links, hence, it cannot be reformed and reversed back to its initial state. Epoxies and vinylesters are typical examples of thermosets. Thermoplastics on the other hand, are polymers that become soft and flow above a critical temperature and solidify during cooling. The main characteristic of a thermoplastic is that it can be reformed by simply heating the polymer up to a critical temperature (softening or melting temperature) and then, of course, cool down and solidify. Typical examples of thermoplastics are polyolefins (such as polypropylene), polyamides (such as nylon) and polyketones (such as polyetheretherketone).

The extensive research and enormous success in the field of polymers during the previous century resulted in the emergence of a new class of materials, called fibre reinforced polymers, commonly known as polymer composites. Fibre reinforced polymers consist of a polymer which acts as the matrix and fibres which act as the reinforcement, usually glass fibres (GF) or carbon fibres (CF). The role of the fibres is to increase the strength and stiffness of the material and the role of the matrix is to support the fibres and transfer the load among them. Furthermore, fibre reinforced polymers possess superior specific properties due to their low density, in other words very high strength and modulus to weight ratio [5][6], especially when compared to steel or aluminium, establishing them as high-performance lightweight materials. Owing to their lightweight nature and attractive properties such as excellent fatigue performance and corrosion resistance [5], fibre reinforced polymers are being used in many sectors such as automotive, building and infrastructure, renewable energy, marine, oil and gas, and aerospace [5][7]. Both thermoplastics and thermosets are used as matrix in polymer composites, depending on the requirements and cost of the application.

1.1 Polymer composites in aerospace

In the aerospace industry, the interest in polymer composites started primarily post WWII in order to develop lightweight materials that could replace metals without compromising the mechanical performance of the aircraft. Already in the 1940s, the aerospace industry envisioned the use of fibre reinforced polymers in airplanes. An article of *Popular Mechanics* journal in 1943 [7][8], quoted H.D. Hoekstra from the Civil Aeronautics Administration: "*Airplanes weighing as much as one and one-third million pounds are deemed possible*". Hoekstra stated that the use of glass fibre reinforced plastics in aircraft could be possible. And it was. Not only glass fibre but mainly carbon fibre reinforced polymers (CFRP), as soon as industrial carbon fibre production became a reality. The first substantial use of fibre reinforced polymers took place in the 1970s by both Airbus and Boeing. The Airbus A300 featured spoilers and rudders made of CFRP [9] while the Boeing 737 featured spoilers made of CFRP [10]. The use of polymer composites in aerospace industry steadily increased through the 1980s and 1990s (Figure 1.1), reaching 15% in A320 in mid 1980s [9][11]-[13].

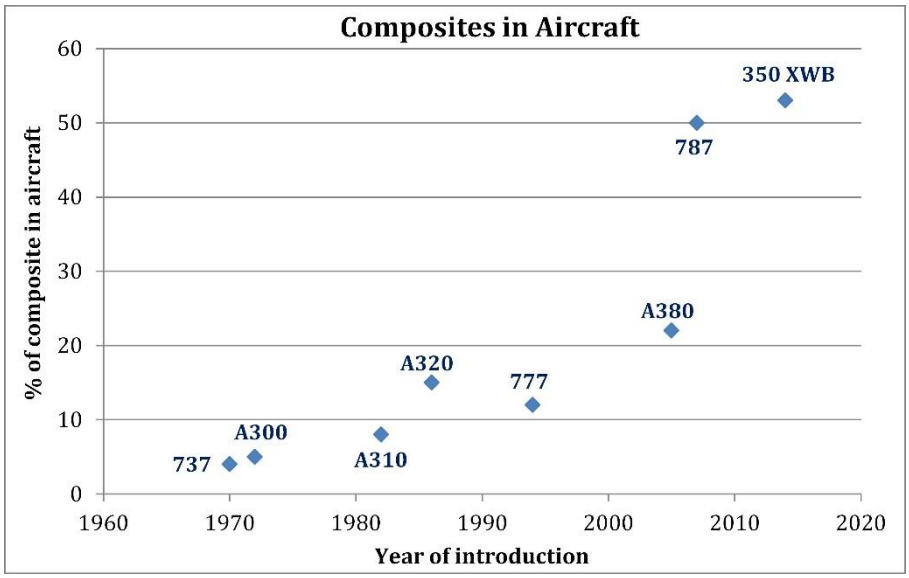

Figure 1.1. Use of polymer composites in aircraft over the last 50 years. Data taken from several sources [9][11]-[14].

Since the year 2000, the use of polymer composites in aviation increased significantly, reaching 50% in the 787 in 2007 [13] and 53% in the A350 XWB (Figure 1.2) in 2014 [14]. In fact, the wing of the Airbus A350 XWB is the largest single aviation structure ever made out of fibre reinforced polymer, and is about 32 metres long and 6 metres wide [15]. Although fibre reinforced polymers are materials with very attractive properties and have an increased design freedom allowing engineers to use the materials' full potential, the aviation industry is also keen on increasing the use of these lightweight materials to reduce the net aviation carbon dioxide (CO_2) emissions. By 2050 the goal is to reduce the net aviation CO_2 emissions by half of what they were in 2005 [16] and, right now, aircraft weight reduction seems as one of the most efficient ways of achieving such goal.

Figure 1.2. Airbus A350-900 (A350 XWB family).

Thermosets – mainly epoxy resins – are predominantly utilised as the polymer matrix in aircraft structures instead of thermoplastics; the existing knowledge database, ease of processing and substantial investment over the years are the drivers for the higher use of thermoset matrices in aircraft applications. However, over the last years, several companies and research centres have developed and produced structures from thermoplastic composites (TPCs) utilising high-performance thermoplastics (Figure 1.3). The most frequently studied high-performance thermoplastics are PEEK (Poly ether ether ketone), PEKK (Poly ether ketone ketone), PPS (Polyphenylene sulphide), and PEI (Polyetherimide). Thermoplastics offer several advantages over thermosets such as higher toughness, high damage tolerance, solvent resistance, "infinite" shelf-life, and recyclability [17][18]. Furthermore, the ability of thermoplastics to be re-melted and re-shaped through heating and cooling cycles, allows thermoplastic composites (i) to be produced in fast, cost- and energy-efficient processes (such as press consolidation instead of autoclave consolidation), (ii) to be joined together through fast, cost- and energy-efficient manufacturing technologies such as welding and (iii) to be recycled, which is greatly desired in the constant strive for sustainability of today's world. Joining of polymer composites is of significant importance in the manufacturing of aerospace structures since the production of large and complex structures in a single processing step is difficult. Welding of thermoplastic composites seems to fulfil the requirements of a reliable, automated and cost-efficient joining method in order to produce lighter components with high performance, in short production times [19][20]. The reader is referred to section 1.3 for a summary of the advantages of welding over the traditional joining techniques.

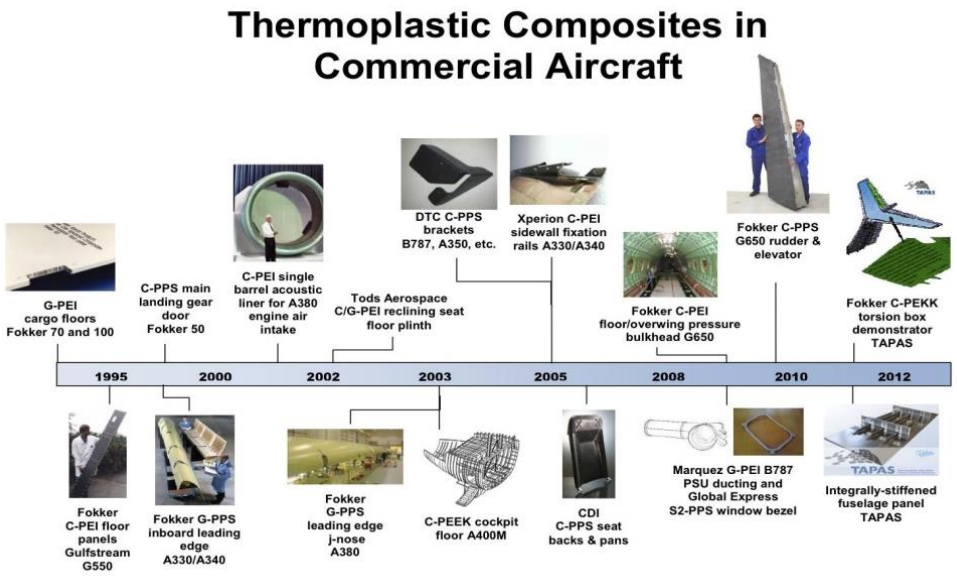

Figure 1.3. Use of thermoplastic composites in aerospace (reproduced from [21]).

1.2 Joining methods: Traditional ways

The two traditional joining techniques for polymer composites that are currently used in aircraft structures are mechanical fastening and adhesive bonding [22].

Mechanical fastening (i.e. riveting and bolting) is the traditional joining method that is primarily used in the aerospace industry. Process simplicity, through-the-thickness reinforcement, joining of dissimilar materials and capability for disassembly are some of its main advantages [22]. However, mechanical fastening can introduce several problems into a polymer composite structure such as stress concentrations, delaminations, additional weight, extensive labour, galvanic corrosion of fasteners due to differences in anodic index, and coefficient thermal expansion (CTE) mismatch between the composite structure and the fastener [22]. It is important to note that holes weaken the composite structures due to stress concentrations, making aerospace engineers to typically overdesign the composite structures, locally adding more layers to compensate for the reduction in mechanical properties. The direct consequence of this is weight increase which can be substantial. The second technique, adhesive bonding, can minimise stress concentrations, it is capable of joining dissimilar materials and has superior fatigue resistance [23]. However, adhesive bonding exhibits considerable disadvantages as well, such as sensitivity to contamination from chemicals like release agents and machining oils, which can have a detrimental impact on the bond strength, extensive surface preparation, and long curing times [19][23][24]. In addition, high-performance thermoplastics such as PPS are difficult to be bonded using adhesives due to their low surface energy [25].

Hence, it becomes clear that the development of a technique that can eliminate or minimise the aforementioned problems is one of the primary goals of the aviation industry. As mentioned in the previous section, thermoplastic polymers have the ability to be re-melted and re-shaped, allowing TPCs to be welded. Welding is a joining method that can form a consolidated joint between two parts, simply by melting locally both of the parts through heat and then cooling the joint under pressure. The next section lists the main advantages and disadvantages of welding and explains the principles of the technique.

1.3 Welding of thermoplastics composites

Although welding of thermoplastics has been in use for almost as long as thermoplastics have been used, welding of TPCs has not so commonly been used. However, over the last decades welding of TPCs has attracted an increasing interest from academia and industry since it brings several advantages that can minimise the majority of the weaknesses of mechanical fastening and adhesive bonding. The main advantages of welding are [19][26]:

a. Very short cycle times
b. Minimised stress concentration
c. Minimised labour
d. Minimal surface preparation of the substrates

However, as with every material, every process and every experimental method, there are some disadvantages:

a. Welding of dissimilar materials is most of the times not possible, although, recent studies undertaken in the welding group of I.F. Villegas at TU Delft, have shown that welding of thermosets to thermoplastics is possible [27]-[29].
b. Disassembly is not yet possible (one of the main advantages of mechanical fastening over adhesive bonding and welding).
c. The weldline properties might differ compared to the bulk of the adherends, depending on the process speed and type of material.

Nevertheless, welding offers promising joining solutions to many problems while research and development in the field of welding can eliminate some of the current disadvantages. In order to understand how welding works, a brief explanation of the principles of "Theory of Healing" and the formation of polymer-polymer interfaces follows below. An important point to be made here is that the theory of healing applies to any form of thermoplastic consolidation and not only to welding. For example, press consolidation of TPC relies on the same principles.

Healing at a polymer-polymer interface essentially means "interdiffusion of chains across the interface". R.P. Wool and co-workers published a series of articles on the theory of healing in polymers more than 30 years ago [30]-[32]. They described the process in five sequential stages:

i. Surface rearrangement
ii. Surface approach
iii. Wetting
iv. Diffusion
v. Randomisation

By heating the polymer above its glass transition temperature, the molecular chains become mobile and start to rearrange. Chain end distributions and molecular chains orientation are some of the "changes" occurring near the heated surface of the polymer and these changes intensify at higher temperatures. However, surface rearrangement will not be effective if there is no contact with another surface otherwise the molecules can diffuse back to the bulk polymer/laminate. Following surface approach, wetting of the two surfaces should take place in order to form an interface. It is important to remember that wetting does not happen instantaneously at every location due to surface asperities, uneven thickness, etc. Wetting itself cannot form a strong polymer-polymer interface as the latter requires interdiffusion of

molecular chains across the interface. When the wetting stage is completed, intimate contact between the two surfaces is achieved. The potential barriers at the interface are eliminated and the molecular chains can move freely across the interface in the stages of diffusion and randomisation. The process of interdiffusion relies on the reptation theory which can describe the chain motions in a polymer-polymer interface. In thermoplastics, there are considerable restrictions in chain motions due to the physical entanglements of neighbouring polymer chains. In Figure 1.4 the concept of the "tube-like" region is illustrated: a polymer chain is entangled with many neighbouring chains resulting in topological constraints in its motion which is represented by the tube. Initially, the chain is inside the tube, taking the tube's shape. During the interdiffusion process, segments of the polymer chain "escape" from the initial tube and, eventually, when the reptation time has elapsed ($t=t_r$), the chain has erased its initial conformation. The key aspect of healing (or welding as it is the main topic of this study) is that intimate contact needs to be achieved between the two surfaces and the healing time (or welding time) should be longer than the intimate contact time in order to obtain optimum weld strength. Figure 1.5 illustrates a simplified schematic representation of chain motions across a polymer-polymer interface.

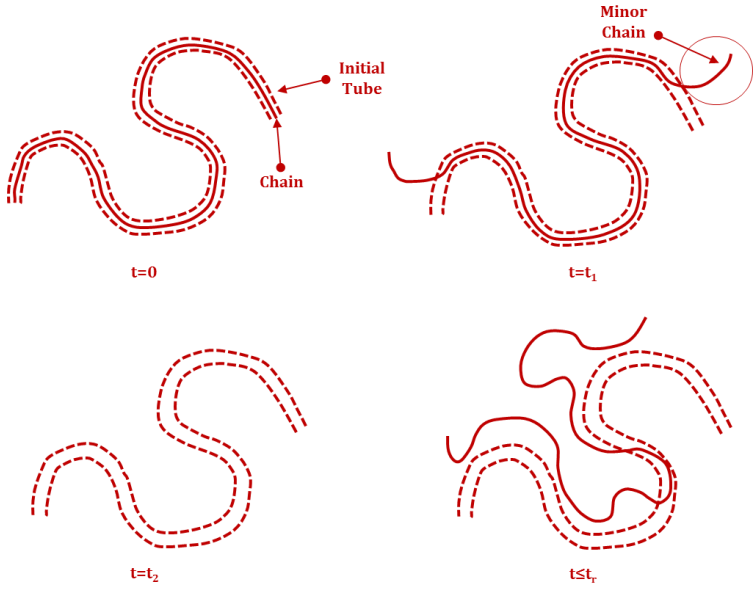

Figure 1.4. Schematic representation of the reptation model for the disentanglement of a polymer chain from its initial tube. tr is the reptation time. The schematic is adapted from [31].

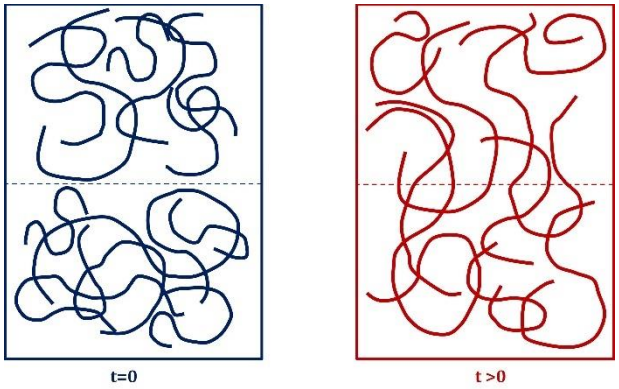

Figure 1.5. Simplified representation of molecular chains interdiffusion across a polymer-polymer interface. The schematic is adapted from [31].

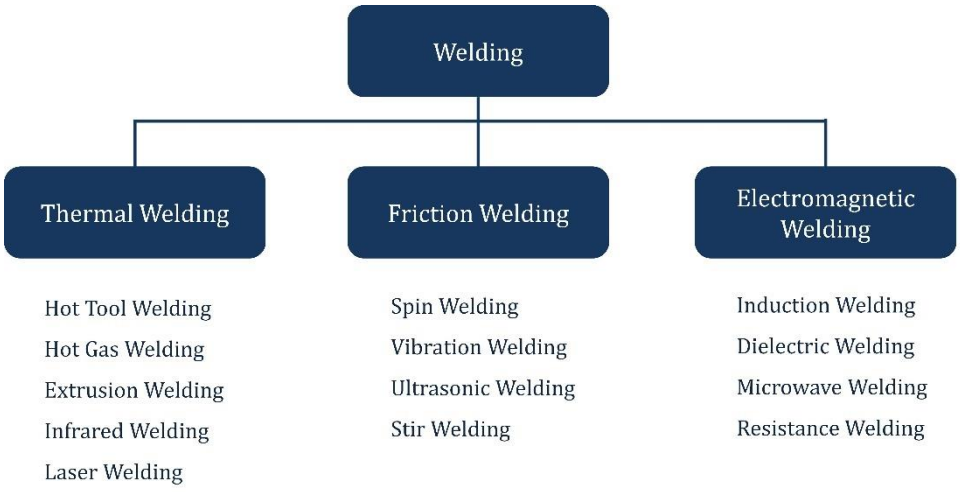

Figure 1.6. Welding techniques classification [20].

There are several welding techniques which are classified according to their heating mechanism, as summarised in Figure 1.6 [20]. The three main "families" of welding techniques can be classified as (i) thermal welding, (ii) friction welding and (iii) electromagnetic welding. Thermal welding relies on an external heat source that can heat up directly the parts to be welded and, subsequently, melt them. After removal of the heat source, the surfaces are brought into contact under the application of pressure. In some cases, like in laser welding, the surfaces are typically in contact from the beginning of the process. Friction welding is a joining method that relies on frictional work at the joint interface in order to generate heat and melt the surfaces, while the joint is constantly under pressure. Electromagnetic welding is the third class of welding techniques and relies on the presence of a conductive material (e.g. stainless steel, graphite) or, in some cases, at the interface between the two surfaces to be welded that can heat up through the application of an electromagnetic field and melt the surfaces, while being constantly under pressure. From those categories, the most promising ones are ultrasonic welding, resistance welding (RW) and induction welding [33][34]. In this study the main focus will be on ultrasonic welding and resistance welding as a continuation of previous work done in the Department of Aerospace Structures and Materials at TU Delft.

1.3.1 Resistance welding

In resistance welding a conductive heating element (e.g. metal mesh, carbon fibre prepreg) is placed between the two parts (substrates) to be welded, while the edges of the heating element are connected to a power supply. Subsequently, electrical current is applied to the heating element resulting in an increase in temperature. The heating mechanism of resistance welding is based on Joule heating: the circulation of electrical current through the heating element results in heat dissipation, which will heat up and, eventually, melt the polymer at the weldline. The principle of Joule heating can be expressed as

$$P = I^2 \cdot R \tag{1.1}$$

where P denotes the Power, I denotes the electrical current and R denotes the electrical resistance of the heating element.

The final stage of this process is the cooling stage; the power is turned off and the joint is allowed to cool down naturally to temperatures below the polymer's glass transition temperature. The two parts are subjected to pressure during the heating and the cooling stage of the process, while the heating element remains trapped in the weld and becomes an integral part of the weldline. In order to minimise heat losses from the system, the adherends are also sandwiched between two thermal insulating blocks. Figure 1.7 illustrates a schematic of a resistance welding setup. The details of the resistance welding set-up used in this study are provided in Chapter 2.

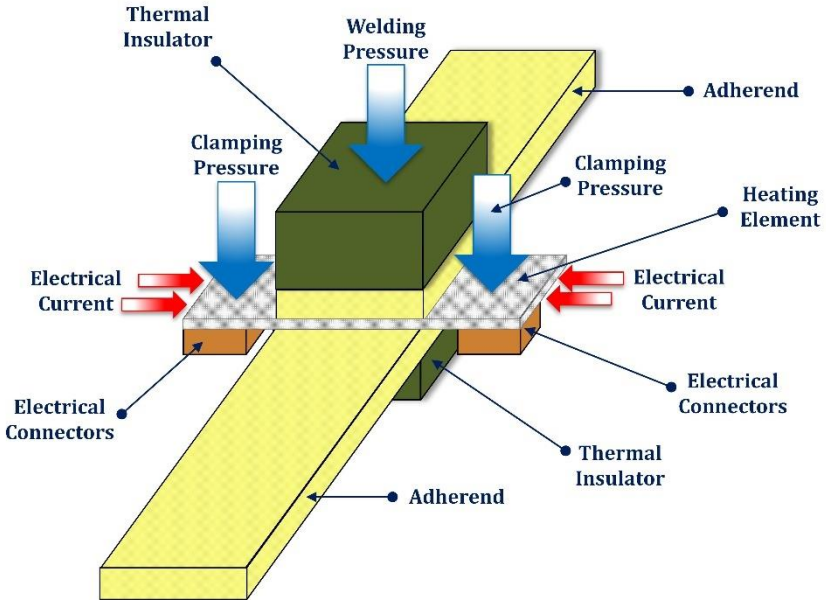

Figure 1.7. Resistance Welding Set-Up. The schematic is adapted from [35].

Resistance welding has already found some use in secondary aircraft structures. Some of the applications are the GF/PPS fixed leading edge of Airbus A340 and A380, the CF/PPS main landing gear doors for Fokker 50 and the CF/PPS rear pressure bulkhead of Airbus A320 [36][37].

1.3.2 Ultrasonic welding

Ultrasonic welding is classified as a friction welding technique; it converts high frequency (typically 20-40 kHz) and low amplitude (typically between 2.5 to 250μm peak-to-peak amplitude) mechanical vibrations into heat via friction [38]. The produced vibrations are transverse to the weld interface and cause surface and intermolecular friction in the materials to be welded which result in heat generation. In order to concentrate heat generation between the adherends, energy directors (ED), which are made of the same polymer as the adherends' matrix, are placed at the weld interface [38]-[40]. The lower compressive stiffness of the energy directors compared to the composite adherends results in higher cyclic strains in the EDs during the welding process which, in turn, promote heat generation [38][40][41]. It is very fast (extremely short cycle times of only a few seconds), there are no foreign materials in the weldline and it produces high quality joints. However, unlike resistance welding, ultrasonic welding has not yet been used as a structural joining technology of TPCs. Nevertheless, recent research efforts by Villegas and co-workers [42][43] have demonstrated that the development of a continuous ultrasonic welding process is not far from industrialization. Figure 1.8 shows a schematic diagram of an ultrasonic welding machine. More details on the ultrasonic welding device used in this study are given in Chapter 3.

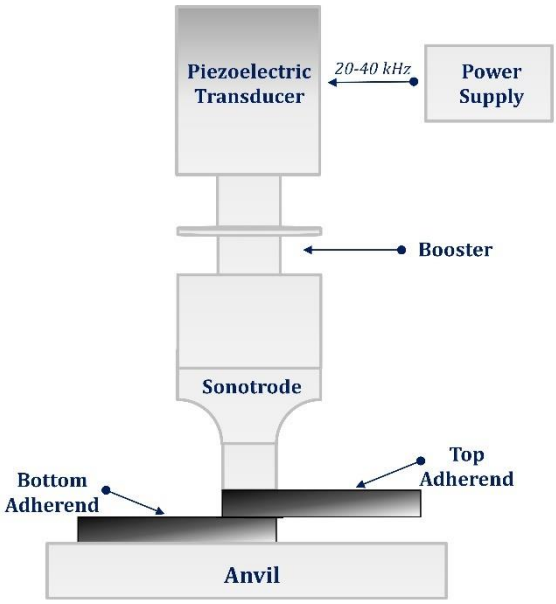

Figure 1.8. Ultrasonic Welding Machine. The schematic is adapted from [34].

1.4 Motivation

Aircraft operate in a wide range of temperatures, typically between -50°C and 70°C which are the typical minimum and maximum service temperatures. However, the temperatures can reach as low as -60°C and as high as 93°C, depending on the application [44]. Polymers are temperature-dependent materials meaning that their properties are influenced by temperature. Properties such as elastic modulus and thermal conductivity usually decrease with increasing temperature while other properties such as specific heat capacity and thermal expansion rate usually increase [3]. It is important to know that in some temperature regions the changes in properties can be dramatic. One of such regions is the glass-rubber transition which occurs in all polymers and can be seen in the schematic illustration of the elastic modulus dependency on temperature of a semi-crystalline thermoplastic (Figure 1.9). This transition is identified by the most important intrinsic property of polymers (in the author's opinion) which is the glass transition temperature (Tg). Below Tg, the polymer is in the glassy state where the molecular chains are, essentially, "frozen". In the glassy state, only some vibrations of atoms and short-range rotational motions take place, resulting in very low molecular mobility. Hence, in the glassy state most of the polymer properties remain fairly constant, at least for the high-performance thermoplastics [3][45][46]. Above the glass transition temperature, the polymer enters the glass-rubber transition region where the molecules start to move in a long-range and coordinated motion due to the increased thermal energy attained by the chain atoms [3]. In the glass-rubber transition the polymer properties can change dramatically, such as the significant drop in elastic modulus, typically a few orders of magnitude, and the increase in thermal expansion rate [3]. In fact, several thermal analysis techniques rely on the changes of these properties in order to determine the glass transition temperature. At higher temperatures, the polymer enters the rubbery plateau where the modulus decreases slightly, becoming virtually constant. In the case of semi-crystalline thermoplastics, a further increase in temperature will bring the polymer into the melting region where the modulus drops significantly and the polymer behaves almost like a liquid (it flows). Amorphous thermoplastics do not melt but soften above their glass transition temperature and exhibit similar flow-like characteristics.

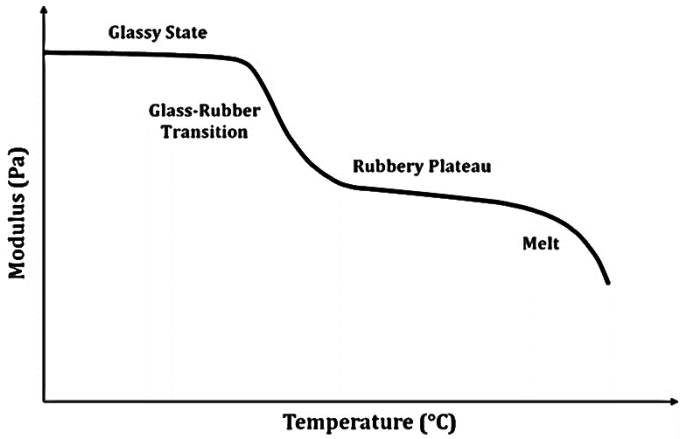

Figure 1.9. Schematic illustration of modulus-temperature relationship of semi-crystalline thermoplastics (adapted from [3]).

Although a polymer composite will never be used as an aircraft structural part when the polymer matrix is not in the glassy state, for some materials such as PPS even temperatures like 80 °C can be critical as they are very close to the glass-rubber transition of PPS (reported in literature as between 80 and 95°C [45]). In addition, it is not only the elastic modulus of the polymer that is of concern at high temperatures. For example, the changes in the CTE – in other words, the changes in the thermal expansion rate – can have a significant effect on the mechanical performance of the composite. It is well known that the fibre/matrix interfacial strength in TPC relies on a high extent on the physical bonding formed during cooling between the fibres and the matrix [47]-[50]. Polymers have a higher CTE than that of glass fibres and carbon fibres. This means that during cooling the polymer will contract more than the fibres, resulting in the formation of residual stresses around the latter. The molecular chains of the polymer will "grip" themselves firmly around the asperities of the fibres, resulting in a phenomenon known as "mechanical interlocking", establishing the physical bonding between the fibres and the matrix. However, when the composite structure (laminate or weld) is heated up, those residual stresses will be relieved due to the higher expansion of the polymer compared to the fibres and will, potentially, diminish the fibre/matrix interfacial strength and, ultimately, the mechanical performance of the composite structure. The importance of fibre/matrix interfacial strength in the weld performance of TPCs joints was demonstrated in a previous work carried out at TU Delft by Shi et al [51] who studied the strength and the failure mechanisms of RW GF/PEI joints. It was found that intralaminar failure was the main failure mechanism, showing either fibre/matrix debonding or laminate tearing. By using two different sizings, the authors showed that the sizing resulted in an improved fibre/matrix adhesion that could significantly increase the lap shear strength. Considering the influence of temperature on the fibre/matrix interfacial strength and the link between the latter and the weld performance, it is expected that the temperature could have an effect on the performance of both RW TPCs joints and UW TPCs joints.

Even though extensive studies have been performed on the effects of temperature on TPC and on adhesive joints [48][52]-[55], to the best of the author's knowledge, very little research has been carried out on the temperature exposure of TPCs welded joints. Most of the research in the field of TPC welded joints has focused on the optimisation and up-scaling of the welding techniques and on the influence of process parameters on the mechanical performance of the joints at room temperature (RT) conditions. With regard to resistance welding much research has been published on the influence of the heating element and process parameters (e.g. welding time and pressure) on the weld performance at RT conditions and on the modelling and optimisation of the welding process [19][25][26][35][51][56]-[58]. Similarly, the studies

carried out on ultrasonic welding of TPCs have focused on investigating the heating mechanisms [59][60], the optimisation of the welding process, and the capability of welding thermoset composites to thermoplastic composites [28][38][39][42][60]. To the author's knowledge, only one study – outside this work – has been published dealing with the effect of temperature on the mechanical performance of TPCs welded joints [61]. Taking the operational temperature range of aircraft into consideration, in conjunction with the temperature-dependency of polymer composites, the exposure of TPCs welded joints to low and high temperatures appears to be worthy of investigation.

While fibre/matrix interfacial strength and the overall mechanical performance of the adherends play an instrumental role in the performance of TPCs welded joints, more factors can affect the weld performance, also at low and high temperatures. Of special interest in this research is the weldline of TPCs joints and how the temperature can influence the weld performance by affecting the weldline properties and/or weldline structure, which is explained in the next two paragraphs

In resistance welding, the use of a metallic mesh as a heating element has proven to be a very efficient method to produce high quality joints [51]. However, the metal mesh remains in the weldline as an integral part of the consolidated welded joint. The polymer/metal interface relies on the same principles as the fibre/matrix interface which were described earlier. During cooling, the polymer contracts more than the metal and the formation of residual stresses enhances the mechanical interlocking between the polymer and the metal. A temperature increase might loosen the mechanical interlocking due to the polymer expansion and potentially affect the mechanical behaviour of the weld.

In ultrasonic welding there is no foreign material in the weldline, therefore, the TPCs joints made with ultrasonic welding are virtually a continuous composite structure. However, the process speed of ultrasonic welding is very fast, resulting in extremely fast cooling rates. When the polymer is cooled down from its melt, the molecular chains will start to disentangle from the melt and to organise themselves into ordered structures (crystals). In essence, the polymer transitions from a higher entropy state (melt) to a lower entropy state (crystals). However, the organisation of molecular chains into crystals not only requires sufficient thermal energy but also time. Depending on the crystallization kinetics, very fast cooling rates might result in lower degree of crystallinity or even to fully amorphous polymers. For example, high density polyethylene (HDPE) is known to have very fast crystallization kinetics, meaning that HDPE crystallizes almost instantaneously once cooled down from its melt. The cooling rates to quench HDPE need to be higher than 10^6 K/s [62]. Other polymers, though, crystallize in a slower fashion, for example, quenching of PPS has been reported at rates between 20 to 30 K/s [63][64]. With this in mind, the formation of an amorphous polymer – or of low crystallinity – in the weldline seems to be a reasonable possibility, depending on the actual cooling rates of ultrasonic welding and the crystallization kinetics of the polymer. The structure and, ultimately, the performance of semi-crystalline polymers depend heavily on the process cooling rates. The very fast cooling rates not only can result in lower crystallinity but can also result in different morphology like lamellar thickness and crystal size distribution [65][66]. Two key differences between the amorphous and the semi-crystalline version of the same polymer (e.g. amorphous PPS and semi-crystalline PPS) is that the modulus and the glass transition temperature of the former are usually lower. In fact, the Tg can be lower by several degrees Celsius [67]-[69]. As explained previously, the performance of polymer composites and, potentially, of TPCs welded joints can be dramatically affected by temperature. A possible shift in the Tg due to crystallization could have a major impact on the performance of TPCs welded joints.

Summarizing the ground covered in this section, the reader is reminded of the temperature-dependency of polymers, the effect of temperature on fibre/matrix interfacial strength and the direct connection between the latter and the strength of TPCs welded joints. In addition, the weldline properties and/or structure in both types of welds can also be affected by temperature, as the available evidence suggests. Hence, with this background in mind it becomes clear that the exposure of TPCs welded joints to low and high temperature is worthy of investigation. The discussion on resistance welding centres on the overall thermal effects on the weld performance using the optimum process parameters which were identified in a previous study [25]. The objective of the current work on resistance welding is not to correlate the process parameters with the weld performance at various temperatures, but to understand how the weld strength is affected by temperature and to assess the connection between the heating element and the matrix. The overall thermal effects on the strength of UW TPCs joints are also addressed but the discussion focuses more on the crystallization of the matrix at the weldline. Taking into account the very short cycle times of ultrasonic welding (few seconds) compared to the longer cycle times of resistance welding (few minutes), the focus of this research, regarding polymer crystallization and its effect on weld performance at low and high temperatures, was put on ultrasonic welding.

1.5 Research Objective

The objective of this research is to develop a more comprehensive understanding of the behaviour of TPCs welded joints at low and high temperatures.

The research questions of this work can be summarized as follows:

> *(i) How is the performance of thermoplastic composites welded joints affected by the testing temperature and which material properties are governing the strength and the failure mechanisms?*
>
> *(ii) To which extent is the weld performance at a wide range of temperatures dictated by the crystalline structure of the matrix in the weldline and adjacent areas and how is the welding process affecting such crystalline structure?*

For this study PPS was the matrix choice, as a continuation of previous work done on resistance welding and ultrasonic welding in the Department of Aerospace Structures and Materials at TU Delft; but also because PPS is a semi-crystalline thermoplastic that, first, has a higher potential to be used in more demanding chemical environments compared to PEI or even PEKK and, second, it allows for a thorough study on the crystallinity effect on weld strength due to its relatively slow crystallization kinetics. In addition, the glass transition temperature of PPS is reported to be between 80 and 95°C [45] which is close to the maximum operational temperature of aircraft, hence, it can provide a great insight of the behaviour of TPCs welded joints close to the polymer's glass transition temperature and close to the temperature operational limits of the aircraft. For the resistance welding experiments, the use of glass fibre reinforced PPS was preferred: using carbon fibre laminates can result in current leakage inside the adherends which, in turn, would affect the quality and most importantly, the consistency of the welds. Although current leakage can be prevented by electrically insulating the metal mesh [57] it was decided to use glass fibre laminates as this would ensure no current leakage and eliminate any questions regarding ineffective insulation which could affect the results. Since the objective of this research was the investigation of the thermal effects on RW TPCs joints, it was very important to ensure that all the welds made with resistance

welding would have the same quality. For the ultrasonic welding experiments, carbon fibre reinforced PPS and neat PPS were used as adherends and energy directors, respectively.

1.6 Thesis outline

This thesis is divided into 7 Chapters. The outline of this thesis can be summarised as follows:

Chapter 2: In this chapter, the first research question is addressed with respect to resistance welding. The results of exposing glass fibre reinforced PPS RW joints to testing temperatures between -50°C and 150°C are presented and discussed in terms of weldline properties, adherend properties and failure mechanisms.

Chapter 3: This chapter addresses the second part of the second research question. The effect of the ultrasonic welding process parameters on the crystalline structure of PPS in the weldline of ultrasonically welded carbon fibre reinforced PPS joints is analysed.

Chapter 4: This chapter is complementary to chapter 3, as the second part of the crystallinity assessment of PPS in the weldline of ultrasonically welded joints. The assessment is performed through nanoindentation measurements and is carried out in the surrounding areas (adherends) as well. The effect of the process parameters on the formation and the extent of a Heat Affected Zone (HAZ) inside the adherends is also discussed.

Chapter 5: In this chapter, essentially, both research questions are addressed, with respect to ultrasonic welding. The results of single lap shear tests (SLS) carried out at temperature ranging from -50°C to 120°C are presented and discussed on the basis of weldline properties, adherend properties and failure mechanisms. The link between the matrix crystallinity and the temperature dependence of the mechanical behaviour of ultrasonically welded carbon fibre reinforced PPS joints is also investigated and discussed.

Chapter 6: A discussion connecting the results shown in the previous chapters is given, drawing direct comparisons between the two polymer composite types, GF/PPS and CF/PPS. The two welding techniques, resistance welding and ultrasonic welding, are also compared.

Chapter 7: The conclusions of this work together with the recommendations for future work are presented.

Bibliography

[1] Olson RG. Technology and Science in Ancient Civilizations. Greenwood, 2010.
[2] Rehren T, Belgya T, Jambon A, Káli G, Kasztovszky Z, Kis Z et al. 5,000 years old Egyptian iron beads made from hammered meteoritic iron. Journal of Archaeological Science 2013; 40: 4785-4792.
[3] Sperling LH. Introduction to physical polymer science. Pennsylvania: Wiley-Interscience, 4th edition, 2005.
[4] Panayiotou C. Science and Technology of Polymers. Thessaloniki: Pegasos, 2nd edition, 2000.
[5] Hull D. Clyne TW. An Introduction to Composite Materials. Cambridge University Press, 2nd edition. 1996.
[6] Tsai SW, Hahn HT. Introduction to Composite Materials. Technomic Publishing Company Co, Inc, 1980.
[7] Roeseler WG, Sarh B, Kismarton MU. Composites structures: The first 100 years. 16th International Conference on Composite Materials 2007; 1-10.
[8] Windsor HH. Popular Mechanics Magazine, March 1943; 79(3).
[9] Park SJ. Carbon Fibers. Singapore: Springer, 2nd edition, 2018.
[10] Vosteen LF, Hadcock RN. Composite chronicles: Past performance and future prospects. NASA Conference Publication, Issue 3229, Part 1 1993; 1-19.
[11] https://www.airbus.com/(accessed December 2020).
[12] http://www.boeing.com/(accessed December 2020).
[13] Beaumont PWR, Soutis C, Hodzic A. The Structural Integrity of Carbon Fiber Composites. Springer, 2017.
[14] https://www.airbus.com/aircraft/passenger-aircraft/a350xwb-family.html
[15] https://www.airbus.com/newsroom/news/en/2017/08/composites--airbus-continues-to-shape-the-future.html
[16] https://www.atag.org/facts-figures.html,(accessed December 2020).
[17] Ibeh CC. Thermoplastic Materials: Properties, Manufacturing Methods, and Applications. Boca Raton, FL: CRC Press, Taylor & Francis Group, 2011.
[18] Jones DP, Leach DC, Moore DR. Mechanical properties of poly(ether-ether-ketone) for engineering applications. Polymer 1985; 26(9): 1385-1393.
[19] Ageorges C, Ye L. Fusion Bonding of Polymer Composites. London: Springer, 2002.
[20] Youseprouf A, Hojjati M, Immarigeon JP. Fusion bonding/welding of thermoplastic composites. Journal of Thermoplastic Composite Materials 2004; 17: 303-341.
[21] http://www.compositesworld.com/articles/thermoplastic-composites-primary-structure
[22] Campbell FC. Structural Composite Materials. Ohio: ASM International, 2010.
[23] Pocius AV. Adhesion and Adhesives Technology. Munich: Hanser 3rd edition, 2012.
[24] Niu MCY. Composite Airframe Structures, Practical Design Information and Data. Hong Kong: Conmilit Press Ltd, 1st edition, 1992.
[25] Shi H. Resistance welding of thermoplastic composites. Process and performance. Delft: Delft University of Technology, 2014.
[26] Yuan Q, Hou M, Mai YW, Ye L. Resistance welding of carbon fiber reinforced polyetherimide composite. Journal of Thermoplastic Composite Materials 2001; 14: 2-19.
[27] Villegas IF, Rubio PV. On avoiding thermal degradation during welding of high-performance thermoplastic composites to thermoset composites. Composites: Part A 2015; 77: 172-180.

[28] Villegas IF, van Moorleghem R. Ultrasonic welding of carbon/expoy and carbon/PEEK composites through a PEI thermoplastic coupling layer. Composites Part A 2018; 109: 75-83.
[29] Lionetto F, Morillas MN, Pappadà, Buccoliero G, Villegas IF, Maffezzoli A. Hybrid welding of carbon-fiber reinforced epoxy based composites. Composites Part A 2018; 104: 32-40.
[30] R.P. Wool, K.M. O'Connor. A theory of crack healing in polymers. Journal of Applied Physics 1981; 52: 5953-5963.
[31] Y. H. Kim, R.P. Wool. A theory of healing of polymer-polymer interface. Macromolecules 1983; 16: 1115-1120.
[32] Wool RP, Yuan BL, McGarel OJ. Welding of Polymer Interfaces. Polymer Engineering and Science 1989; 29(19): 1340-1367.
[33] Villegas IF. Optimum processing conditions for ultrasonic welding of thermoplastic composites. 19th International Conference on Composite Materials 2013.
[34] Ageorges C, Ye L, Hou M. Advances in fusion bonding techniques for joining thermoplastic matrix composites: a review. Composites: Part A 2001; 32: 839-857.
[35] Ageorges C, Ye L, Mai YW, Hou M. Characteristics of resistance welding of lap shear coupons. Part I: Heat transfer. Composites: Part A 1998; 29: 899-909.
[36] Offringa A. New thermoplastic composite design concepts and their automated manufacture. JEC Composites Magazine 2010; 58 (June-July): 45-49.
[37] https://www.gknaerospace.com/globalassets/downloads/homepage/in-the-media/cw-2018-09-50-63.pdf/
[38] Palardy G, Villegas IF. On the effect of flat energy directors thickness on heat generation during ultrasonic welding of thermoplastic composites. Comp Interfaces 2017; 24:2, 203-214.
[39] Villegas IF. Strength development versus process data in ultrasonic welding of thermoplastic composites with flat energy directors and its application to the definition of optimum processing parameters. Composites: Part A 2014; 65: 27-37.
[40] Villegas IF. In situ monitoring of ultrasonic welding of thermoplastic composites through power and displacement data. J Thermoplast Compos Mater 2015; 28: 66-85.
[41] Potente H. Ultrasonic welding – principles and theory. Mater De 1984; 5(5): 228-34.
[42] Jongbloed B, Teuwen J, Palardy G, Villegas IF, Benedictus R. Continuous ultrasonic welding of thermoplastic composites: enhancing the weld uniformity by changing the energy director. Journal of Composite Materials 2019; 0(0): 1-13. Open Access.
[43] Senders F, van Beurden M, Palardy G, Villegas IF. Zero-flow: a novel approach to continuous ultrasonic welding of CF/PPS thermoplastic composite plates. Advanced Manufacturing: Polymer & Composites Science 2016; 2(3-4): 83-92.
[44] Composite Materials Handbook. USA: Department of Defense Handbook. Vol. 3, 2002.
[45] Spruiell JE, Janke CJ. A review on the measurement and development of crystallinity and its relation to properties in neat poly(phenylene sulfide) and its fiber reinforced composites. Technical Report, Oak Ridge National Laboratory, 2004.
[46] Vieille B, Aucher J, Taleb L. Influence of temperature on the behavior of carbon fiber fabrics reinforced PPS laminates. Materials Science and Engineering A 2009; 517: 51-60.
[47] Thomason JL, Yang L. Temperature dependence of the interfacial shear strength in glass-fibre polypropylene composites. Composites Science and Technology 2011; 71: 1600-1605.
[48] Rao V, Drzal LT. The temperature dependence of interfacial shear strength for various polymeric matrices reinforced with carbon fibers. Journal of Adhesion 1992; 37: 88-95.
[49] Di Landro L, Pegoraro M. Evaluation of residual stresses and adhesion in polymer composites. Composites Part A 1996; 27A: 847-853.

[50] Kim JK, Mai YW. Engineered Interfaces in Fiber Reinforced Composites. Elsevier, 1998.
[51] Shi H, Villegas IF, and H.E.N. Bersee HEN. Strength and failure modes in resistance welded thermoplastic composite joints: Effect of fibre-matrix adhesion and fibre orientation. Composites: Part A 2013; 55: 1-10.
[52] K.Y. Kim, L. Ye, K.M. Phoa. Interlaminar fracture toughness of CF/PEI and GF/PEI composites at elevated temperatures. Applied Composite Materials 2004; 11: 173-190.
[53] Zhang Y, Vassilopoulos AP, Keller T. Effects of low and high temperatures on tensile behaviour of adhesively-bonded GFRP joints, Composite Structures 2010; 92: 1631-1639.
[54] Ashcroft IA, Hughes DJ, Shaw SJ, Abdel Wahab M, Crocombe A. Effect of temperature on the quasi-static strength and fatigue resistance of bonded composite double lap joints, J. Adhesion 2001; 75: 61-88.
[55] Adams RD, Coppendale J, Mallick V, Al-Hamdan H. The effect of temperature on the strength of adhesive joints. International Journal of Adhesion and Adhesives 1992; 12(3): 185-190.
[56] Dubé M, Hubert P, Gallet JNAH, Stavrov D, Bersee HEN, Yousefpour A. Metal mesh heating element size effect in resistance welding of thermoplastic composites. Journal of Composite Materials 2011; 46(8): 911-919.
[57] Dubé M, Hubert P, Yousefpour A, Denault J. Current leakage prevention in resistance welding of carbon fibre reinforced thermoplastics. Composites Science and Technology 2008; 68: 1579-1587.
[58] Shi H, Villegas IF, Octeau MA, Bersee HAN, Youseprouf A. Continuous resistance welding of thermoplastic composites: modelling of heat generation and heat transfer. Composites: Part A 2015; 70: 16-26.
[59] Tolunay MN, Dawson PR, Wang KK. Heating and bonding mechanisms in ultrasonic welding of thermoplastics. Polym Eng Sci 1983; 23(13): 726-33.
[60] Levy A, Le Corre S, Villegas IF. Modeling of the heating phenomena in ultrasonic welding of thermoplastic composites with flat energy directors. J Mater Process Technol 2014; 214: 1361-1371.
[61] Rohart V, Dubé M, Laberge Lebel L. Effects of temperature on the apparent lap shear strength of resistance-welded carbon fibre/thermoplastic composite joints. In: International SAMPE technical conference 2018-May; 1-10.
[62] Toda A, Androsch R, Schick C. Insights into polymer crystallization and melting from fast scanning chip calorimetry. Polymer 2016; 91: 239-263.
[63] Grouve WJB, Vanden Poel G, Warnet LL, Akkerman R. On crystallization and fracture toughness of poly(phenylene sulphide) under tape placement conditions. Plastics, Rubber and Composites 2013; 42(7): 282-288.
[64] Furushima Y, Kumazawa S, Umetsu H, Toda A, Zhuravlev E, Schick C. Melting and recrystallization kinetics of poly(butylene terephthalate). Polymer 2017; 109: 307-314.
[65] Chung JS, Cebe P. Melting behaviour of poly(phenylene sulphide): 1. Single-stage melt crystallization. Polymer 1992; 33(11): 2312-2324.
[66] Gedde UW. Polymer Physics. Chapman & Hall, 1995.
[67] Zhang RC, Li R, Lu A, Jin Z, Liu B, Xu Z. The glass transition temperature of poly(phenylene sulfide) with various crystallinities. Polymer Int 2013; 62: 449-453.
[68] Krishnaswamy RK, Geibel JF, Lewis BJ. Influence of semicrystalline morphology on the physical aging characteristics of poly(phenylene sulfide). Macromolecules 2003; 36: 2907-2914.
[69] Jonas A, Legras R. Relation between PEEK semicrystalline morphology and its subglass relaxations and glass transition. Macromolecules 1993; 26: 813-824.

2 Influence of temperature on the strength of RW GF/PPS joints

We live in a society exquisitely dependent on science and technology,
in which hardly anyone knows anything about science and technology.

(Carl Sagan)

This chapter is an adaptation of the paper published in the journal "Composites Part A: Science and Manufacturing", in 2018[1]*.*

In this chapter, the effect of temperature exposure on the strength of resistance welded joints is analysed, addressing the first research question of this thesis. GF/PPS adherends were joined using the resistance welding technique, using a stainless steel mesh as the heating element. Single lap shear tests were performed at temperatures ranging between -50 °C and 150 °C to evaluate the strength of the welded joints, and fractography analysis was carried out to examine the failure mechanisms. Thermal analysis and in-plane shear tests were also performed in order to identify the material properties governing the strength and failure mechanisms of the resistance welded joints.

[1] *Koutras N, Villegas IF, Benedictus R. Influence of temperature on the strength of resistance welded glass fibre reinforced PPS joints. Composites: Part A 2018; 105: 57-67.*

2.1 Introduction

Over the last years, high performance thermoplastics, notably PEEK, PEKK, PPS and PEI, have gained significant ground in the aerospace industry [1] due to advantageous qualities like their superior damage tolerance, excellent chemical resistance, infinite shelf-life, recyclability, and ability to be welded [2][3]. Aircraft structures are large and complex and cannot be manufactured in a single step, therefore, joining techniques are utilised in order to connect different parts together. Hence, joining of polymer composites is of significant importance for the aerospace industry due to the need of reliable, automated and cost-efficient joining methods. As detailed in chapter 1, welding has been considered as an effective alternative technique for the joining of thermoplastic composites, since it brings several advantages compared to the traditional techniques that can minimise most of these problems. In summary, the principal advantages of welding are the minimised stress concentration, the minimised labour, the very short cycle times and the minimal surface preparation of the substrates [4][5].

Amongst the various welding techniques, resistance welding is considered as a promising joining technique for thermoplastic composites, which can consistently produce high quality joints with short cycle times, and it has already been successfully used in secondary aircraft structures [1]. The work presented in literature about resistance welding of TPCs is primarily concerned with the optimisation of the processing parameters, the effect of the heating element and the characterisation of joint strength and failure modes at room temperature. Hou et al. found that the type of the heating element affected the temperature distribution at the weldline as well as the joint strength [6], while Dubé et al. investigated the influence of the metal mesh geometry; they found that the wire diameter as well as the open gap width had an important effect on the weld quality [7]. Welding time, welding pressure, and power density have been identified as the main factors which govern the welding process and, consequently, the weld quality [8]-[11]. Moreover, the failure modes of resistance welded joints have been classified by several authors, with intralaminar failure being the predominant mode for high quality joints [4][8][11].

However, aircraft operate in a wide range of temperatures, typically between -50 °C and 70 °C [12] while due to operation some components can be subjected to temperatures as high as 93 °C [12]. Taking this temperature range into consideration, it becomes clear that more knowledge should be gained regarding the exposure of RW TPCs to various temperatures. In literature, there are extensive studies dealing with the effect of temperature on adhesive joints. The strength of adhesively bonded fibre reinforced polymer double lap joints has been reported to decrease with increasing temperature, while the failure mode at high temperatures changed from adherend failure to adhesive failure [13][14]. Adams et al. studied the exposure of adhesive single lap joints to a wide range of temperatures (-60 °C, 200 °C) and found that the joint strength decreased at low and high temperatures because the adhesive became brittle and soft, respectively [15]. Da Silva and Adams studied the effect of temperature on titanium/composite double lap joints and found that the failure of the joints at -55 °C and 22 °C occurred through the thickness of the composite [16]. The same authors investigated the mixed modulus concept of low temperature and high temperature adhesives and suggested that for dissimilar adherend double lap joints, the use of a high modulus adhesive and a low modulus adhesive improved the performance compared to the high modulus adhesive alone [17].

Although, as briefly outlined before, much research is described in literature about the influence of temperature on bonded joints in fibre reinforced polymers, to the author's knowledge, there is very limited work on the influence of temperature on resistance welded

polymer composite joints [18]. Despite obvious similarities between bonded joints and welded joints (i.e. joint architecture, continuous joint nature, polymer-rich joint weldline), they hold several fundamental differences which may cause different temperature-dependent mechanical performances. These fundamental differences concern the joining mechanisms, i.e. adhesive forces versus molecular inter-diffusion, and the architecture and nature of the joint weldline, i.e. dissimilar polymer versus matrix polymer with embedded metal mesh. Likewise, available knowledge on the effect of temperature on the behaviour of fibre reinforced polymers is not directly applicable to RW joints owing to the complexity of the weldline. In particular, the effect of varying temperature could be detrimental to the strength of the welded joints by virtue of the nature of the bond between the metal mesh and the polymer matrix at the weldline. Resistance welded joints feature a rather complex resin-rich weldline with an embedded resistive heating element, generally a metal mesh. It is known that the mechanism dictating the bond between metals and polymers is mechanical interlocking [19][20]. During the welding process, the polymer matrix wets and penetrates the irregularities of the metal surface and the mesh open gaps, locking itself mechanically to the metal wires. This mechanism is promoted by the residual thermal stresses that are formed during the cooling process. As the thermoplastic cools down from its melt, it shrinks and contracts more than the metal due to their CTE mismatch, thereby, resulting in compressive stresses on the metal wire. Consequently, at room temperature the polymer matrix and the metal mesh form a strong connection, as it was demonstrated in a previous study where the main failure at room temperature, in GF/PEI and GF/PPS RW joints, was found to be glass fibre/matrix debonding [8]. However, when the joints are subjected to higher temperatures, the opposite effect will occur. In particular, at high temperatures the compressive stresses will be lowered due to the higher thermal expansion of the polymer over the metal wires, resulting in a diminished mechanical interlocking, which could have a detrimental effect on the joint strength. Therefore, even if the stainless steel mesh does not have a negative impact on the mechanical performance of RW joints at room temperature conditions, it could still be the primary reason for joint failure at high temperatures.

Hence, two key questions arise which require further investigation in order to develop a comprehensive understanding of the behaviour of resistance welded thermoplastic composite joints at different temperatures.

- Is the connection between the metal mesh and the thermoplastic matrix the weakest link at the weldline when the joints are subjected to elevated temperatures?
- How is the weld strength affected by temperature?

To fill this gap, this chapter analyses the strength and failure mechanisms of resistance welded glass fibre reinforced PPS joints tested at a wide range of temperatures using a fully experimental approach. The major objective of this study is to evaluate in detail the relationships between the joint strength and the constituents of the joint, namely the fibres, the thermoplastic matrix and the metal mesh, under the influence of temperature.

2.2 Experimental procedure

2.2.1 Laminate manufacturing

The material used in this study was Cetex® woven (eight harness satin) glass fibre reinforced polyphenylene sulphide composite supplied by Ten Cate Advanced Composites, The Netherlands. Laminates measuring 580 mm x 580 mm were built from semi-impregnated GF/PPS layers with a stacking sequence of $[(0°/90°)_4]_s$, with a nominal fibre volume fraction of 50%. 0° is the direction of the warp yarns while 90° is the direction of the weft yarns of the woven fabric. The laminates were consolidated using a hot platen press at 320 °C and 1 MPa pressure for 20 min. The cooling rate of the press plates was consistently set at 15 °C/min for all the laminates manufactured in this study. The stainless steel moulds used in the press consolidation process were first cleaned with acetone, then degreased with a degreasing agent (PFQD, from Socomore) and finally coated with Marbocote 227CEE release agent. The final thickness of the consolidated laminates was 1.9 mm. Welding adherends and test specimens were cut from the consolidated laminates using a water-cooled diamond blade.

2.2.2 Resistance welding

The in-house developed resistance welding setup shown in Figure 2.2 was used in this work. The main elements in this setup are:

(a) Direct current (DC) power supply unit with a maximum power output of 45A/70V (Delta Electronika, The Netherlands) that provides the welding energy.

(b) A pneumatic cylinder which provides both the welding pressure and the clamping pressure.

(c) Two copper connectors which are connected to the power supply and to the heating element in order to circulate electrical current.

(d) Two thermal insulation blocks (top and bottom) made out of ceramic blocks to minimise the heat losses from the system and allow for gradual cooling of the matrix.

(e) A computer equipped with dedicated LabView software for welding process control.

(f) Data acquisition system (DAQ).

A plain woven stainless steel (AISI 304L) mesh with 0.04 mm wire diameter and 0.09 mm open gap width (Dinxperlo, The Netherlands) was used as the heating element in the welding process based on the results presented in [7]. The dimensions of the heating element were 300 mm x 13 mm. The heating element was placed over the bottom adherend while being in good contact with the copper connectors to ensure electrical current circulation (Figure 2.2). An 80 µm-thick neat amorphous PPS film (Amcor Flexibles, Gent, Belgium) was placed between the metal mesh and the top adherend for adequate filling of the open areas in the mesh during the welding process. The adherends, with dimensions 102 mm x 171 mm, were welded in a single lap configuration with overlap dimensions 171 mm x 13 mm. Both adherends and the heating element were degreased (PFQD degreasing agent) prior to welding. The welding parameters, resulting from an optimization performed in a previous study [21], were 80 kW/m^2 power density, 0.8 MPa welding pressure and 55 seconds heating time.

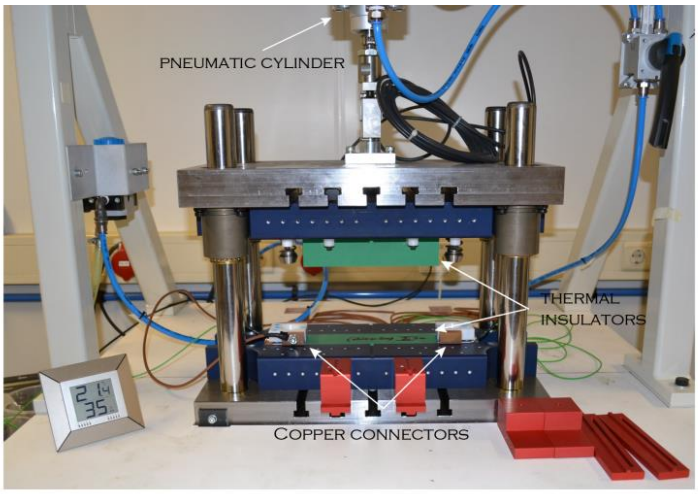

Figure 2.1. Resistance Welding set-up. The different parts of the device are indicated on the figure.

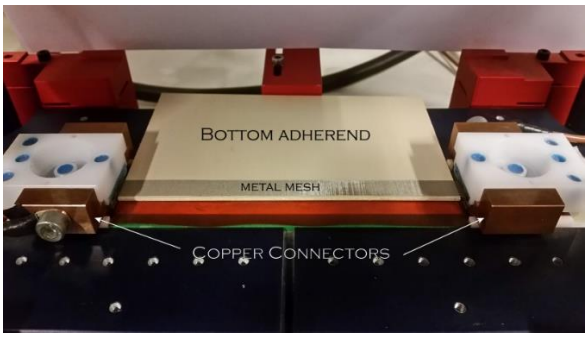

Figure 2.2. Preparation of RW joints. The metal mesh is placed over the bottom adherend while being in good contact with the copper connectors in order to ensure electrical current circulation.

The temperature at the weldline during the welding process (heating and cooling stages) was not measured in this study. However, by using the temperature measurements performed during resistance welding of GF/PEI joints by Shi (estimated cooling rates of 3 °C/s) [21], it was possible to estimate the cooling rates during resistance welding of GF/PPS joints in the present study. In both cases, i.e GF/PEI joints by Shi and GF/PPS joints in the present study, the process parameters were the same and taking into account that PPS has a similar thermal conductivity as PEI (at room temperature: 0.19 W/mK and 0.22 W/mK, respectively) [21] it can be assumed that the cooling rates would be almost the same, i.e. close to 3 °C/s.

2.2.3 Material characterisation

2.2.3.1 Thermal analysis

Dynamic Mechanical Analysis (DMA) was used to measure the glass transition temperature and the evolution of the storage and loss moduli of the PPS resin and the GF/PPS composite. Three point bending DMA tests were carried out in a Pyris Diamond DMA from Perkin Elmer, from -70 °C to 200 °C, at a frequency of 1Hz and a heating rate of 2 °C/min. The dimensions of the specimens were 40 mm x 15 mm x 2 mm for the neat PPS and 40 mm x 13 mm x 1.9 mm for the GF/PPS composite. Liquid nitrogen was used in order to reach cryogenic temperatures.

Thermomechanical Analysis (TMA) was used to measure the CTE of PPS within 25 °C to 140 °C temperature range. The TMA experiments were carried out on a 10 mm x 3 mm x 0.08 mm annealed PPS film specimen in a Diamond TMA from Perkin Elmer. The heating rate was 2 °C/min and the static force applied to the specimen was 5 mN. The PPS film was supplied by

Amcor Flexibles (Gent, Belgium). The initial (as-received) state of the PPS film was amorphous. The film was annealed in an oven for 2 hours at 200 °C in order to perform the TMA measurements on semi-crystalline PPS which is more representative of the weldline PPS structure. The TMA specimen was subjected to three cycles of heating up to 140 °C, cooling down to 25 °C, at a rate of 2 °C/min, in order to "erase" the previous thermal history. Since it was not possible to heat up to the melting point for practical reasons (to prevent polluting the chamber and the clamps), the two additional cycles were ran as a confirmation that no additional changes occurred within this temperature range (25-140 °C) for the annealed specimen.

The CTE values were computed using the following equation:

$$\boldsymbol{\alpha_m = \frac{1}{L_0} \cdot \frac{dL}{dT}} \qquad \textbf{(2.1)}$$

Where:

- α_m is the mean coefficient of thermal expansion, in µm/(m·°C)
- L_0 is the initial specimen length at RT, in m.
- dL is the change in the specimen length, in µm.
- dT is the change in temperature, in °C.

For higher precision in the computation of the CTE, a minimum temperature difference (dT) of 40 °C was used, when possible (i.e. not at regions where a large change in slope was observed).

2.2.3.2 In-plane shear tests

For the determination of in-plane shear (IPS) strength and modulus at different temperatures within the -50 °C to 120 °C range, ±45° tensile tests were performed in a Zwick 250kN machine, according to the ASTM D3518 standard [22]. The relative deviation of the machine was ±0.65% in the range of 500 N, and below ±0.04% for higher loads. The ±45° tensile test was chosen as an evaluation method because it is a simple test in terms of fixture and specimen preparation and it has been proven to be sensitive to the interfacial shear strength [23]. This was motivated by the findings by Shi et al. who identified fibre/matrix debonding as the main failure mechanism of RW GF/PPS and GF/PEI joints tested at room temperature [21]. The test specimens were cut in the ±45° direction of the fibres, using a water cooled diamond blade. The specimens were 250 mm-long, 25 mm-wide and 1.9 mm-thick. 50 mm-long paper tabs were bonded on the specimens using a cyanoacrylate adhesive (RS Components) in order to prevent slippage during testing. 0°/90° biaxial rosette strain gauges from Kyowa (KFG-5-120-D16-23) with 5 mm gauge length were bonded to the middle section of the specimens (Cement Glue CC-33A, Kyowa) for in-plane strain measurements (parallel and transverse to the longitudinal direction of the samples). The temperature chamber used for the tests was pre-heated for 1 hour at the test temperature and the specimens were pre-conditioned for 30 minutes prior to the tests. Liquid nitrogen was used for the tests at -50 °C. All tests were conducted in displacement control at a loading rate of 2 mm/min.

In total three specimens per temperature were tested and used to calculate the average shear stress and the average shear modulus. It must be noted that, following the guidelines in the ASTM D3518 standard, the in-plane shear strength was calculated at 5% shear strain, since at this strain level the fibre rotation is small and hence the difference between apparent and actual shear stresses can be expected to be small, as reported by Wisnom [24]. The in-plane

shear modulus (G_{12}) was calculated in the initial elastic region, i.e. in the 0.01% – 0.1% strain range.

The in-plane shear strain, γ_{12}, was calculated as:

$$\boldsymbol{\gamma_{12} = \varepsilon_{yy} - \varepsilon_{xx}} \quad \textbf{(2.2)}$$

where ε_{yy} is the longitudinal strain and ε_{xx} is the transverse strain.

The in-plane shear stress, τ_{12}, was calculated as:

$$\boldsymbol{\tau_{12} = \frac{F}{2 \cdot w \cdot z}} \quad \textbf{(2.3)}$$

where F is the applied load in [N], and w and z, the width and thickness in [mm] respectively.

2.2.4 Characterisation of welded joints

2.2.4.1 Single lap shear tests

From each welded sample, five single lap shear specimens were cut using a water-cooled diamond blade with a final width of 25.4 mm. SLS tests based on the ASTM D 1002 standard [25] were performed at different temperatures within the -50 °C to 150 °C range. For the single lap tests the 250kN Zwick/Roell universal testing machine, equipped with a temperature chamber, was used. The temperature chamber was pre-heated for 1 hour at the test temperature and all specimens were maintained at the test temperature for 30 minutes prior to testing in order to reach equilibrium of the entire specimen. Liquid nitrogen was used to perform the tests at -50 °C. The apparent lap shear strength (LSS) of the RW joints was calculated as the maximum load divided by the average overlap area (25.4 mm x 13 mm). The total number of specimens tested at each temperature is shown in Table 2.1**.**

Table 2.1. Number of single lap joint specimens tested at each temperature.

Test Temperature (± 2 °C)	-50	20	50	70	90	120	150
# of specimens	9	43	16	15	15	10	8

2.2.4.2 Fractography

Fractography was used to investigate the failure mechanisms of the welded joints. For this purpose a stereo microscope (Zeiss stereo Discovery V8) and a scanning electron microscope (SEM) from JEOL (JSM-7500F) were used. Image J (open source software) was used to calculate the size of areas of interest on the fracture surfaces.

2.3 Results

2.3.1 Material characterisation

2.3.1.1. Thermal analysis

The thermal evolution of the loss and the storage moduli of the PPS resin and the GF/PPS composite, as resulting from DMA tests, is shown in Figure 2.3. The loss modulus (E″) of both the neat PPS resin and the GF/PPS composite exhibited a peak with a maximum at around 103 °C, which defines the Tg of the polymer and, as expected, it coincided with a significant drop in the storage modulus (E′). In the case of the GF/PPS composite a secondary smaller peak with onset at around 50 °C was also observed in the loss modulus. At that temperature the storage modulus of the composite was found to already start slowly dropping. It is worth mentioning that both the storage and the loss modulus of the GF/PPS composite showed a slight sudden increase towards the end of the DMA test (i.e. at around 200 °C). Possible reasons for this peculiar behaviour could be either a test artefact or interaction between the reinforcing fibres and the loading nose, although further tests would be necessary to clarify it. Such research is however out of the scope of this work, where the temperature range of interest was between -50 and 150 °C.

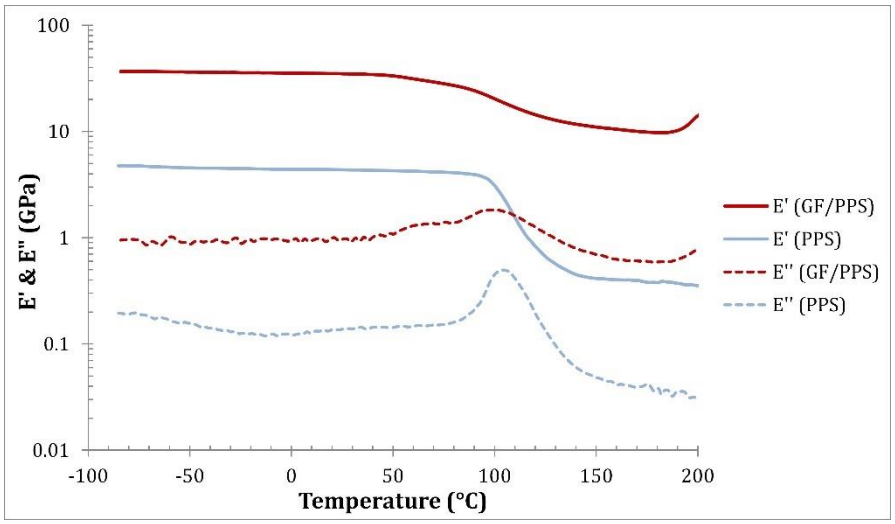

Figure 2.3. Storage modulus (E′) and loss modulus (E″) as a function of temperature for GF/PPS and neat PPS.

Table 2.2 shows the linear CTE values of all materials in the adherends (matrix and reinforcing fibres) and in the weldline (matrix and metal mesh). The plot in Figure 2.4 depicts the dimensional changes of the annealed PPS film during the second and the third heating curves, which are identical. The change in the slope around 95 °C is related to the glass transition, owing to the increased chain mobility in that region. Ideally, equation (2.1) should be applied in regions that do not exhibit a discontinuous jump, therefore, the CTE values corresponding to the ranges [25 °C, 90 °C] and [100 °C, 140 °C] were computed and reported. With respect to the CTE values below RT, at the moment of the experiments it was not possible to reach cryogenic temperatures due to technical issues. However, it could be assumed that the CTE values below RT would not change substantially considering the limited mobility of the polymeric chains below the glass transition temperature. In addition, in chapter 5 the TMA curve of an amorphous PPS film is shown where it can be seen that the expansion rate below RT is similar to the expansion rate above RT and below the Tg.

Table 2.2. Linear CTE values for materials in adherends and weldline.

Material	CTE (10^{-6} / °C)	Comments
PPS	45.1 (25 °C to 90 °C) 106.9 (100 °C to 140 °C)	Obtained through TMA tests
Stainless Steel 304L	17.8 (10 °C to 315 °C)	Obtained from [26]
Glass Fibres	5.0 (-)	Obtained from [27]

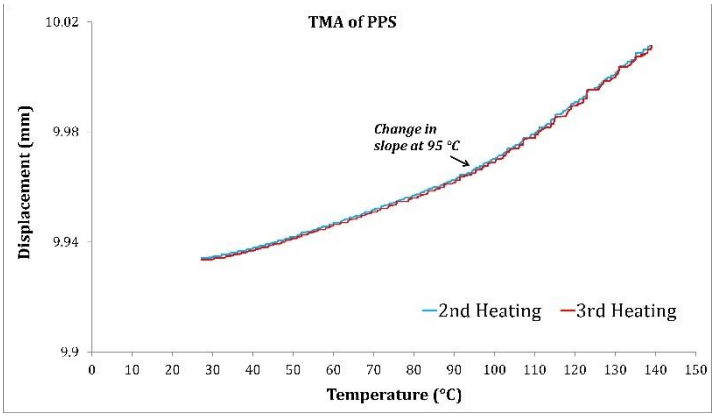

Figure 2.4. Thermal expansion of PPS as resulting from TMA tests (2 °C/min).

2.3.1.2. In-plane shear tests

Figure 2.5 shows that the temperature increase had a detrimental effect in both the in-plane shear strength and the in-plane shear modulus. As seen in Figure 2.5, both the strength and modulus seemed to have a more pronounced decrease rate in the 50 °C to 90 °C range. It should be noted that in the tests at 120 °C the adhesive used to glue the strain gauges on the specimens failed at around 2% shear strain, therefore it was not possible to measure the IPS strength but only the modulus. The IPS properties are also listed in Table 2.3.

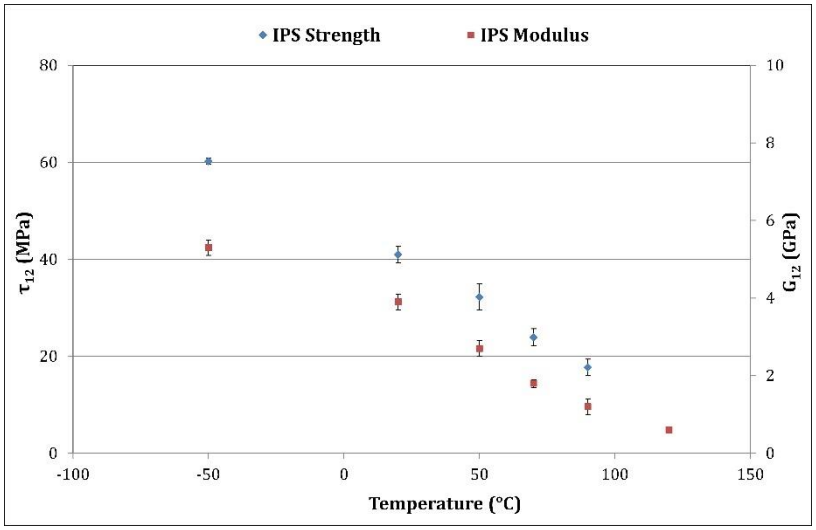

Figure 2.5. Effect of temperature on IPS properties of GF/PPS laminates. The scatter bars represent the standard deviation.

Table 2.3. Summary of in-plane shear test results on GF/PPS laminates at [-50 °C, 90 °C].

Temperature (°C)	IPS Strength (MPa)	IPS Modulus (GPa)
-50	*60.2 ± 0.4*	*5.3 ± 0.2*
20	*41.0 ± 0.4*	*3.9 ± 0.2*
50	*32.2 ± 0.4*	*2.7 ± 0.2*
70	*23.9 ± 0.5*	*1.8 ± 0.1*
90	*17.7 ± 0.3*	*1.2 ± 0.2*
120	-	*0.6 ± 0.03*

2.3.2 Characterisation of welded joints

2.3.2.1 Lap shear strength

Figure 2.6 illustrates the average values with 95% confidence intervals for the apparent LSS of the welded joints as a function of testing temperature. Table 2.4 lists the average LSS values and corresponding scatter. As it can be seen, the LSS showed an overall decreasing trend with increasing temperature, except for the region between 50 °C and 90 °C where the LSS exhibited a plateau. Therefore, the plot in Figure 2.6 could be divided into three distinct regions according to the temperature dependence of the LSS. Region A extended from -50 °C to 50 °C and featured an approximately linear decrease of LSS with increasing temperature. As it is, the LSS was found to increase in 28% between RT and -50 °C. Likewise, increasing the temperature from RT to 50 °C caused a 12% LSS decrease. Region B extended from 50 °C to 90 °C and, as previously mentioned, was characterised by a LSS plateau; the LSS remained constant with minor differences within the confidence intervals. Finally, region C, which extended from 90 °C to 150 °C, featured an approximately linear drop in LSS. Relative to RT, a 25% and 35% LSS decrease was measured at 120 °C and 150 °C, respectively.

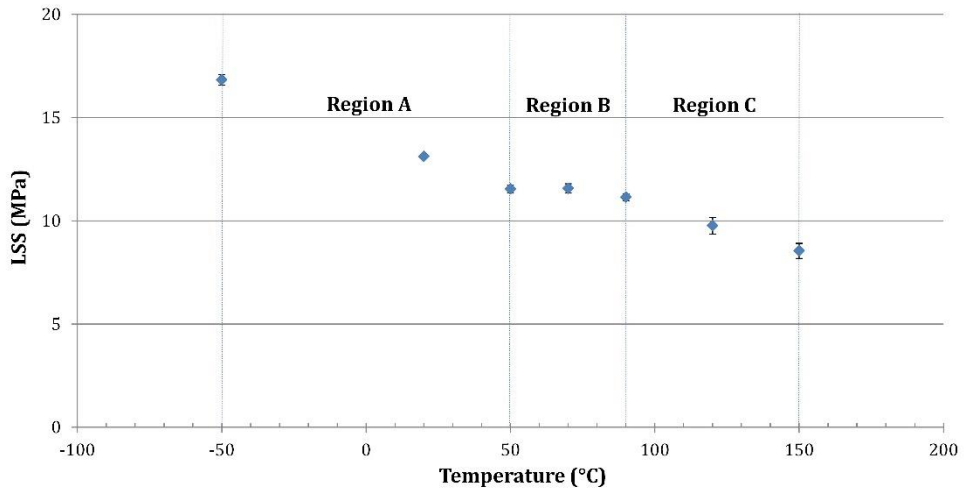

Figure 2.6. Influence of temperature on the single lap shear strength of RW GF/PPS joints. The scatter bars represent the 95% confidence intervals.

Table 2.4. Summary of SLS test results on GF/PPS laminates at [-50 °C, 150 °C].

Temperature (°C)	LSS (MPa)
-50	*16.8 ± 0.4*
20	*13.1 ± 0.4*
50	*11.5 ± 0.4*
70	*11.6 ± 0.5*
90	*11.1 ± 0.3*
120	*9.8 ± 0.6*
150	*8.5 ± 0.7*

2.3.2.2. Fractography

In order to understand the effect of temperature on the failure mechanisms of the RW GF/PPS joints, the fracture surfaces of the tested specimens were investigated. Fractographic analysis was carried out at two levels: naked-eye observation to investigate macroscopic failure features and scanning electron microscopy to investigate microscopic failure features.

Macroscopic failure features

The fracture surfaces of welded joints tested at -50 °C and RT (an example of which is shown is Figure 2.7) showed that approximately 50% of the metal mesh, mostly covered by resin and glass fibres, remained on each side of the fracture surface. Owing to the peel stress concentrations at the edges of the overlap in single lap shear joints [28] (Figure 2.8) and to the resin and fibres covering the fractured mesh, failure was believed to initiate in both adherends and to progress towards the middle of the joint overlap where mesh tear eventually occurred, as shown in the schematic in Figure 2.9. As a result of this type of failure, hereafter referred to as fracture type I, roughly the same area of mesh (between 40% and 60% of the total mesh area) was left on each mating fracture surface (Figure 2.9). The fracture surfaces of RW joints tested at T ≥ 50 °C revealed some changes in how the mesh was divided between the two mating fracture surfaces after failure.

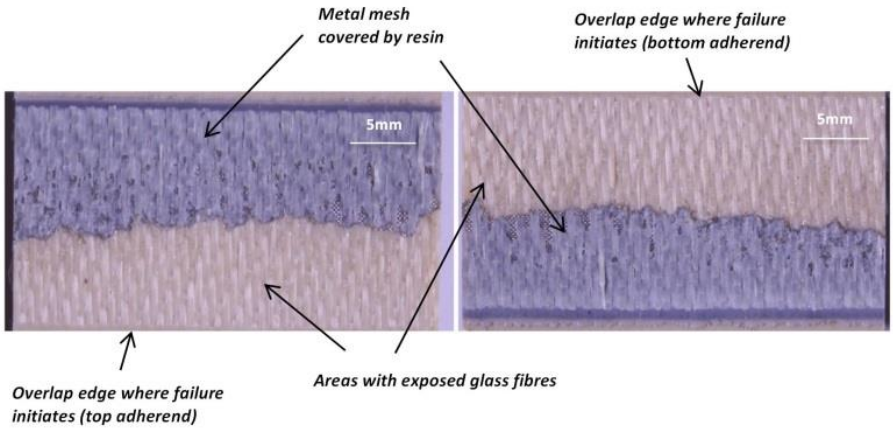

Figure 2.7. Mating fracture surfaces of a specimen tested at -50 °C. The arrows indicate the areas where the metal mesh is mostly covered by PPS resin as well as the areas with exposed glass fibres, In addition, the overlap edges where failure was initiated are also indicated.

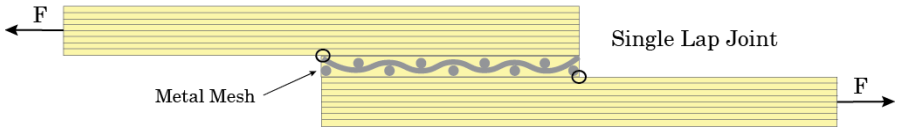

Figure 2.8. Schematic of a RW single lap shear sample with circles indicating the locations of peel stress concentrations.

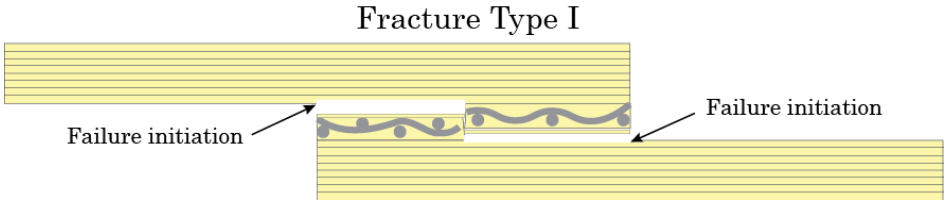

Figure 2.9. Schematic of failure observed in samples tested at -50 °C and RT: Fracture Type I (40-60% of metal mesh on one side).

Figure 2.10 illustrates the top fracture surfaces of welded joints tested at 70 °C, 90 °C and 120 °C where these changes can be observed. Consequently, two additional fracture types were defined, fracture type II (60-80% of the mesh on one of the fracture surfaces) and fracture type III (80-100% of the mesh on one of the fracture surfaces), as shown in the schematic representations in Figure 2.11.

Figure 2.10. Representative fracture surfaces of welded joints tested at 70 °C (left) showing fracture type II, 90 °C (middle) and 120 °C (right) showing fracture type III Only one fracture surface is provided per testing temperature.

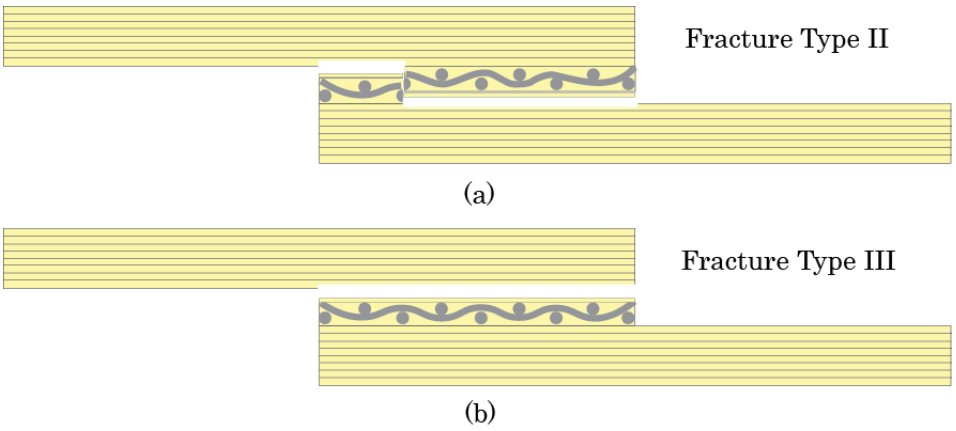

Figure 2.11. Schematic representation of failure (a) fracture type II (60-80% of metal mesh on one side) and (b) fracture type III (80-100% of metal mesh on one side).

Figure 2.12 shows the percentage of specimens that exhibited the three fracture types defined above per test temperature as well as the LSS per group of specimens (defined by fracture type and testing temperature). It can be seen that, apart from the fact that specimens tested at -50 °C and RT exclusively showed fracture type I, at 50 °C and 70 °C fracture type I was prevalent, at 90 °C the dominant fracture type was type III, while at 120 °C and 150 °C the distribution of the fracture types was more uniform. Nevertheless, there was no clear trend on a prevalent fracture type at temperatures above RT. The macroscopic failure was found to be independent of the position of the adherends during the resistance welding process. Similarly, the clamping

position of the adherends during the SLS tests had no contribution to the change in macroscopic failure. It should be noted that, as seen in Figure 2.12, the macroscopic fracture type did not seem to have any significant effect on the LSS of the welded joints.

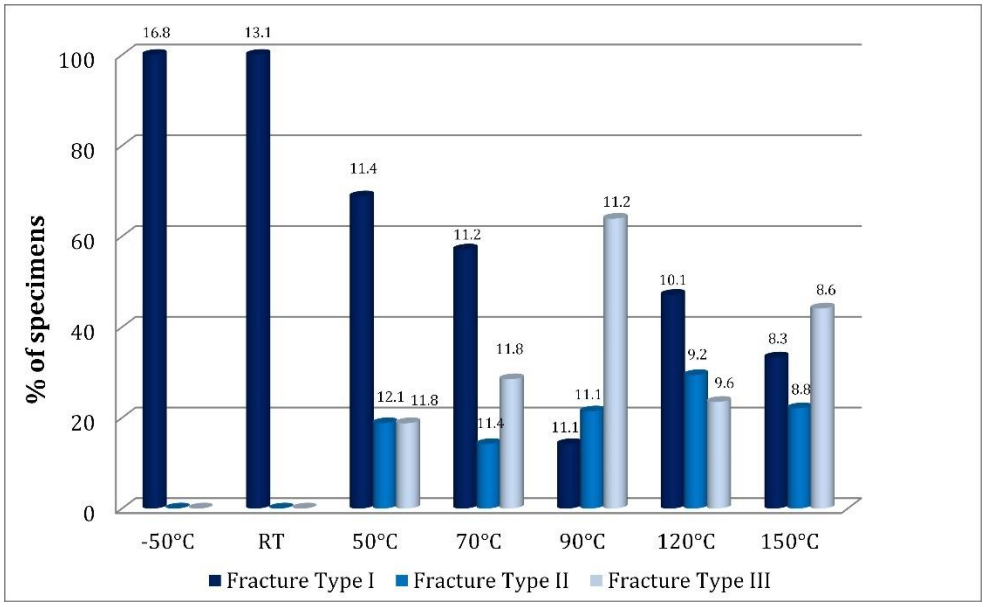

Figure 2.12. Distribution of fracture types as a function of temperature. The LSS values corresponding to each group of samples (defined by fracture type and testing temperature) are shown on top of the bars.

Microscopic failure features

All tested specimens exhibited the same key microscopic failure mechanisms regardless of the test temperature. These key mechanisms were fibre/matrix debonding and mesh/matrix debonding. Among these, fibre/matrix debonding was found to be the predominant failure mechanism at all temperatures. This is illustrated by the fracture surfaces in Figure 2.13 and Figure 2.14, corresponding to a specimen tested at -50 °C and a specimen tested at 120 °C, respectively. Finally, the cross-section micrograph of a single lap shear specimen tested at RT shows that fibre/matrix debonding not only did occur at the weldline but also within the bulk of the composite in the overlap (Figure 2.15).

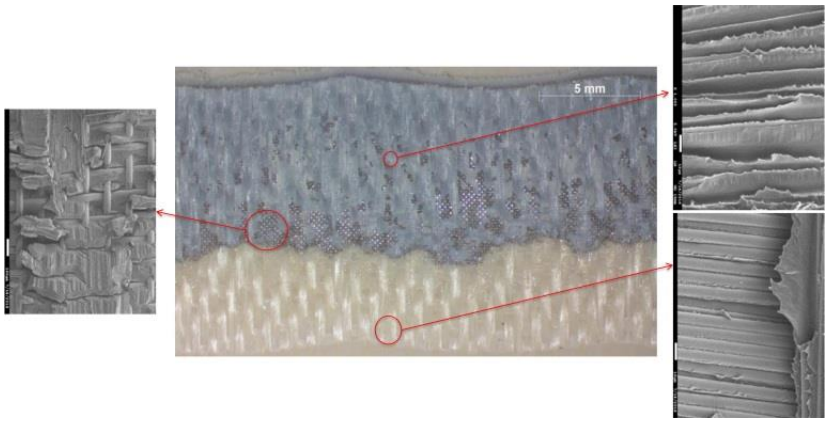

Figure 2.13. Fracture surface of specimen tested at -50 °C (centre). SEM micrographs illustrate fibre/matrix debonding (right) and mesh/matrix debonding (left). The top right SEM image illustrates fibre imprints in the resin and the bottom right SEM image illustrates debonded fibres.

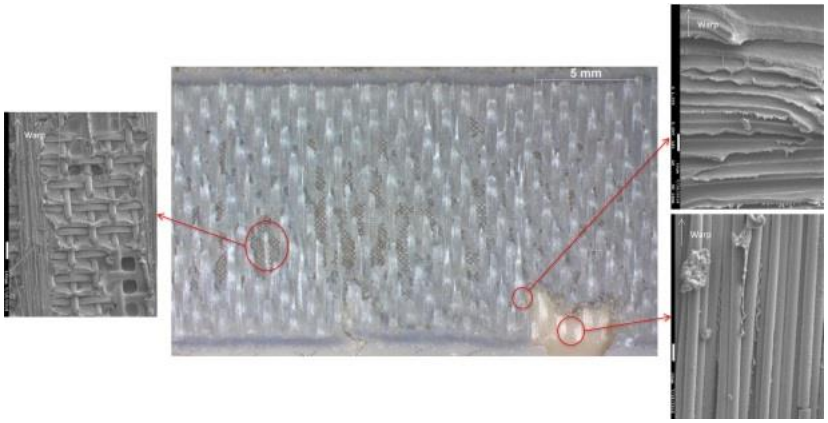

Figure 2.14. Fracture surface of specimen tested at 120 °C (centre). SEM micrographs illustrate the fibre/matrix debonding (right) and mesh/matrix debonding (left). The top right SEM image illustrates fibre imprints in the resin and the bottom right SEM image illustrates debonded fibres.

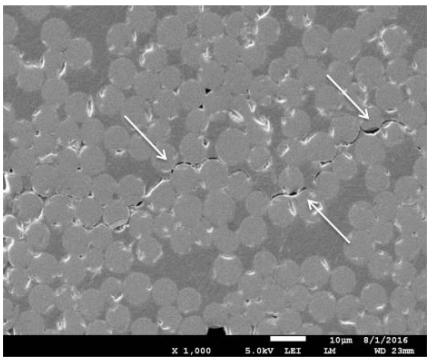

Figure 2.15. SEM image of a cross-section of specimen tested at RT showing fibre/matrix debonding. The arrows indicate the failure which occurs within the weft bundle and along the fibre/matrix interface.

2.4 Discussion

In this section the results are discussed from the perspective of the key research questions that motivated the present research, i.e. (a) is the connection between the metal mesh and the thermoplastic matrix the weakest link at the weldline when the joints are subjected to elevated temperatures and (b) how is the joint strength affected by the temperature?

Regarding the first question, even though the PPS matrix was found to expand significantly more than the metal mesh (2.5 and 6 times more, below and above its Tg, respectively), the resulting decrease in the compressive stresses on the mesh was not enough to turn the mesh/matrix connection into the weakest link in the welded joints at least up to 150 °C. This statement is supported by the fact that fibre/matrix debonding, and not mesh/matrix debonding, was found to be the primary microscopic failure mode not only at low but also at elevated testing temperatures. The relatively big differences between the melt crystallization temperature of PPS and the test temperatures are believed to favour this behaviour. Likewise, the fact that during lap shear testing the highest stresses occur at the interface between the adherend and the weldline [28] and not at the centre of the weldline, i.e. the location of the mesh, could as well play a role. However, it is acknowledged that this observation cannot be simply extended to all RW TPCs. In a recent study, Rohart et al [18] using the same heating element used in this work, carried out SLS tests on RW CF/PPS joints at temperatures ranging from 21 °C to 150 °C and measured consistently higher LSS than the LSS reported in this work. They also reported that the failure location of the RW joints was mainly at the interface

between the heating element and the matrix. The different observations between the two studies could be attributed to a higher interfacial strength between the carbon fibres and the PPS matrix compared to the interfacial strength between the glass fibres and PPS.

Regarding the second question, the strength of the welded joints showed an overall decreasing trend with increasing temperature with the exception of the 50 °C to 90 °C range, where the weld strength remained fairly constant. The test temperature was found to affect to some extent the macroscopic failure type, however there seemed to be no apparent link between the macroscopic failure type and the weld strength. Microscopic failure features pointed at fibre/matrix interfacial strength as the main responsible for the strength of the welded joints at all test temperatures. Consequently, fibre/matrix interfacial strength was identified as one of the potential main factors affecting the thermal evolution of the weld strength. Moreover, given the sensitivity of lap shear tests to the mechanical properties of adherends and weldline [29], the stress state at the overlap was identified as another potential influential factor. It follows a more detailed discussion on the effect of temperature on these two factors.

In thermoplastic composites, fibre/matrix interfacial strength is often related to the residual thermal stresses caused during manufacturing as well as the static friction at the fibre/matrix interface which result in mechanical interlocking between the matrix and the fibres [30][31]. Residual thermal stresses, more specifically residual compressive stresses on the surface of the fibres, originate from the CTE mismatch between fibres and matrix, similarly to the mesh/matrix case discussed before. Consequently, the residual compressive stresses are directly proportional to the elastic modulus of the matrix, the CTE difference between matrix and fibres and the difference between the melt crystallization temperature of the matrix, i.e. stress-free temperature, and the service temperature [30][32]. An increase in the testing temperature, hence, tends to decrease the residual compressive stress on the fibres through a decrease in the temperature gap (ΔT) between stress-free and service temperatures. However, based on the analysis of the storage modulus of PPS (see Figure 2.3), the biggest decrease in the compressive stresses is caused by the fact that the elastic modulus of the matrix is one order of magnitude lower above the glass transition temperature. The increase of the CTE difference between fibres and matrix above the Tg of PPS (see Table 2.2) is, on the contrary, too small to counteract the effect of the drop in elastic modulus. The results of the in-plane shear tests (see Figure 2.5) did show a decrease in IPS strength, which according to [23] can be related to a decrease in the fibre/matrix interfacial strength, with increasing temperature. Interestingly the IPS strength decreased at a faster pace in the 50 °C to 90 °C temperature range, which does not seem to be related to the above-mentioned changes in the residual compressive stresses on the fibres. It might, however, result from potential temperature-induced changes in the sizing of the glass fibres which could affect its interaction with either the matrix or fibres themselves. The premature decrease in storage modulus and secondary peak in the loss modulus observed in the same temperature range for the GF/PPS composite (see Figure 2.3) are in line with this hypothesis since they seem to indicate the presence of sizing on the glass fibres with a lower Tg than the PPS matrix [31][32]. Further research is however needed to fully understand this behaviour. It is also worth noticing that the IPS modulus followed the same trend as the IPS strength. The fact that the storage modulus of PPS remains virtually constant from -50 °C till 90 °C suggests that the decrease in IPS modulus could as well be linked to the decrease in fibre/matrix interfacial strength. This hypothesis is in line with the findings of some researchers [31][34], however, there is no consensus in literature regarding the presence or absence of a relationship between the fibre/matrix interfacial strength and the in-plane shear modulus [23].

With regard to the stress state in the joint overlap during single lap shear testing, it is well known that the geometry of a single lap joint results in non-uniform stress distributions with

shear and peel stress concentrations at the edges of the overlap [17][35]. Of these, the peel stresses are the most critical ones in composite welded joints [36]. The magnitude of the shear and peel stress peaks is dependent, among other factors, on the deformations in the adherends and on the deformation in the adhesive, i.e. the weldline. In particular, secondary bending of the adherends, which results from the eccentric load path inherent to the sample geometry, is known to increase the peel stresses at the edges of the overlap [35][37]. Likewise, the longitudinal deformation of the adherends and of the adhesive affect how uniform the shear stress distribution is at the overlap. Increasing the stiffness of the adherends and/or decreasing the stiffness of the adhesives results in more uniform and hence more favourable shear stress distributions at the overlap [29]. Finally, the shear deformation of the adherends causes the stresses to be distributed over a larger area hence decreasing the shear stress concentrations [38]. Consequently, by affecting the stiffness of the adherends and of the weld line, the testing temperature has an effect on the distribution of the shear stresses along the overlap and the magnitude of the peel stress peaks at the edges of the overlap. Particularly, in the -50 °C to 50 °C testing temperature range the decrease in IPS modulus of the adherends with increasing temperature can be expected to have a positive effect in the load distribution within the overlap by decreasing the shear stress concentrations at the overlap edges. Between 50 °C and 90 °C, the decrease in IPS modulus and hence its positive effect in the shear stress distribution is more pronounced. Above 90 °C the positive effect brought along by the decrease in IPS modulus is counteracted by the increase in peel stresses resulting from a significant decrease in the storage modulus of the adherends.

Consequently, in the whole temperature range considered in this study (i.e. -50 °C to 150 °C) the fibre/matrix interfacial strength decreased with increased temperature. Given the fact that fibre/matrix debonding was found to be the major failure mechanism of the welded joints, the stress values resulting in failure of the welded joints decreased with increased temperature. This would have resulted in a continuous decrease of the lap shear strength of the welded joints with increasing temperatures if the stress distribution within the overlap had been the same for all testing temperatures. However, the sensitivity of the lap shear test to the stiffness of the welded coupons resulted in a dependence between the stress distribution at the overlap and the testing temperature which affected lap shear strength results. Particularly, the pronounced decrease in IPS modulus between 50 °C and 90 °C most likely counteracted the decrease in failure strength by decreasing the shear stress concentrations and hence caused the observed discontinuity in the lap shear strength of the welded joints.

A final remark of this chapter concerns the crystallinity degree of PPS at the weldline of the RW GF/PPS joints. Although, as mentioned in the first chapter, this work did not investigate the PPS crystallinity in relation with the process parameters, it is worth to mention that the crystallinity degree of PPS could have an impact on the weld performance depending on the process parameters. In section 2.2.2, it was estimated that the cooling rates during resistance welding of GF/PPS were close to 3 °C/s, based on previous work by Shi [21]. For such cooling rates, Cebe and Chung reported a semi-crystalline PPS [39], even though a different study reported quenching of PPS at slower cooling rates [40]. In chapter 3, the dependency of PPS crystallinity with the cooling rates is shown, where it can be seen that a cooling rate of 3 °C/s would yield semi-crystalline PPS, however, not of optimum crystallinity (i.e. highest possible as obtained by cooling rates near to 10 °C/min). This means that longer heating times coupled with lower power densities could potentially result in slower cooling rates and alter the PPS morphology at the weldline and, possibly, at the first plies of the adherends. In addition, during cooling, the weldline matrix remained above 120 °C - which is the cold crystallization temperature of PPS [40] - for approximately one minute [21], possibly adding an annealing step in the process which could have increased the PPS crystallinity. With respect to this

chapter's results, it can be argued that at 120 °C and 150 °C the 30 minutes conditioning time prior to the single lap shear tests, could have increased the crystallinity of PPS. Perhaps this was achieved only marginally, considering the expected moderate-to-high levels of crystallinity (based on the estimated cooling rates). Furthermore, considering the substantial decrease in LSS at these temperatures, it seems that while cold crystallization of PPS could have been beneficial for the fibre/matrix interfacial strength, its effect was probably eliminated due to the detrimental effects of the other factors mentioned earlier. Taking into account the unknowns of the topic of PPS crystallinity in RW joints, it is recommended to conduct a separate investigation by isolating the effects of power density and heating time on the crystallinity degree of PPS and the weld performance at various temperatures.

2.5 Conclusions

The major objective of this study was to evaluate in detail the relationships between the joint strength and the constituents of the joint, namely the glass fibres, the PPS matrix and the stainless steel mesh, under the influence of temperature. Single lap shear tests were performed at temperatures ranging between -50 °C and 150 °C to assess the strength of the welded joints, followed by a detailed fractography analysis which identified the main failure mechanisms. The following conclusions can be drawn:

- The strength of the RW joints showed an overall decreasing trend with increasing temperature, except for the region between 50 °C and 90 °C, where the weld strength remained fairly constant. At -50 °C the LSS was 28% higher than the strength at room temperature while the lowest strength was observed at 150 °C, exhibiting a 35% decrease with respect to room temperature.

- Fractographic inspection revealed that the main failure mechanism of RW GF/PPS joints at all temperatures was fibre/matrix debonding. This type of failure could be favoured by the relatively big differences between the melt crystallization temperature of PPS and the testing temperatures, and by the high stresses at the interface between the adherend and the weldline instead of the centre of the weldline, where the mesh is located. Hence, the connection between the stainless steel mesh and the PPS matrix was not the weakest link at the weldline of the single lap joint at any of the temperatures under study.

- The decrease in IPS strength with increasing temperature together with the fact that fibre/matrix debonding was found to be the main failure mechanism at all temperatures, suggested that the fibre/matrix interfacial strength was the main factor affecting the strength of the RW joints. This reduction in fibre/matrix interfacial strength was mainly attributed to the decrease in the residual compressive stresses between the glass fibres and the PPS matrix, which was even more pronounced at temperatures above Tg due to the significant drop of the PPS modulus at these temperatures.

- The stress state at the overlap was identified as a potential influential factor for the discontinuity in the lap shear strength in the temperature region between 50 °C and 90 °C. The pronounced decrease in IPS modulus could cause the stresses to be distributed over a larger area, thus, lower the shear stress concentrations which potentially could counteract the decrease in the failure strength of the welded joints caused by the decrease in fibre/matrix interfacial strength.

Bibliography

[1] Offringa A. New thermoplastic composite design concepts and their automated manufacture. JEC Composites Magazine 2010; 58 (June-July): 45-49.
[2] Ibeh CC. Thermoplastic Materials: Properties, Manufacturing Methods, and Applications. Boca Raton, FL: CRC Press, Taylor & Francis Group, 2011.
[3] Jones DP, Leach DC, Moore DR. Mechanical properties of poly(ether-ether-ketone) for engineering applications. Polymer 1985; 26(9): 1385-1393.
[4] Ageorges C, Ye L. Fusion Bonding of Polymer Composites. London: Springer, 2002.
[5] Yuan Q, Hou M, Mai YW, Ye L, Resistance welding of carbon fiber reinforced polyetherimide composite. Journal of Thermoplastic Composite Materials 2001; 14: 2-19.
[6] Hou M, Yang M, Beehag A, Mai YW, Ye L. Resistance welding of carbon fibre reinforced thermoplastic composite using alternative heating element. Composite Structures 1999; 47: 667-672.
[7] Dubé M, Hubert P, Gallet JNAH, Stavrov D, Bersee HEN, Yousefpour A. Metal mesh heating element size effect in resistance welding of thermoplastic composites. Journal of Composite Materials 2011; 46(8): 911-919.
[8] Shi H, Villegas IF, and H.E.N. Bersee HEN. Strength and failure modes in resistance welded thermoplastic composite joints: Effect of fibre-matrix adhesion and fibre orientation. Composites: Part A 2013; 55: 1-10.
[9] Ageorges C, Yen L, Hou M. Experimental investigation of the resistance welding of thermoplastic-matrix composites. Part II: Optimum processing window and mechanical performance. Composites Science and Technology 2000; 60: 1191-1202.
[10] Ageorges C, Ye L, Mai YW, Hou M. Characteristics of resistance welding of lap-shear coupons. Part III. Crystallinity. Composites Part A 1998; 29A*:* 921-932.
[11] Hou M, Ye L, Mai YW, An experimental study of resistance welding of carbon fibre reinforced polyetherimide (CF fabric/PEI) composite material. Applied Composite Materials 1999; 6: 35-49.
[12] Composite Materials Handbook. USA: Department of Defense Handbook. Vol. 3, 2002.
[13] Zhang Y, Vassilopoulos AP, Keller T. Effects of low and high temperatures on tensile behaviour of adhesively-bonded GFRP joints, Composite Structures 2010; 92: 1631-1639.
[14] Ashcroft IA, Hughes DJ, Shaw SJ, Abdel Wahab M, Crocombe A. Effect of temperature on the quasi-static strength and fatigue resistance of bonded composite double lap joints, J. Adhesion 2001; 75: 61-88.
[15] Adams RD, Coppendale J, Mallick V, Al-Hamdan H. The effect of temperature on the strength of adhesive joints. International Journal of Adhesion and Adhesives 1992; 12(3): 185-190.
[16] da Silva LFM, R.D. Adams RD. Effect of temperature on the mechanical and bonding properties of a carbon-reinforced bismaleimide. Journal of Materials: Design and Applications 2008; 222(1): 45-52.
[17] da Silva LFM, Adams RD. Joint strength predictions for adhesive joints to be used for a wide temperature range. International Journal of Adhesion and Adhesives 2007; 27: 362-379.
[18] Rohart V, Dubé M, Laberge Lebel L. Effects of temperature on the apparent lap shear strength of resistance-welded carbon fibre/thermoplastic composite joints. In: International SAMPE technical conference 2018-May; 1-10.
[19] Pocius AV. Adhesion and Adhesives Technology. Munich: Hanser 3rd edition, 2012.

[20] Ahmed TJ. Hybrid composite structures: Multifunctionality through metal fibres. Delft: Delft University of Technology, 2009.
[21] Shi H. Resistance welding of thermoplastic composites. Process and performance. Delft: Delft University of Technology, 2014.
[22] ASTM Standard D 3518/D 3518M – 94, 2001, "Standard Test Method for In-Plane Shear Response of Polymer Composite Materials by Tensile Test of a ±45° Laminate", ASTM International, West Conshohocken, PA.
[23] Madhukar MS, Drzal LT. Fiber-matrix adhesion and its effect on composite mechanical properties: I. Inplane and interlaminar shear behavior of graphite/epoxy composites. Journal of Composite Materials 1991; 25: 932-956.
[24] Wisnom MR. The effect of fibre rotation in ±45° tension tests on measured shear properties. Composites 1995; 26: 25-32.
[25] ASTM Standard D 1002 – 05, 2005, "Standard Test Method for Apparent Shear Strength of Single-Lap-Joint Adhesively Bonded Metal Specimens by Tension Loading (Metal-to-Metal), ASTM International, West Conshohocken, PA.
[26] Davis JR. Stainless Steels, ASM Specialty Handbook. Ohio: ASM International, 1994.
[27] Daniel IM, Ishai O. Engineering Mechanics of Composite Materials. New York: Oxford University Press, 2nd edition, 2006.
[28] Gleich DM, Van Tooren MJL, Beukers A. Analysis and evaluation of bondline thickness effects on failure load in adhesively bonded structures. Journal of Adhesion Science and Technology 2001; 15: 1091-1101.
[29] Guess TR, Allred RE, Gerstle FP. Comparison of lap shear test specimens. Journal of Testing and Evaluation 1977; 5: 84-93.
[30] Thomason JL, Yang L. Temperature dependence of the interfacial shear strength in glass-fibre polypropylene composites. Composites Science and Technology 2011; 71: 1600-1605.
[31] Carnevale P. Fibre-matrix interfaces in thermoplastic composites. Delft: Delft University of Technology, 2014.
[32] Rao V, Drzal LT. The temperature dependence of interfacial shear strength for various polymeric matrices reinforced with carbon fibers. Journal of Adhesion 1992; 37: 88-95.
[33] Lee S, Munro M, Scott RF. Evaluation of three in-plane shear test methods for advanced composite materials. Composites 1990; 21 (6): 495-502, 1990.
[34] Deng S, Ye L. Influence of fiber-matrix adhesion on mechanical properties of graphite/epoxy composites: II. Interlaminar fracture and inplane shear behaviour. Journal of Reinforced Plastics and Composites 1999; 18: 1041-1057.
[35] Da Silva LFM, Öchsner A. Modeling of Adhesively Bonded Joints. Heidelberg: Springer, 2008
[36] Zhao T, Palardy G, Villegas IF, Rans C, Martinez M, Benedictus R. Mechanical behaviour of thermoplastic composites spot-welded and mechanically fastened joints: a preliminary comparison. Composites Part B: Engineering 2017; 112: 224-234.
[37] Adams RD Adhesive Bonding: Science, Technology and Application. Boca Raton FL: Woodhead Publishing Limited and CRC Press LLC, 2005.
[38] Tsai MY, Oplinger DW, Morton J. Improved theoretical solutions for adhesive lap joints. Int. J. Solids Structures 1998; 35 (12): 1163-1185.
[39] Chung JS, Cebe P. Melting behaviour of poly(phenylene sulphide): 1. Single-stage melt crystallization. Polymer 1992; 33(11): 2312-2324.
[40] Kenny JM, Maffezzoli A. Crystallization kinetics of poly(phenyene sulfide) (PPS) and PPS/Carbon Fiber Composites. Polym Eng Sci 1991; 31(8): 607-614.

3 Characterisation of crystallinity at the weldline of UW CF/PPS joints

Science is the belief in the ignorance of experts.

(Richard Feynman)

This chapter is an adaptation of the paper published in the journal "Composites Part A: Science and Manufacturing", in 2019[1]*.*

In this work, the influence of ultrasonic welding on the crystallinity degree of PPS at the weldline[2] *of CF/PPS joints is discussed. In combination with chapter 4, this chapter addresses the second part of the second research question of this thesis. Two sets of welding force and vibration amplitude were used, (1000 N, 86.2 μm) and (300 N, 52.8 μm), representing short and long welding times, respectively. The evolution of temperature with time at the centre of the joint overlap was recorded using thermocouples in order to estimate the cooling rates during the welding process. The crystallinity degree of PPS was measured using differential scanning calorimetry (DSC), while the cooling rate dependency of crystallinity was determined through fast scanning calorimetry (FSC) measurements. Finally, wide-angle X-ray diffraction (WAXD) experiments were performed to estimate the average crystallite size of the matrix. The FSC experiments were performed at the University of Nantes under the guidance and assistance of Dr. Nicolas Boyard and the assistance of PhD candidate, Juliana Armidine.*

[1] *Koutras N, Amirdine J, Boyard N, Villegas IF, Benedictus R. Characterisation of crystallinity at the interface of ultrasonically welded carbon fibre PPS joints. Composites: Part A 2019; 125: 105574.*

[2] In the above publication, the term "welding interface" was used instead of the term "weldline". It was decided post-publication that "weldline" is the more appropriate term, thus, the latter was used in this thesis.

3.1 Introduction

Aerospace industry requirements of lightweight structures and cost-driven manufacturing have created the need for fast and cost-efficient joining processes. Welding of thermoplastic composites is a joining method with fast production cycles and minimal labour work. One of the most promising welding techniques is ultrasonic welding, which is classified as a friction welding technique, converting high frequency (typically 20-40 kHz) and low amplitude mechanical vibrations (2.5-250 μm) into heat via friction [1]. The produced vibrations are transverse to the weld interface and cause surface and intermolecular friction in the materials to be welded, which result in heat generation. In order to concentrate the heat generation between the adherends, energy directors (ED), which are made of the same polymer as the adherends' matrix, are placed at the weld interface [2]-[4]. The lower compressive stiffness of the energy directors compared to the composite adherends result in higher cyclic strains in the EDs during the welding process which, in turn, promote heat generation [3]-[5]. Ultrasonic welding is a very fast process, it does not require a foreign material in the weldline and it produces excellent quality joints [2].

Most of the efforts so far, have been directed at investigating the heating mechanisms and the factors affecting the ultrasonic welding process and the weld strength. Benatar and Gutowski [1] studied the heating mechanism in ultrasonic welding of carbon fibre PEEK composites, dividing the mechanism into five steps, (i) mechanics and vibration, (ii) viscoelastic heating, (iii) heat transfer, (iv) flow and wetting, and (v) intermolecular diffusion. The heating and bonding mechanisms in ultrasonic welding of neat polystyrene were investigated and it was suggested that the most rapid heating occurred at the proximity of the weld interface [6]. Furthermore, Levy et al. [7] showed that the heat initiated mainly due to friction dissipation between the energy director and the substrate in ultrasonic welding of CF/PEI composites. Amplitude of vibration and hold time were recognised as key factors affecting the weld performance [8]-[10], while higher force resulted in shorter welding times and lower welding energies [11]. Villegas demonstrated that power and displacement data can be related to weld strength and can be used for the in-situ monitoring of the welding process. Furthermore, increasing welding force and increasing vibration amplitude were found to significantly shorten the vibration times [2][3].

The cycle times of the ultrasonic welding process are extremely fast (only a few seconds), hence, the cooling rates at the weldline during ultrasonic welding are expected to be very high. Considering that the high-performance thermoplastics such as PEEK, PEKK and PPS are semi-crystalline polymers, the speed of the ultrasonic welding process could have an effect on the properties of the polymer at the weldline. In particular, when such semi-crystalline polymers are cooled very fast from the melt down to room temperature they can become predominantly amorphous or reach low levels of crystallinity degree, as it has already been reported [12]-[18]. Kenny and Maffezzoli [13] reported that quenching the PPS matrix system at cooling rates above 1.67 °C/s can yield an amorphous structure, while in a later study [14] the same authors reported that PPS was quenched at a cooling rate of 6.67 °C/s. Cebe and Chung [19] observed that cooling rates of 3.3 °C/s did not yield an amorphous PPS since the polymer was still able to crystallize during cooling. Furthermore, Ferrara et al. [20] suggested a dual-mechanism for PPS melt crystallization which resulted in a minimum crystallinity of 8% independently of the processing conditions. In recent years, the crystallization of different resin systems at very fast cooling rates has been investigated by many researchers using fast scanning calorimetry [17][18][21]-[29]. A study on the crystallization of PPS using fast scanning calorimetry revealed that PPS could not crystallize at cooling rates equal or higher than 20 °C/s [17]. Similarly, Furushima et al [28] investigated the crystallization and melting kinetics of PPS at very high

scanning rates, and found that a 30 °C/s cooling rate was sufficient to yield amorphous PPS. It is worth to mention that the cooling rates required to quench PPS were found to be lower in the older studies (at 80s and 90s) compared to the ones reported nowadays. Possibly, the different grades of PPS available nowadays are capable of crystallizing faster. Furthermore, the limited capabilities of the thermal testing techniques used in the older studies did not allow for experiments to be conducted at temperatures close to the actual temperature of maximum crystallization rate. Instead, the quenching rates were obtained by extrapolation of crystallization models developed at much lower cooling rates. Regarding other relevant semi-crystalline polymers, cooling rates higher than 100 °C/s resulted in a neat PEEK matrix with very low crystallinity levels, as shown in separate studies [16][21][30].

It has been well studied and documented that the semi-crystalline nature of thermoplastic matrix systems can influence properties such as stiffness, shear strength, fibre/matrix interfacial strength, fracture toughness and chemical resistance. Talbott et al. [16] studied the mechanical properties of PEEK and found that decreasing crystallinity led to a lower elastic modulus, lower tensile strength and lower shear strength for neat PEEK. Similar observations on the beneficial effect of crystallinity on the tensile properties of PPS and its composites have been made in past studies [17][31]. Crystallinity has also been reported to have a positive influence on the interfacial shear strength of carbon fibre reinforced PPS and carbon fibre reinforced PEEK [14][32]. On the contrary, a decrease in crystallinity has been demonstrated to cause an increase in Mode-I interlaminar fracture toughness of PEEK and PPS composites [16][33][34]. Along similar lines, in a previous study it was suggested that increasing crystallinity caused a reduction in fracture toughness of PEEK [35]. Furthermore, the fracture toughness of the weld interface of carbon fibre reinforced PPS tapes welded on carbon fabric PPS laminates, was shown to become substantially lower upon annealing [36]. In addition, it is well known that high-performance semi-crystalline thermoplastics possess excellent chemical resistance and low moisture absorption [31][37]-[40], properties that are heavily influenced by the semi-crystalline structure of these polymers [38][39][41].

Hence, considering the very fast welding times of the ultrasonic welding process and given the influence of crystallinity on the final properties of polymers and fibre reinforced polymers, the investigation of the polymer state at the weldline of ultrasonically welded thermoplastic composites joints is of significant importance. This chapter presents a characterisation of crystallinity at the weldline of UW CF/PPS joints, having two main objectives. First, to study the influence of the ultrasonic welding process parameters on the degree of crystallinity at the weldline of CF/PPS joints and, second, to determine whether it is possible to obtain a semi-crystalline weldline by appropriately modifying the process parameters. In order to determine the crystallinity degree and the average crystallite size of the matrix at the weldline, differential scanning calorimetry and wide-angle X-ray diffraction measurements on energy director films removed from the weldline after the welding process, were performed. The temperature profile at the centre of the joint overlap was measured, using thermocouples embedded in energy directors. The dependence of the crystallinity degree on the cooling rate, as well as the critical cooling rate at which the matrix crystallization is suppressed, were determined using fast scanning calorimetry. The conventional DSC technique could not be used to study the thermal transitions of polymers at very high heating and cooling rates (applicable to the ultrasonic welding process) due to its limited capabilities [27][29], therefore the FSC technique was employed.

3.2 Experimental procedure

3.2.1 Materials

The material used in this study was Cetex® woven (five harness satin) carbon fibre reinforced polyphenylene sulphide composite (CF/PPS) supplied by Ten Cate Advanced Composites, The Netherlands. Laminates measuring 580 mm x 580 mm were built from six powder-impregnated CF/PPS layers with a stacking sequence of $[(0°/90°)_3]_s$, with a nominal 50% fibre volume content. 0° is the direction of the warp yarns while 90° is the direction of the weft yarns of the woven fabric. The laminates were consolidated using a hot platen press at 320 °C and 1 MPa pressure for 20 min and subsequently cooled down at a cooling rate of 15 °C/min. The stainless steel moulds used in the press consolidation process were first cleaned with acetone, then degreased with a degreasing agent (PFQD, from Socomore) and finally coated with Marbocote 227CEE release agent. The final thickness of the consolidated laminates was 1.9 mm. Welding adherends and test specimens were cut from the consolidated laminates using a water-cooled diamond blade. Flat ED films were consolidated by placing three 0.08 mm-thick amorphous PPS films between two stainless steel moulds in a hot platen press at 270 °C and 1 MPa pressure for 20 min. The ED films were cooled down at 15 °C/min and had a final thickness of 0.24 mm.

3.2.2 Ultrasonic welding

All the joints in this study were manufactured using a 20 kHz Rinco 3000 microprocessor-controlled ultrasonic welder with maximum power output of 3000 W (Rinco Ultrasonics, Romanshorn, Switzerland) in a single lap configuration. Figure 3.1 depicts the ultrasonic welder and the welding jig, which consists of a clamp for the bottom adherend, a clamp for the top adherend, and a sliding platform which allows vertical movement of the top adherend. The welding jig also prevented shifting of the adherends during the welding process. The sonotrode serves the purpose of applying the mechanical vibrations and the force to the laminates. The mechanical vibrations are generated via a piezoelectric transducer and amplified by the booster. The piezoelectric transducer is connected to a power supply and converts the electrical signal generated by the power supply to mechanical vibrations. The complete stack of transducer-booster-sonotrode is attached to a pneumatic press which allows the vertical movement of the system. The diameter of the cylindrical titanium sonotrode was 40 mm. The adherends and the energy director were always degreased prior to welding using a degreasing agent (PFQD). The energy director was fixed on the bottom adherend prior to the welding process using an adhesive tape. The ultrasonic welding process consists of two phases, the vibration phase during which heat is generated via friction and the matrix only starts to melt and flow, and the solidification phase during which the weld is cooled down under constant pressure, achieving consolidation. The ultrasonic welding machine provides output curves of dissipated power and vertical displacement with respect to vibration time, after each weld. It is possible to control the ultrasonic welding process through the vibration time, the dissipated energy or the vertical displacement of the sonotrode. However, it is known that controlling the process through the vertical displacement (called "travel" hereafter) of the sonotrode, can produce consistently high-strength welds [2]. Therefore, the process in this study was "displacement-controlled", i.e. the vibration phase was terminated after the sonotrode travelled a certain distance (called "optimum travel").

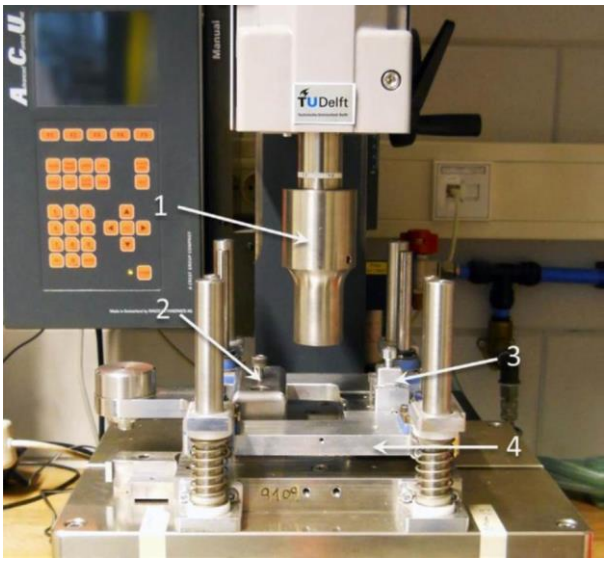

Figure 3.1. Utrasonic welder and welding jig. (1) sonotrode, (2) sliding support for top clamp, (3) top clamp, (4) bottom clamp.

The procedure that was followed in order to determine the optimum travel values has been described in previous work [2][3] and is also briefly presented here to facilitate the reader. Figure 3.2 illustrates a typical example of power and displacement curves during the vibration phase for CF/PPS samples, welded with a 0.32 mm thick energy director, using a welding force of 300 N and a vibration amplitude of 51.8 μm. The dissipated power and the displacement of the sonotrode are shown as a function of the vibration time. The vibration phase can be described in five distinct stages [2][3]:

Stage 1: The initial state of the vibration phase is characterised by a continuous increase in power (first linear, and then of decreased rate) while the displacement of the sonotrode remains constant. The end of this stage is marked by the peak in dissipated power. The energy director is initially heated up at the edges, and at the end of stage 1, the heating of the ED has already progressed into the overlap.

Stage 2: In this stage, the dissipated power decreases in a step-like fashion, while the sonotrode displacement remains constant. The energy director continues to heat up and the nucleation and growth of hot-spots result in the local melting of the ED. The nucleation of random hot-spots is governed by interfacial friction while the growth of the hot-spots by the viscoelastic heating mechanism. The duration of stage 2 is mainly depended on the welding force; the amount of initiation sites depends on the contact between the ED and the substrates which is improved for a higher welding force, leading to a shorter stage 2. The melting of the energy director means that the unmolten (solid) area of the ED decreases, which is most probably the reason for the reduction in dissipated power.

Stage 3: Both dissipated power and sonotrode displacement increase during this stage. This means that the upper adherend moves downwards, and, evidently, the weldline thickness decreases. The increase in dissipated power is attributed to the increase of the dynamic impedance of the adherends' interface when the melt fronts meet [1].

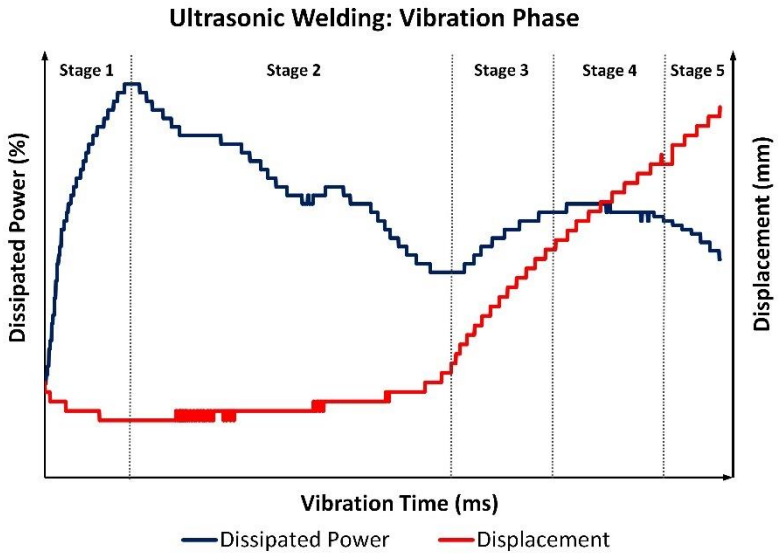

Figure 3.2. Schematic illustration of the five stages of the ultrasonic welding vibration phase. The schematic is based on power and displacement curves for CF/PPS samples welded with a 0.32 mm thick ED, under a welding force of 300 N and a vibration amplitude of 51.8 µm.

Stage 4: The sonotrode displacement continues to rise during stage 4, while the dissipated power reaches a plateau. Squeeze flow of the energy director continues while local melting of the matrix within the adherends occurs. The latter is an outcome of the heat transfer from the weldline towards the composite substrates. In this stage, the weldline thickness decreases significantly and molecular interdiffusion takes place between the surfaces of the adherends and the weldline. The power plateau can be attributed to the counteracting effects of the local melting of the adherends (power decrease) and the molten ED at the weldline (power increase). The duration of stage 4 decreases with increasing welding force due to the faster flow of the molten matrix.

Stage 5: This is the final stage of the vibration phase of the ultrasonic welding process. Here, the weldline thickness has practically reduced to "zero". It is characterised by a further increase in displacement and a reduction in dissipated power. The main phenomenon in this stage is the melting of the matrix of the adherends.

Villegas [2] demonstrated that the maximum weld strength is achieved within stage 4 and that continuing in stage 5 leads to a reduction in weld strength. By carrying out the ultrasonic welding process through all 5 stages (simply by choosing as a travel value the entire ED thickness), it is possible to identify stage 4 by the power-displacement curves (as in Figure 3.2) and determine the optimum travel. The optimum travel values used per experiment are provided in sections 3.2.3 and 3.2.4.2. As previously mentioned in the introduction of this chapter, increasing the welding force as well as the vibration amplitude result in shorter vibration times which could, possibly, influence the heat generation during the welding process and, evidently, have an effect on the cooling rates that PPS experiences. Hence, the influence of the ultrasonic welding process on PPS crystallinity at the weldline was investigated with respect to the welding force and the vibration amplitude.

Two different sets of force and peak-to-peak vibration amplitude, (1000 N, 86.2 µm) and (300 N, 51.8 µm), were used to study the effect of the process parameters on crystallinity of PPS at the weldline. The first set represents the fast process (vibration times around 400 ms) while the second set represents the slower process (vibration times around 1500 ms). The

solidification phase was characterised by the solidification time which was 4000 ms, and the solidification force which remained constant, and equal to the welding force, for all the welded joints produced in this study.

3.2.3 Temperature measurements

The temperature at the centre of the overlap was measured in order to obtain the temperature profile of the ultrasonic welding process during the vibration phase and the solidification phase. Embedding a thermocouple inside the energy director was proven to be the most effective method to measure the temperature at the weldline. Machining a groove on the adherend surface and then inserting a thermocouple inside the groove was also considered, however, the edges of the groove would act as heat concentrators and interfere with the welding process. In addition, a thermal camera could not be used because the weldline view was blocked from the welding set-up itself.

K-type thermocouples with a diameter of 0.1 mm were placed between four films of amorphous PPS. Prior to press consolidation, the thermocouples were manually fixed on the PPS films using a Rinco handheld ultrasonic welder. Figure 3.3 illustrates a schematic representation of manufacturing of EDs with embedded thermocouples. Two stainless steel moulds were used as the bottom and top moulds (cleaned following the procedure described in 3.2.1). A silicon layer of 1.95 mm thickness was placed in between the top mould and the PPS films stack for achieving a more uniform pressure distribution (the presence of the thermocouples caused a non-uniform pressure distribution). The silicon layer was sandwiched between two 25 μm-thick polyimide (Kapton, from Dupont) films (called "Kapton films" hereafter), to prevent contact with the EDs which, in turn, would cause contamination of the product. The stack was consolidated in a hot platen press following the same cycle used for the consolidation of EDs (described in section 3.2.1), having a final thickness of 0.32 mm, instead of 0.24 mm, to ensure that the thermocouples were located in the centre of the energy directors. It is worth noting here, that by using a thicker ED for the temperature measurements (0.32 mm instead of 0.24 mm) slightly lower cyclic strains would occur as it was shown by Palardy and Villegas [4].

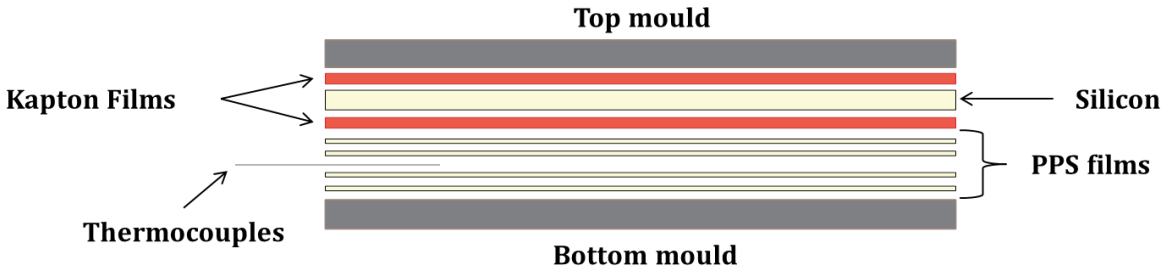

Figure 3.3. Schematic of manufacturing of energy directors with embedded thermocouples. Dimensions are not to scale.

The ED with the embedded thermocouple (ETC) was fixed on the bottom substrate using an adhesive tape, ensuring that the thermocouple tip was located at the centre of the overlap (Figure 3.4). The optimum travel for both sets of parameters was 0.22 mm. The temperature was recorded during ultrasonic welding using a Thermocouple Data Logger, TC-08, from Pico Technology, at a frequency of 10 Hz. It must be noted, that the sampling rate (1 measurement recorded per 100 ms) in conjunction with the very rapid cycle times of ultrasonic welding (typically 4-5 seconds) might have limited the precision of the measurements. The specimen series welded using a force of 1000 N and a peak-to-peak vibration amplitude of 86.2 μm are

denoted by ETC_F ("F" stands for fast process), while the specimen series welded using a force of 300 N and peak-to-peak vibration amplitude of 51.8 µm are denoted by ETC_S ("S" stands for slow process). In total, two ETC_F specimens, three ETC_S specimens, and two Kapton_ETC_S specimens were tested. Table 3.1 presents the welding conditions and the number of measurements per series.

Table 3.1. Welding conditions and number of measurements per series.

Specimen Series	Number of measurements	Welding Force (N)	Vibration Amplitude (µm)	Travel (mm)
ETC_F	*2*	*1000*	*86.2*	*0.22*
ETC_S	*3*	*300*	*51.8*	*0.22*
Kapton_ETC_S	*2*	*300*	*51.8*	*0.22*

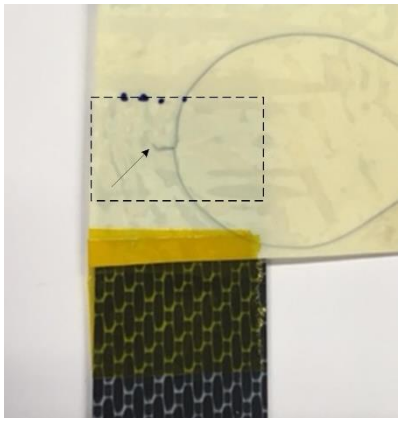

Figure 3.4. ED with embedded thermocouple prior to ultrasonic welding, positioned in such way to measure the temperature at the centre of the overlap (area enclosed within the dashed rectangle). The arrow in the picture points at the tip of the thermocouple (location of the temperature measurements).

In order to calculate the cooling rates, the temperature at which the crystallization rate is maximum needs to be known. The maximum crystallization rate of a semi-crystalline polymer occurs at a temperature approximately around the midpoint of the glass transition temperature (Tg) and the equilibrium melting temperature [31][42][43]. Close to the Tg, the molecular movement is sluggish while close to the melting temperature the crystal nucleation rate and the growth rate are very low, hence, the rate of crystallization is very slow close to both temperatures; at the midpoint between the two temperatures, the balance between the chain mobility and the nucleation rate results in the fastest crystallization rate. Chung and Cebe [44] reported that the fastest crystallization rate for PPS occurred between 170 °C and 190 °C, while Furushima et al. [28] reported the fastest rate at 160 °C, thus, it was assumed that in this study the maximum crystallization rate of PPS occurred between 160 °C and 190 °C.

3.2.4 Crystallinity assessment

3.2.4.1 Fast Scanning Calorimetry

The FSC experiments were performed using a Mettler Flash DSC 1 calorimeter, which is a chip-based fast scanning device with power compensation. The chip sensor had an active area of 500 µm and the thickness of the membrane was approximately 2 µm. The maximum heating and cooling rates can reach up to 20 000 °C/s and 5 000 °C/s, respectively. The specimens were prepared from a piece of ED under a microscope and placed in the centre of the chip sensor as illustrated in Figure 3.5. The specimen was purged with dry nitrogen gas at a flow

rate of 10 mL/min. A good thermal contact between the specimen and the sensor was achieved by, first, melting the specimen on the sensor by heating it up to 320 °C at a 10 °C/s heating rate and, subsequently, consolidating the specimen on the sensor by cooling it down to room temperature at 1000 °C/s. As a result, the preparation procedure does not allow measurements of an "as-received" specimen using the FSC technique. Hence, after the first heating/cooling cycle that was required to melt and consolidate the specimen on the sensor, a second cycle with very slow cooling equal to 0.16 °C/s was performed, in order to obtain a semi-crystalline structure of PPS. The effect of cooling rate on the crystallinity of PPS was investigated by selecting eight cooling rates, between 0.16 and 50 °C/s (Table 3.2). The rate of the heating scans was 1000 °C/s in order to prevent reorganisation of crystals which can occur upon heating [26][27]. The mass of the specimens (per sensor) ranged between 250 – 500 ng. Such low masses cannot be weighed using common balances (which normally have a readability of 0.01 mg), thus, an alternative approach has been adopted in literature. In particular, the heat capacity or the melting enthalpy can be used to estimate the specimen mass [18][21][27]. In this study, the melting enthalpy was used to estimate the specimen mass, m_{FSC}, using the following equation:

$$\boldsymbol{m_{FSC} = \frac{\Delta H_{FSC}}{\Delta H_{DSC}} \cdot m_{DSC}} \qquad \textbf{(3.1)}$$

Where:

- ΔH_{FSC}, (in J) is the measured melting enthalpy determined from the melting peak of PPS previously crystallized at 0.16 °C/s, using FSC.
- ΔH_{DSC} (in J) is the measured melting enthalpy determined from the melting peak of PPS previously crystallized at 0.16 °C/s, using the standard DSC.
- m_{DSC} is the mass of the specimen used in the standard DSC.

The degree of crystallinity, X_C, was computed using the following equation:

$$\boldsymbol{X_c = \frac{\Delta H_m}{\Delta H_f^o} \cdot 100}\ (\%) \qquad \textbf{(3.2)}$$

Where ΔH_m is the measured specific melting enthalpy in J/g and ΔH_f^o is the specific melting enthalpy of an ideal crystal ($\Delta H_f^o = 112$ J/g)[45].

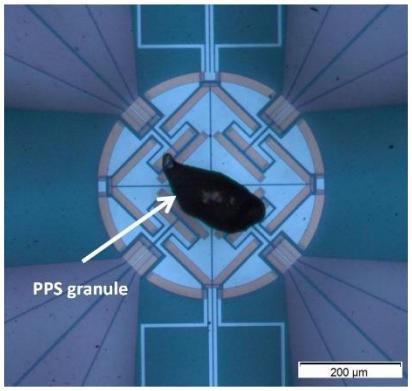

Figure 3.5. Example of a PPS granule placed at the centre of the chip sensor.

Table 3.2. Number of FSC measurements per cooling rate.

Cooling Rate (°C/s)	*0.16*	*0.33*	*1*	*1.6*	*5*	*10*	*20*	*50*
Number of Measurements	*4*	*2*	*1*	*1*	*3*	*4*	*2*	*2*

3.2.4.2 Standard DSC and WAXD analysis

Removing material from the weldline of a consolidated welded joint is necessary to perform DSC or WAXD experiments, however, it requires meticulous attention in order to prevent material from the weldline from being mixed with material from the adjacent plies (i.e. 1st ply of the adherend). For example, PPS in powder form could be obtained by grinding the cross-section of the joint but it is impossible to determine whether the powder originated from the weldline or from the resin rich areas of the adherends. Therefore, an alternative and quite simple method was used. Prior to welding, two 25 μm-thick Kapton films were fixed with tape one to each adherend and, subsequently, the ED was sandwiched between the Kapton films and fixed with an adhesive tape as well (Figure 3.6). The ultrasonic welding process was carried out as described in section 3.2.2 and the ED was easily removed from the weldline after the completion of the welding process, due to the Kapton films. The optimum travel values for the two sets of parameters, (1000 N, 86.2 μm) and (300 N, 51.8 μm), were 0.15 mm and 0.13 mm, respectively. The ED films removed after welding with high force and high vibration amplitude are denoted by ED_F and the films removed after welding with low force and low vibration amplitude are denoted by ED_S. The details of the preparation conditions of the ED films removed from the weldline (called "removed EDs" hereafter) are summarised in Table 3.3. In addition, in order to study the effect of the initial state of PPS (amorphous or semi-crystalline) on the final crystallinity of PPS, EDs made of amorphous PPS were prepared by cutting three amorphous PPS films (0.08 mm thick each) into sections of 30 mm x 30 mm and stacking them together by spot welding the four corners using a Rinco handheld ultrasonic welder. The final thickness of the amorphous EDs was 0.24 mm. The amorphous ED films were placed between the two adherends and welded using the 20 kHz Rinco 3000 ultrasonic welder (Figure 3.1). After the completion of ultrasonic welding, the EDs were removed from the weldline following the same procedure described in this section (Figure 3.6). If there is any effect of the initial state of PPS on its crystallinity degree at the weldline, the effect would be more pronounced and easier to study at slower cooling rates which were expected to be obtained by using low welding force and low vibration amplitude. Hence, the amorphous EDs were welded using a welding force of 300 N and a vibration amplitude of 51.8 μm, and are denoted by AMR_ED_S. It is important to note though, that the removed EDs were not fully representative of an ED of a consolidated welded joint produced without the interference of Kapton films. The presence of Kapton films might have an influence on the heat generation and heat transfer as the ED is in contact with the Kapton films and not with the composite adherends. On these grounds, energy directors with embedded thermocouples were placed between two Kapton films following the corresponding procedures described in sections 3.2.3 and 3.2.4.2 regarding temperature measurements and the use of Kapton films. Two specimens produced using low welding force and low vibration amplitude were tested, denoted by Kapton_ETC_S. The potential implications of using Kapton films are addressed in the discussion section.

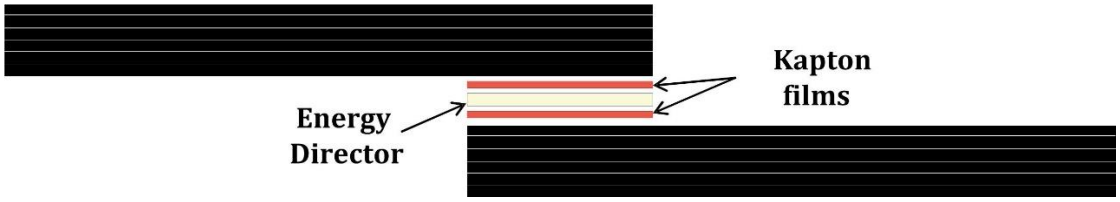

Figure 3.6. Schematic of specimen prepared for removing the energy directors from the weldline in order to perform direct crystallinity measurements. Dimensions are not to scale.

Table 3.3. Preparation conditions of removed EDs.

Specimen Series	Welding Force (N)	Vibration Amplitude (µm)	Travel (mm)	ED state prior to welding
ED_F	*1000*	*86.2*	*0.15*	*Semi-crystalline*
ED_S	*300*	*51.8*	*0.13*	*Semi-crystalline*
AMR_ ED_S	*300*	*51.8*	*0.13*	*Amorphous*

Standard DSC measurements on ED films in their initial state (after press consolidation and prior to ultrasonic welding, hereafter called "ED_Ref") and on the specimens presented in Table 3.3 were carried out in a Sapphire DSC from Perkin Elmer. The melting peak temperature and heat of fusion were calibrated prior to the experiments following indium standards. Three measurements per series were performed: the specimens were heated from 25 °C to 310 °C at 10 °C/min, in a nitrogen atmosphere, and the degree of crystallinity was determined from the heating run and computed using the following equation:

$$\boldsymbol{X_c = \frac{\Delta H_m - \Delta H_c}{\Delta H_f^o} \cdot 100} \quad (\%) \qquad \textbf{(3.3)}$$

Where ΔH_m is the measured specific melting enthalpy in J/g, ΔH_c is the specific energy associated with the cold crystallization peak in J/g, and ΔH_f^o is the specific melting enthalpy of an ideal crystal ($\Delta H_f^o = 112$ J/g) [45].

Valuable information about the state of PPS can also be obtained via measuring the change in the specific heat capacity (ΔC_p) in the glass transition region: a higher amount of the specific heat capacity could mean a higher amorphous content. ΔC_p was measured using the Perkin Elmer software.

An X-ray powder diffractometer from Bruker was used for the WAXD measurements (one per series) on amorphous PPS (80 µm thick), ED_Ref (240 µm thick), ED_F (70 µm thick) and ED_S (90 µm thick). The samples were in the shape of films. There was no WAXD measurement on AMR_ED_S due to lack of samples at the time the WAXD tests were performed. The diffractograms were [46][47] obtained using a Cobalt radiation source. The average crystallite size, D, was estimated using the Scherrer equation [46][47]:

$$\boldsymbol{D = \frac{K \cdot \lambda}{\beta \cdot \cos\theta}} \qquad \textbf{(3.4)}$$

Where K is a shape factor (approximately 0.9 [46]-[48], λ is the X-ray wavelength (1.789 Å for Cobalt), β is the full-width at the half maximum intensity of the diffraction peak and θ is the Bragg angle. It is noted, that although WAXD is not the most accurate method to measure crystal size (small-angle X-ray scattering would measure with a higher precision [49]), the results shown in this work can still be considered reliable and acceptable because they still have the correct order of magnitude and they are mainly used for comparison purposes.

3.3 Results

3.3.1 Temperature measurements

Figure 3.7 shows the temperature evolution during ultrasonic welding for one specimen per series. As it can be seen, the time-temperature relationship was non-linear, therefore it was considered inaccurate to calculate and provide a global cooling rate. Instead, the temperature region between the equilibrium melting temperature of PPS (between 298-330 °C [31]) and 160 °C was divided into smaller temperature regions, in which the time-temperature relationship was assumed quasi-linear, allowing the cooling rates to be calculated. For all series, the cooling rates decreased continuously with increasing time, and the lowest cooling rate was calculated between 190 °C and 160 °C; in this temperature region, the cooling rate for ETC_F was 41.0 ± 8.4 °C/s, for ETC_S was 16.9 ± 5.9 °C/s and for Kapton_ETC_S it was 10.9 ± 2.1 °C/s. Therefore, although a global cooling rate could not be used due to the non-linearity between time and temperature, it can be argued that the rates at which PPS was cooling down from the equilibrium melting temperature to 190 °C, were higher than the abovementioned cooling rates. Between 160 °C and 120 °C the cooling rates decreased even further, reaching 3.9 ± 0.1 °C/s and 3.5 ± 1.0 °C/s for ETC_S and Kapton_ETC_S, respectively. The cooling rate of ETC_F on the other hand was much faster, being measured around 19 ± 3.6 °C/s. An additional point to be made from these calculations is the relatively large experimental errors in most of the cooling rates which is addressed in the discussion section.

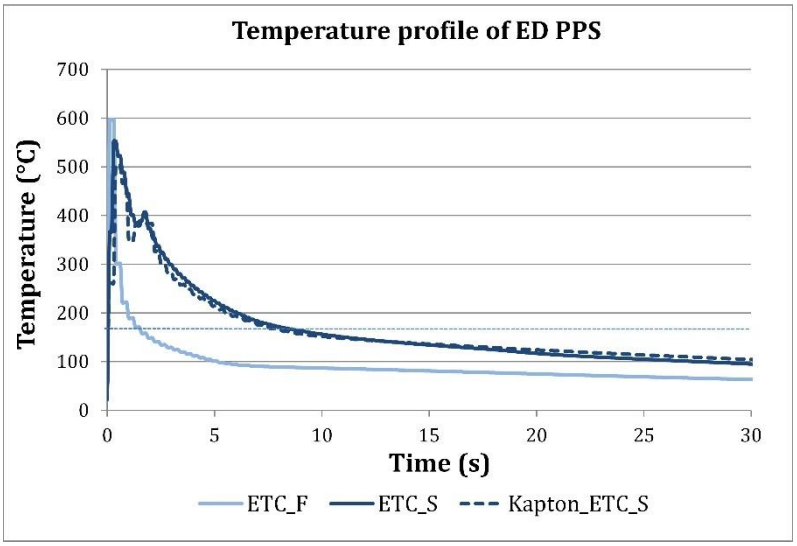

Figure 3.7. Temperature evolution during ultrasonic welding of ETC_F, ETC_S and Kapton_ETC_S. Only one specimen per series is illustrated for clarity purposes.

3.3.2 FSC measurements

Figure 3.8 shows FSC heating curves for PPS previously subjected at different cooling rates (ranging from 0.16 °C/s to 50 °C/s). In this figure, all the measurements were carried out using the same chip sensor. Four main observations regarding the melting peaks can be made from this graph. Increasing cooling rates seems (i) to result in smaller melting peaks, (ii) to shift the melting peaks to lower temperatures and (iii) to broaden the melting peaks, which were characterised by a "shoulder" shifting to lower temperatures with increasing cooling rates (above 0.33 °C/s). Finally, (iv) PPS previously cooled at 20 °C/s showed a very weak signal, exhibiting an almost negligible melting peak. Further increase of the cooling rate (at 50 °C/s) resulted in no melting peak indicating a completely amorphous structure. In addition, all

heating curves exhibited a smaller endothermic signal at lower temperatures, very close to the glass transition; this phenomenon could be attributed to the enthalpy relaxation occurring during the previous cooling and/or heating curve, as it was suggested by Furushima et al. [28]. This smaller endothermic peak shifted to lower temperatures with increases in the preceding cooling rates.

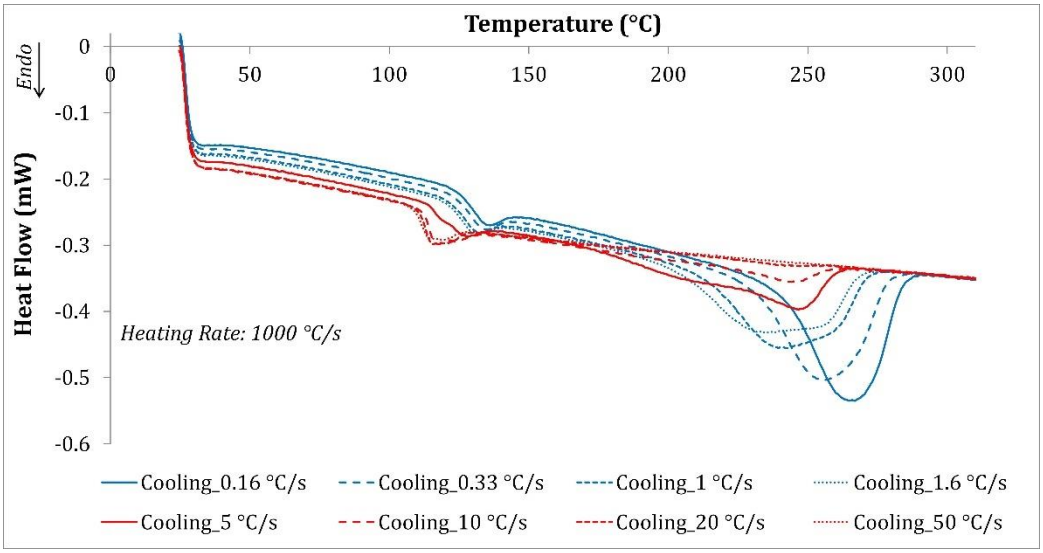

Figure 3.8. FSC heating curves of PPS (1000 °C/s) performed after cooling from 320 °C to RT at eight different cooling rates using the same chip sensor.

The dependency of X_C on cooling rate is illustrated in Figure 3.9. As it was already indicated by the smaller melting peaks in Figure 3.8, higher cooling rates resulted in lower X_C values. The highest degree of crystallinity, 28.9%, was measured for the lowest cooling rate, 0.16 °C/s. The reduction of X_C was relatively gradual up to 1.6 °C/s, where X_C was 22.2%. A further increase in cooling rate, though, caused a substantial decrease in crystallinity: at a cooling rate of 5 °C/s the crystallinity degree was 11.3% while at a cooling rate of 10 °C/s the degree of crystallinity was only 3.6%. However, it must be noted that the standard deviation for the last two values was quite large, especially for the latter. Finally, the critical cooling rate at which crystallization was suppressed was 20 °C/s, a result which is in close agreement with previous studies [17][28]. Such cooling rate yielded almost amorphous PPS, exhibiting a crystallinity degree of only 0.5%.

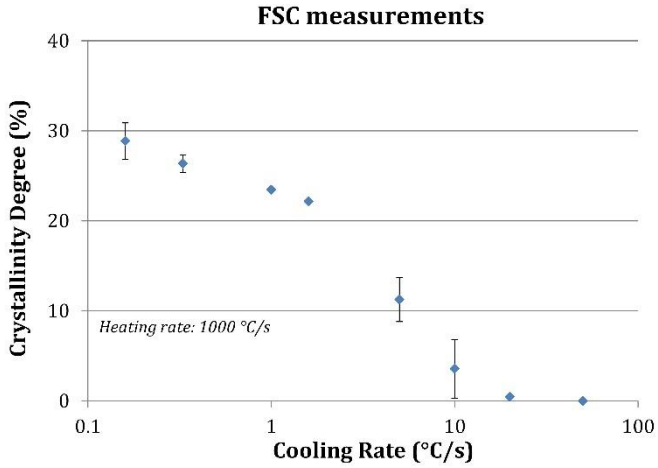

Figure 3.9. FSC measurements performed on neat PPS showing the dependence of crystallinity on cooling rate, and the critical cooling rate at which crystallization is suppressed (20 °C/s).

Furthermore, the experimental data obtained from the FSC measurements (Figure 3.9) seem to be matching quite well to an exponential function of the form:

$$y = B \cdot e^{-Ax} \tag{3.5}$$

where y is the crystallinity degree, in %, x is the cooling rate, in °C/s, while A and B are two constants that can be determined experimentally. By using the least squares method approach, the approximate solution of equation (3.5) becomes:

$$y = e^{(3.385-0.205x)} \tag{3.6}$$

Figure 3.10 illustrates the good agreement between the experimental data (shown in Figure 3.9) and the exponential fit. The coefficient of determination, R^2, was found to be equal to 0.996.

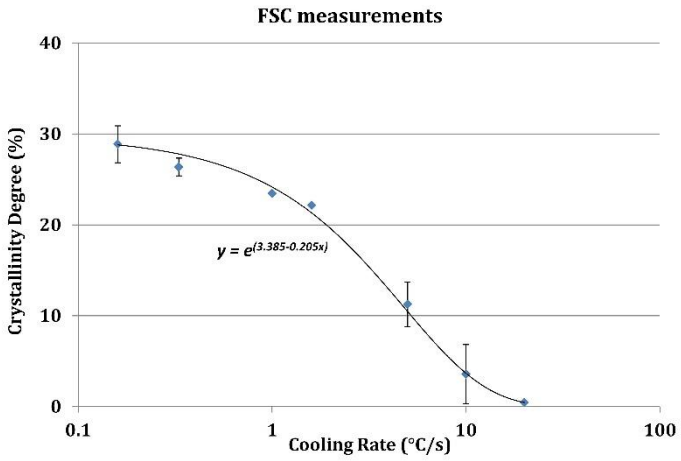

Figure 3.10. Exponential fit of the experimental data of the FSC measurements.

Equation (3.6) allows the calculation, or rather, the estimation of the degree of crystallinity of PPS at various cooling rates. Making use of equation (3.6), the crystallinity degree of PPS at the weldline of RW GF/PPS joints can be estimated as well. As it was mentioned in chapter 2, section 2.4, the cooling rate at the weldline was estimated to be around 3 °C/s. Such cooling rate would yield a crystallinity degree of around 16%. Further discussion on the effect of crystallinity degree of weldline PPS on the LSS of RW GF/PPS joints is given in chapter 6.

3.3.3 DSC and WAXD analysis of removed EDs

Figure 3.11 shows two energy directors that were removed from the weldline after welding under different conditions, where clear differences in terms of transparency can be observed. A welding force of 1000 N and a vibration amplitude of 86.2 μm produced a predominantly transparent film, with some small opaque areas (Figure 3.11). Contrarily, a welding force of 300 N and a vibration amplitude of 51.8 μm produced an opaque film with some randomly distributed small transparent areas (Figure 3.11).

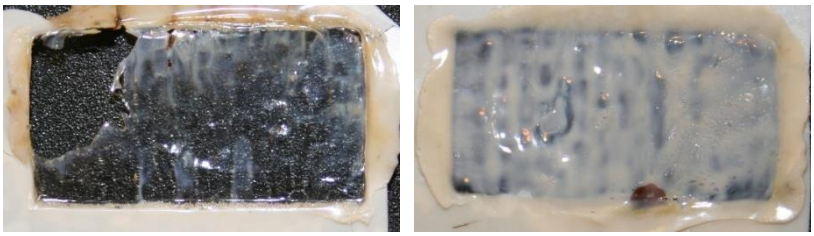

Figure 3.11. Energy directors removed after welding at 1000 N, 86.2 µm (left) and at 300 N, 51.8 µm (right). High force and high vibration amplitude produced a predominantly transparent film, while low force and low vibration amplitude produced an opaque film. A black background was used in order to facilitate observation of the films.

Transparency can provide evidence of amorphous structure while opacity of semi-crystalline structure. However, this is just a first indication since the difference in appearance could also be related to the larger thickness of the opaque film. Furthermore, it is well known that even a semi-crystalline polymer can be transparent if the crystallites are too small to scatter visible light [50]. Hence, further investigation was conducted through DSC and WAXD measurements. Figure 3.12 illustrates heating curves of standard DSC measurements carried out on removed EDs and on ED_Ref. Three measurements per ED film were performed but only one measurement per ED film is shown in Figure 3.12 for clarity purposes. As the DSC graph demonstrates, only the ED_Ref specimen did not exhibit an exothermal peak while the other three specimens exhibited an exothermal peak around 128 °C, due to cold crystallization, with the ED_F specimen showing the most pronounced one. Cold crystallization occurs above the glass transition temperature during heating from the glassy state; it was an indication of a partial crystallization during the previous specimen cooling due to a too fast cooling rate with respect to crystallization kinetics.

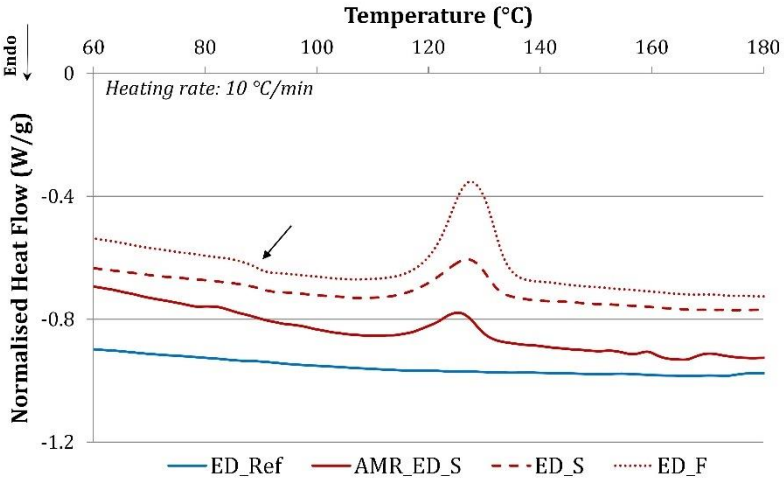

Figure 3.12. Standard DSC measurements on ED prior to ultrasonic welding (reference, i.e. after press consolidation and before welding) and on EDs removed from the weldline under different welding conditions. The graph focuses on the cold crystallization peaks of the four specimens and the glass transition region of PPS. The arrow pointing at the ED_F curve, indicates the ΔCp "step" at the glass transition. The curves are vertically shifted for better clarity.

The enthalpy associated to the cold crystallization is related to the PPS fraction which did not have time to crystallize during cooling prior to the DSC heating scan. In addition, the change of the specific heat capacity (ΔC_p) at the glass transition (around 90 °C) was larger for ED_F (0.17 ± 0.01 J/(g·°C)) compared to ED_S (0.1 J/(g·°C)), indicating that ED_F specimens had a larger amorphous phase fraction compared to ED_S. It is noted that for ED_F, the ΔC_p value was an average of three measurements while for ED_S the specific heat capacity "step" was detectable in only one measurement. It was not possible to detect the corresponding specific

heat capacity "steps" in the other ED_S and AMR_ED_S specimens, despite the use of higher heating rates (20 °C/min) or the 1st derivative of the heat flow.

Figure 3.13 shows the same heating curves as Figure 3.12 but focusing only on the melting peaks of the four specimens (illustrating only the temperature range between 180 °C and 300 °C). Only one endotherm peak corresponding to the melting of PPS crystals was observed per specimen. In addition, the melting peak temperature was found to be approximately 280 °C (±1 °C) in all series. The average crystallinity degree values were calculated using equation (3.3) and are outlined in Figure 3.14. The crystallinity degree of ED_Ref was 26% and exhibited a coefficient of variation (CoV) of 6.2%. With respect to ED_Ref, low welding force and low vibration amplitude were capable of producing ED films of moderate crystallinity, 14.6% for ED_S and 17.2% for AMR_ED_S.

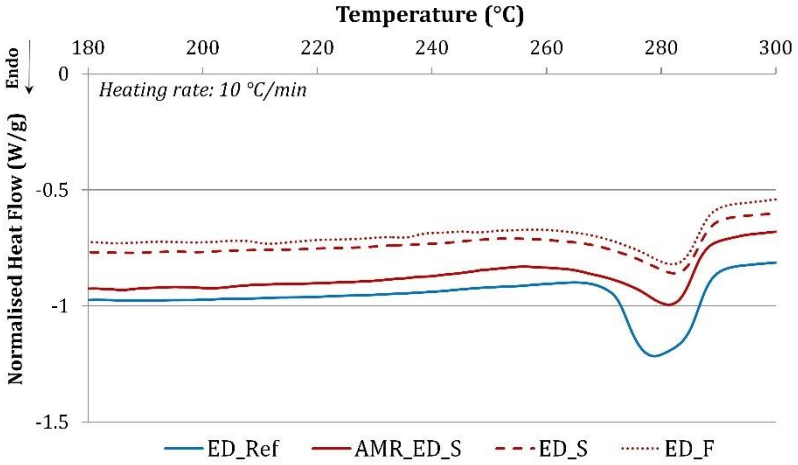

Figure 3.13. Standard DSC measurements on energy director prior to ultrasonic welding (reference, i.e. after press consolidation and before welding) and on energy directors removed from the weldline under different welding conditions. The graph focuses on the melting peaks of the four specimens. The curves are vertically shifted for better clarity.

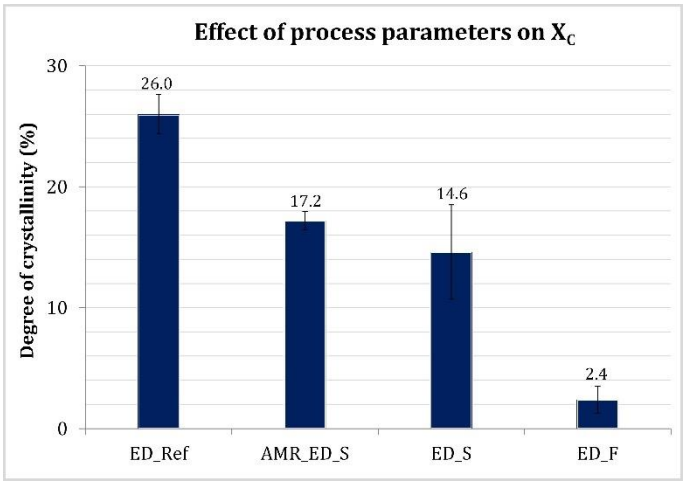

Figure 3.14. Crystallinity degree of PPS ED films calculated from Standard DSC measurements. Low welding force and low vibration amplitude produced ED films of moderate crystallinity while high welding force and high vibration amplitude produced predominantly amorphous ED films.

On the contrary, high welding force and high vibration amplitude produced a predominantly amorphous PPS, showing a crystallinity degree of only 2.4%. An additional point to be made for Figure 3.14 is the large scatter of crystallinity degree of ED_S and ED_F, showing CoV

equal to 26.7% and 45.8%, respectively. The large experimental error on the crystallinity values could probably be a result of non-uniform crystallization of the ED films during cooling, however, this was not in line with the low experimental error of AMR_ED_S (CoV equal to 4.4%). Figure 3.15 demonstrates the diffraction patterns of four specimens. The intensity of each curve was normalised with respect to the corresponding intensity of the major diffraction peak, (200, 111), and plotted against the diffraction angle, 2θ. The amorphous PPS curve was normalised with respect to the intensity of ED_Ref, in order to obtain a clear and readable diffractogram. It can be seen that ED_Ref exhibited narrower diffraction peaks compared to the removed EDs, with ED_F showing the most considerable peak broadening. The latter showed two less distinct peaks within the 2θ range of 22° to 25° and one broad peak within the 2θ range of 28° to 34°, compared to the ED_Ref and ED_S which showed four distinct diffraction peaks within the 2θ range of 28° to 34°.

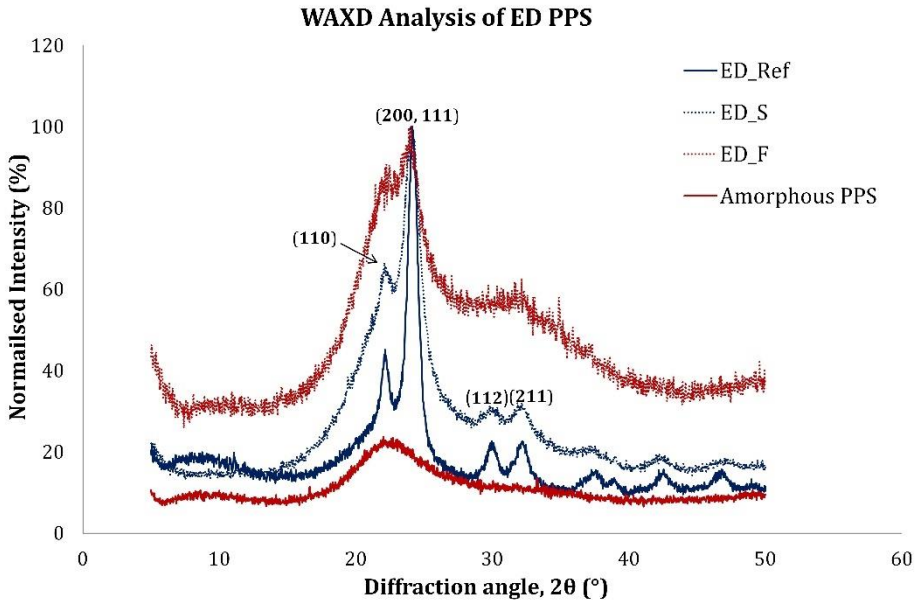

Figure 3.15. WAXD diffraction patterns showing the effect of the welding process parameters. The intensity of the ED films was normalised with respect to the intensity of the main diffraction peak (200, 111).

The amorphous PPS material exhibited a broad peak at 22°, characteristic of the diffraction peak of an amorphous material. Equation (3.4) was used to estimate the order of magnitude of the average crystallite size of the crystalline phase of PPS, and it was found that the average crystallite sizes of ED_Ref, ED_S and ED_F were 115.6 Å, 41.3 Å and 25.6 Å, respectively. In addition, the positions of the four main PPS diffraction peaks were identified and labelled in the graph [48], and were found to not be influenced by the welding conditions, remaining the same for all specimens.

3.4 Discussion

In this section, first, a brief analysis of the most probable mechanism responsible for the temperature profile at the centre of the joint overlap is presented, followed by the discussion concerning the influence of the ultrasonic welding parameters on the degree of crystallinity of PPS at the weldline. Furthermore, the additional features of the thermograms and the WAXD diffractogram of sections 3.3.2 and 3.3.3 are addressed.

The temperature profile of ED PPS during the ultrasonic welding process in Figure 3.7 showed that lowering the welding force and the vibration amplitude decreased the cooling rates significantly. The reasons for the slower cooling rates of ETC_S can be found, mainly, in the slower heat generation, $\dot{\boldsymbol{Q}}$, due to the lower vibration amplitude [6][7] which is given in the equation:

$$\dot{\boldsymbol{Q}} = \boldsymbol{\omega} \cdot \boldsymbol{\varepsilon_o^2} \cdot \boldsymbol{E''/2} \tag{3.7}$$

Where ε_o is the strain amplitude, ω is the frequency of the vibration and E″ is the loss modulus of the material. Due to the high thermal conductivity of carbon fibres, heat dissipation occurs, through the composite substrates, increasing their temperature as well. As a result, the slower heat generation would, possibly, cause a larger heat affected zone within the substrates and, essentially, cause a less effective heat transfer leading to a slower cooling of the weldline. Regarding the relatively large experimental errors of the cooling rates, one possible reason could be the low sampling rate (1 measurement point per 100 ms). Especially for the ETC_F specimens the experimental error was larger since there were less measurement points.

The standard DSC measurements on the removed EDs showed that the process parameters had a substantial impact on the crystallinity degree. Welding using a force of 300 N and a vibration amplitude of 51.8 µm yielded PPS of moderate crystallinity at the weldline while a welding force of 1000 N and a vibration amplitude of 86.2 µm resulted in predominantly amorphous PPS (Figure 3.14). Although the DSC measurements are sensitive to chain reorganisation during heating, it is not expected that it would have such a significant impact on the measured crystallinity degree of ED_S and AMR_ED_S, that would result in such a large difference with the crystallinity degree of ED_F. This statement is supported by the enthalpy associated to the cold crystallization peaks of the three series presented in Figure 10: this enthalpy for ED_F was much larger than the corresponding areas of ED_S and AMR_ED_S, indicating that a higher crystallinity degree was obtained during cooling using low welding force and low vibration amplitude. Similarly, the lower value of the specific heat capacity of ED_S associated to glass transition (about 41% lower than that of ED_F) suggests a higher crystallinity degree: the lower ΔCp value is a result of a constrained chain mobility due to the presence of crystals and a smaller amorphous phase content of ED_S. The DSC analysis was complemented by the WAXD analysis which showed that the diffraction pattern of ED_F was different than the diffraction pattern of fully amorphous PPS (Figure 3.15) while the relatively well-defined diffraction peaks of ED_S confirm the presence of a PPS crystalline phase in specimens welded under low welding force and low vibration amplitude. ED_F showed two very broad diffraction peaks, suggesting lower crystal perfection and lower crystallinity degree than ED_S. With respect to the average crystallite size of PPS, it was found that the very high cooling rates of the ultrasonic welding process caused a reduction in the average crystallite size of PPS. Further evidence supporting the notion of less perfect crystals can also be found in Figure 3.8 where it is shown that increasing cooling rates resulted in broader melting peaks, which were also shifted to lower temperatures. The appearance of broader melting peaks is an indication of a wider distribution of lamella thickness [51], while

it is well known that, under fast cooling, less perfect and/or smaller crystals are being formed at lower melt-crystallization temperatures which, in turn, result in lower melting temperatures [19].

As it was mentioned in section 3.3.1, the time-temperature relationship was non-linear, however, by dividing the temperature region between the equilibrium melting temperature and 160 °C into smaller temperature regions, it was demonstrated that the cooling rates of all series, independently of welding force and vibration amplitude, were approximately 11 °C/s or higher. Figure 3.9 showed that increasing cooling rates resulted in lower crystallinity degree values. The polymer chains need time to disentangle from the melt and organise themselves to form crystalline domains, therefore, a fast cooling rate will result in a lower crystallinity degree. Cooling rates of 10 °C/s and 20 °C/s resulted in crystallinity degrees of only 3.6% and 0.5%, respectively. The results of the FSC measurements, in conjunction with the measured cooling rates from the temperature measurements, suggest that PPS at the weldline should be predominantly amorphous regardless of the welding parameters. However, the standard DSC and WAXD measurements were not in line with the FSC measurements, as Figure 3.14 and Figure 3.15 illustrated. A few potential factors responsible for the disagreement between Figure 3.9 and Figure 3.14 (and Figure 3.15) are critically discussed in the following paragraphs.

Effect of temperature measurements

As mentioned in section 3.2.3, the EDs used to obtain the temperature profile at the weldline were thicker than the EDs removed from the weldline. However, considering the lower cyclic strains that occur in thicker EDs due to their higher stiffness [4], it is expected that the thinnest EDs (i.e. the EDs removed from the weldline) should exhibit, if not the same, even faster heating and cooling rates. Therefore, it is safe to assume that the higher thickness of ETC_S and ETC_F did not render the measured cooling rates higher than the rates encountered in ED_S and ED_F. With respect to the effect of the sampling rate (1 measurement recorded per 100 ms) on the measurement precision, most certainly some temperature values were not recorded, especially during heating, and during cooling from very high temperatures (e.g. from 400 °C to 300 °C). In addition, the peak temperature was probably not accurately detected. However, at the temperature range between 190 °C and 160 °C the rates had decreased significantly (less than 20 °C/s), allowing for sufficient measurement points to be recorded (at least 5 points per 10 °C) and to calculate the cooling rates in good approximation.

Effect of Kapton films

One possible reason for this disagreement could be the use of Kapton films in obtaining the ED_S and ED_F specimens, from which the DSC and WAXD measurements were acquired. In particular, the removed EDs were not fully representative of an ED of a consolidated welded joint produced without the interference of Kapton films. Normally, the ED is in contact with the CF/PPS substrates while in our approach, the ED was in contact with the Kapton films which could, potentially, cause different heating and cooling. Kapton_ETC_S exhibited a lower cooling rate than ETC_S, 10.9 °C/s compared to 16.9 °C/s, respectively. The differences in the cooling rates between ETC_S and Kapton_ETC_S could be attributed to the thermal insulation properties of Kapton and to the differences in friction between the Kapton - ED interface and CF/PPS - ED interface. On these grounds, it can be argued that the presence of Kapton films altered the heat generation and heat transfer at the overlap, nonetheless, 10.9 °C/s is still a very high cooling rate and incapable of producing PPS of moderate crystallinity (as a reminder, a cooling rate of 10 °C/s resulted in a crystallinity degree of 3.6%).

Annealing effect

It is well known that annealing of semi-crystalline thermoplastics (i.e. heating above Tg) leads to increased crystallinity degree and crystal perfection [52]. The changes in the crystalline regions can already occur in the first few minutes of annealing. In addition, the highest the annealing temperature, the shortest the annealing time required. Cold crystallization of PPS occurs around 120 – 130 °C which is usually the lowest annealing temperature of PPS; below that temperature the chain mobility is too low and it would require lengthy annealing times to achieve changes in crystallinity and crystal perfection. ETC_F was quenched down to 120 °C (in almost 2 seconds) while ETC_S and Kapton_ETC_S cooled down slower, in 10.3 and 11.4 seconds, respectively. Hence, an annealing effect could be possible, enhancing the crystallinity degree of ED_S and contributing to the growth of the average crystallite size. However, the studies reporting the effect of annealing on PPS, have investigated times in the order of a few minutes [52][53]. Performing experiments to isolate the effect of annealing in non-isothermal conditions for such short times is extremely complex and technically challenging. Recognising the absence of experimental proof due to technical complexities, it is suggested that annealing had a negligible effect on the crystallinity degree of ED_S due to the very short "annealing" time.

Crystal seed effect

Another possible reason for the semi-crystalline structure of ED_S could be the presence of remnant crystals in the melt. Although the temperature reached values much higher than the melting temperature of PPS (Figure 3.7), which ensured that the temperature was high enough to melt the crystals, the material remained a very short time in the melt, which could have caused PPS to partially maintain its chain conformation. Hence, there is always a possibility that some of the crystals, which pre-existed in the initial state of the ED (as received from press consolidation), did not melt or melted partially and, therefore, acted as nucleation sites during cooling (crystal seed effect). However, AMR_ED_S had a crystallinity degree of 17.2%, hence, if the remnant crystals were the main reason for the fast crystallization of PPS then AMR_ED_S should have had a much lower crystallinity degree (as the PPS energy director was amorphous in its initial state). Therefore, the (potential) presence of remnant crystals is not considered to have had a major impact on the crystallization of PPS at the weldline.

Strain-induced crystallization

One major difference between the crystallization of PPS during FSC tests and during ultrasonic welding is that the former proceeds in quiescent conditions while the latter encounters very high strain rates. The vibration frequency used in the ultrasonic welding process was 20 kHz, therefore, very high strain rates could be achieved instantaneously. When a polymer is in the melt state, the molecular chains are entangled and interpenetrated, having a random coil conformation. In quiescent conditions, the crystallization is only driven by chain mobility and supercooling level. If the kinetics of cooling is higher than the crystallization one, crystallization is prevented, leading to an amorphous PPS solid. However, under high strain the molecular chains can be oriented. The formation of nuclei is favoured which, in conjunction with the increase of nucleation density, accelerate crystallization [54], considering the same cooling conditions as in quiescent conditions. The effect of high strain rates on polymer crystallization has also been reported by several researchers [54]-[57], reinforcing our suggestion that strain-induced crystallization could explain the crystallization of PPS despite the very fast cooling rates. Nonetheless, the strain rates are linked to the time available for the molecular chains to form crystals. Although ED_F encountered higher strain rates than ED_S (and AMR_ED_S) due to the higher vibration amplitude (86.2 μm vs 51.8 μm), PPS in ED_F

was almost amorphous, exhibiting a very low degree of crystallinity (2.4%). A plausible explanation could be the shorter time of melted PPS under high strain rates for ED_F. The crystallization rate of a polymer can be accelerated due to high strain rates, however, it is likely that a very short time in the melt is not sufficient for strain-induced crystallization to occur [54]; for a melted polymer, a given time under high strain rates is required to observe an effect on crystallization kinetics. Zhang et al [57] also suggested that the crystallization rate of PPS increased with increasing shear time. Therefore, it appears that the time under high strain rates for melted PPS in ED_F was not long enough to significantly increase the crystallization rate, while the low welding force and the low vibration amplitude favoured the conditions for strain-induced crystallization to occur by decreasing the cooling rates and allowing more time in the melt.

3.5 Conclusions

This chapter presented an investigation of the crystallinity at the weldline of UW CF/PPS joints by studying the influence of welding force and vibration amplitude on the degree of crystallinity at the weldline. The results of our work can be summarised in the following conclusions:

- Temperature measurements at the centre of the overlap of UW CF/PPS joints revealed that low welding force (300 N) and low vibration amplitude (51.8 μm) decreased the cooling rates from 41 °C/s to 16.9 °C/s, compared to high welding force (1000 N) and high vibration amplitude (86.2 μm). The lower cooling rates were attributed to the slower heat generation under 300 N and 51.8 μm. It is suggested that the slower heat generation possibly caused a larger heat affected zone, resulting in a less effective heat transfer.

- The FSC experiments showed that the degree of crystallinity of PPS decreased with increasing cooling rates. Furthermore, it was shown that, in quiescent conditions, the critical cooling rate at which PPS crystallization was suppressed was 20 °C/s, exhibiting a degree of crystallinity of only 0.5%.

- DSC and WAXD measurements performed on energy director films that were removed from the weldline, showed that the ultrasonic welding process parameters had a significant impact on the crystallinity degree of PPS and its crystal perfection. High welding force (1000 N) and high vibration amplitude (86.2 μm) produced predominantly amorphous PPS and imperfect crystals, while low welding force (300 N) and low vibration amplitude (51.8 μm) were capable of increasing the crystallinity to moderate levels as well as the crystal perfection. Although the crystallinity degree and the crystal perfection were not as high as in the initial state of the PPS energy directors (i.e. prior to ultrasonic welding), it was clear from the DSC thermograms and the WAXD diffractogram that PPS had obtained a semi-crystalline structure. A possible explanation for the PPS capability to crystallize despite the very high cooling rates at the centre of the overlap, is the significantly high strain rates involved in the ultrasonic welding process which are suggested to have induced PPS crystallization. The orientation of the molecular chains in the melt due to high strain rates could have facilitated crystal formation and accelerated PPS crystallization. Hence, it was shown that by appropriately modifying the welding force and the vibration amplitude it was possible to obtain a semi-crystalline weldline.

Bibliography

[1] Benatar A, Gutowski TG. Ultrasonic welding of PEEK graphite APC-2 composites. Polym Eng Sic 1989; 29(23): 1705-21.
[2] Villegas IF. Strength development versus process data in ultrasonic welding of thermoplastic composites with flat energy directors and its application to the definition of optimum processing parameters. Composites: Part A 2014; 65: 27-37.
[3] Villegas IF. In situ monitoring of ultrasonic welding of thermoplastic composites through power and displacement data. J Thermoplast Compos Mater 2015; 28: 66-85.
[4] Palardy G, Villegas IF. On the effect of flat energy directors thickness on heat generation during ultrasonic welding of thermoplastic composites. Comp Interfaces 2017; 24:2, 203-214.
[5] Potente H. Ultrasonic welding – principles and theory. Mater De 1984; 5(5): 228-34.
[6] Tolunay MN, Dawson PR, Wang KK. Heating and bonding mechanisms in ultrasonic welding of thermoplastics. Polym Eng Sci 1983; 23(13): 726-33.
[7] Levy A, Le Corre S, Villegas IF. Modeling of the heating phenomena in ultrasonic welding of thermoplastic composites with flat energy directors. J Mater Process Technol 2014; 214: 1361-1371.
[8] Liu SJ, Chang IT. Optimizing the weld strength of ultrasonically welded nylon composites. J. Compos Mater 2002; 36: 611-624.
[9] Liu Sj, Chang IT, Hung SW. Factors affecting the joint strength of ultrasonically welded polypropylene composites. Polymer Composites 2001; 22(1): 132-141.
[10] Benatar A, Eswaran RV, Nayar SK. Ultrasonic Welding of thermoplastics in the near-field. Polymer Engineering and Science 1989; 29(23): 1689-1698.
[11] Barroso M, Villegas IF, Bersee HEN. Optimizing ultrasonic welding of carbon-fibre reinforced polyetherimide. JEC Mag 2012; 70: 54-58.
[12] Brady DG. The crystallinity of poly(phenylene sulfide) and its effect on polymer properties. Journal of Applied Polymer Science 1976; 20: 2541-2551.
[13] Kenny JM, Maffezzoli A. Crystallization kinetics of poly(phenyene sulfide) (PPS) and PPS/Carbon Fiber Composites. Polym Eng Sci 1991; 31(8): 607-614.
[14] Maffezzoli A, Kenny JM, Nicolais L. A macrokinetic approach to crystallization modelling of semicrystalline thermoplastic matrices for advanced composites. J. Mat. Sci 1993; 28 (18): 4994-5001.
[15] Gao SL, Kim JK. Cooling rate influences in carbon fibre/PEEK composites. Part 1. Crystallinity and interface adhesion. Composites: Part A 2000; 31: 517-530.
[16] Talbott MF, Springer GS, Berglund LA. The effects of crystallinity on the mechanical properties of PEEK polymer and graphite fiber reinforced PEEK. J Comp Mater 1987; 21: 1056-1081.
[17] Grouve WJB, Vanden Poel G, Warnet LL, Akkerman R. On crystallization and fracture toughness of poly(phenylene sulphide) under tape placement conditions. Plastics, Rubber and Composites 2013; 42(7): 282-288.
[18] Furushima Y, Kumazawa S, Umetsu H, Toda A, Zhuravlev E, Schick C. Melting and recrystallization kinetics of poly(butylene terephthalate). Polymer 2017; 109: 307-314.
[19] Chung JS, Cebe P. Melting behaviour of poly(phenylene sulphide): 1. Single-stage melt crystallization. Polymer 1992; 33(11): 2312-2324.
[20] Ferrara JA, Seferis JC, Sheppard CH. Dual-mechanism kinetics of polyphenylene sulfide (PPS) melt-crystallization. J Thermal Analysis 1994; 42: 467-484.
[21] Tardiff X, Pignon B, Boyard N, Schmelzer JWP, Sobotka V, Delaunay D, Schick C. Experimental study of crystallization of polyetheretherketone (PEEK) over a large temperature range using a nano-calorimeter. Polymer Testing 2014; 36: 10-19.
[22] Schick C, Mathot V. Fast Scanning Calorimetry. Springer, 2016.

[23] Gradys A, Sajkiewicz, Adamovsky S, Minakov A, Schick C. Crystallization of poly(vinylidene fluoride) during ultra-fast cooling. Thermochim Acta 2007; 461: 153-157.
[24] Zhuravlev E, Madhavi V, Lustiger A, Androsch R, Schick C. Crystallization of polyethylene at large undercooling. ACS Macro Lett 2016; 5: 365-370.
[25] Gradys A, Sajkiewicz P, Zhuravlev E, Schick C. Kinetics of isothermal and non-isothermal crystallization of poly(vinylidene fluoride) by fast scanning calorimetry. Polymer 2016; 82: 40-48.
[26] Toda A, Androsch R, Schick C. Insights into polymer crystallization and melting from fast scanning chip calorimetry. Polymer 2016; 91: 239-263.
[27] Schawe JEK. Influence of processing conditions on polymer crystallization measured by fast scanning DSC. J Therm Analysis Calorimetry 2014; 116: 1165-1173.
[28] Furushima Y, Nakada M, Yoshida Y, Okada K. Crystallization/melting kinetics and morphological analysis of polyphenylene sulfide. Macro Chem Phys 2018; 219(2): 1700481.
[29] Furushima Y, Schick C, Toda A. Crystallization, recrystallization, and melting of polymer crystals on heating and cooling examined with fast scanning calorimetry. Polymer Crystallization 2018; 1: e1005.
[30] Velisaris CN, Seferis JC. Crystallization kinetics of polyetheretherketone (PEEK) matrices. Polym Eng Sci 1986; 26(22): 1574-1581.
[31] Spruiell JE, Janke CJ. A review on the measurement and development of crystallinity and its relation to properties in neat poly(phenylene sulfide) and its fiber reinforced composites. Technical Report, Oak Ridge National Laboratory, 2004.
[32] Schulz E, Kalinka G, Auersch W. Effect of transcrystallization in carbon fiber reinforecd poly(p-phenylene sulfide) composites on the interfacial shear strength investigated with the single fiber pull-out test. J Macromol Sci Part B 1996; 35(3-4): 527-546.
[33] Gao SL, Kim JK. Cooling rate influences in carbon fibre/PEEK composites. Part II: interlaminar fracture toughness. Composites: Part A 2001; 32: 763-774.
[34] Sacchetti F, Grouve WJB, Warnet LL, Villegas IF. Effect of cooling rate on the interlaminar fracture toughness of unidirectional carbon/PPS laminates. Eng Fract Mech 2018; 203: 126-136.
[35] Karger-Kocsis J, Friedrich K. Temperature and strain-rate effects on the fracture toughness of poly(ether ether ketone) and its short glass-fibre reinforced composite. Polymer 1986; 27: 1753-1760.
[36] Grouve WJB, Warnet LL, Rietman B, Akkerman R. On the weld strength of in situ placed reinforcements on weave reinforced structures. Composites: Part A 2012; 43: 1530-1536.
[37] Stober EJ, Seferis JC. Fluid sorption characterization of PEEK matrices and composites. Polym Eng Sci 1988; 28(9): 634-639.
[38] Stober EJ, Seferis JC, Keenan JD. Characterization and exposure of polyetheretherketone (PEEK) to fluid environments. Polymer 1984; 25: 1845-1852.
[39] Ma CCM, Lee CL, Tai NH. Chemical resistance of carbon fiber reinforced poly(ether ether ketone) and poly(phenylene sulfide) composites. Polym Comp 1992; 13(6): 435-440.
[40] Ma CCM, Lee CL, Chang MJ, Tai NH. Hygrothermal behaviour of carbon fiber reinforced poly(ether ether ketone) and poly(phenylene sulfide) composites. I. Polym Comp 1992; 13(6): 448-453.
[41] Wolf C, Flu H. Stress-enhanced transport of toluene in poly aryl ether ether ketone (PEEK). J Polym Sci: Part B: Polym Phys 1996; 34: 75-82.

[42] Sperling LH. Introduction to physical polymer science. Pennsylvania: Wiley-Interscience, 1986.
[43] Hu W. Polymer physics: A molecular approach. Cambridge: Spinger, 2012.
[44] Chung JS, Cebe P. Crystallization and melting of cold-crystallized poly(phenylene sulfide). J Polym Sci: Part B: Polym Phys 1992; 30: 163-176.
[45] Huo P. Cebe P. Effects of thermal history on the rigid amorphous phase in poly(phenylene sulfide). Colloid Polym Sci 1992; 270: 840-852.
[46] Qazi SJS, Rennie AR, Cockcroft JK, Vickers M. Use of wide-angle X-ray diffraction to measure shape and size of dispersed colloidal particles. J Colloid Interface Science 2009; 338: 105-110.
[47] Wu D, Zhou C, Fan X, Mao D, Bian Z. Morphology, crystalline structure and isothermal crystallization kinetics of polybutylene terephthalate/montmorillonite nanocomposites. Polymer & Polymer Composites 2005; 13(1): 61-71.
[48] Lee TH, Boey FYC, Khor KA. X-Ray diffraction analysis technique for determining the polymer crystallinity in a polyphenylene sulfide composite. Polym Comp 1995; 16(6): 481-488.
[49] Borchert H. Shevchenko EV, Robert A, Mekis I, Kornowski A, Grübel, Weller H. Determination of nanocrystal sizes: A comparison of TEM, SAXS, and XRD studies of highly monodisperse $CoPt_3$ particles. Langmuir 2005; 21: 1931-1936.
[50] Starkweather Jr HW, Brooks RE. Effect of spherulites on the mechanical properties of Nylon 66. J Appl Polym Sci 1959; 1(2): 236-239.
[51] Lauritzen Jr JI, Hoffman JD. Extension of theory of growth of chain-folded polymer crystals to large undercoolings. J Appl Phys 1973; 44(10): 4340-4352.
[52] Ostberg GM, Seferis JC. Annealing effects on the crystallinity of polyetheretherketone (PEEK) and its carbon fiber composite. J Appl Polym Sci 1987; 33: 29-39.
[53] Arici A, Sinmazcelik T, Capan L, Yilgor I, Yilgor E. Influence of annealing on the performance of short glass fiber-reinforced polyphenylene sulfide (PPS) composites. J Comp Mat 2005; 39 (1): 21-32.
[54] Chien MC, Weiss RA. Strain-induced crystallization behavior of poly(ether ether ketone) (PEEK). Polym Eng Sci 1988; 28(1): 6-12.
[55] Rao IJ, Rajagopal KR. A study of strain-induced crystallization of polymers. International Journal of Solids and Structures 2001; 38: 1149-1167.
[56] Yoon WJ, Myung HS, Kim BC, Im SS. Effect of shearing on crystallization behavior of poly(ethylene naphthalate). Polymer 2000; 41: 4933-4942.
[57] Zhang RC, Xu Y, Lu A, Cheng K, Huang Y, Li ZM. Shear-induced crystallization of poly(phenylene sulfide). Polymer 2008; 49: 2604-2613.

4 Nanoindentation study of UW CF/PPS joints

I would rather have questions that can't be answered
than answers that can't be questioned.

(Richard Feynman)

The work presented in this chapter complements the work shown in chapter 3, regarding the effect of the ultrasonic welding process on the crystalline structure of the matrix at the weldline. In this work, the influence of the ultrasonic welding process parameters, namely the welding force and the vibration amplitude, on the PPS elastic modulus and hardness at the weldline and at the adherends of CF/PPS welded joints is evaluated. The assessment was entirely carried out through nanoindentation measurements. The formation and the true extent of a heat affected zone inside the adherends is also discussed. Finally, the nanoindentation technique is evaluated as a potential characterisation technique for thermoplastic composites welded joints.

4.1 Introduction

In the previous chapter it was shown that the crystallinity degree of PPS in the weldline of CF/PPS joints was affected by the welding process. A high welding force (1000 N) and high vibration amplitude (86.2 μm) resulted in short welding times and predominantly amorphous PPS while a low welding force (300 N) and low vibration amplitude (51.8 μm) resulted in longer welding times and PPS of moderate crystallinity. Although the results generated in chapter 3 are considered reliable, the experiments were carried out on ED films which were removed from the weldline. Ideally, the crystallinity degree of PPS would be measured on a consolidated welded joint in order to obtain a more representative measurement of the weldline, thus, a different technique is required for such purpose. In addition, using the approach followed in chapter 3 it was possible to remove material only from the weldline but not from the plies of the adherends that would allow to investigate the potential presence of a heat affected zone. The HAZ is an area within the bulk of the laminate that is affected by the welding process. It is known that during welding it is not only the weldline that heats up but also the adherends [1][2]. Heat can transfer through the laminate and depending on the process parameters it can affect not only the plies adjacent to the weldline but also plies deeper in the laminate [1][2].

A promising technique that has been established as an efficient method of direct measurements of elastic modulus and hardness at a nano-scale, is nanoindentation [3]-[14]. It is important to note, though, that measurements at smaller scales usually yield higher values than the respective bulk properties [5]. Considering the correlation between the crystallinity degree and the elastic modulus and hardness of the matrix [15]-[18], nanoindentation seems as an effective method to evaluate the degree of crystallinity, while at the same time it provides modulus and hardness data that could be used in numerical and analytical models of thermoplastic composites welded joints. There is no clear consensus in literature on the capability of nanoindentation as a crystallinity degree measurement method [3][4]. Iqbal et al [3] reported that neat PEEK exhibited a bimodal character in its modulus and hardness response which they associated with amorphous and crystalline regions. The decreasing modulus and hardness were attributed to softer (amorphous) regions and a method to calculate the crystallinity was suggested. The elastic modulus and hardness of neat PEEK were also investigated by Voyiadjis et al [4] who suggested that the approach of Iqbal's to estimate the matrix crystallinity was incorrect and that nanoindentation cannot be used for quantitative measurements of crystallinity. However, the authors [4] recognised the capability of nanoindentation to qualitatively evaluate the crystallinity of a polymer through the modulus and hardness measurements.

On these grounds, nanoindentation was selected as the technique to characterise the weldline and the adherends of the UW CF/PPS joints. In order to complement the results of chapter 3 on the effect of the ultrasonic welding process on the crystalline structure of the matrix, two main objectives are established:

(i) To investigate the influence of the welding process on the elastic modulus and hardness of PPS at the weldline and to compare the findings with the results of chapter 3.
(ii) To investigate the influence of the welding process in the adherends of the welded joints and the extent of a HAZ area inside the laminates.

In addition, the third objective of this chapter is the evaluation of the nanoindentation as a characterisation technique for thermoplastic composites welded joints.

The next section details the principles of nanoindentation and the methodology followed to evaluate the indentations and measurements of the experiments. The results and discussion section show, first, the weldline measurements, second, the adherends measurements, and, finally, a brief evaluation of the nanoindentation technique.

4.2 Experimental procedure

4.2.1 Materials

The materials used in this study together with the manufacturing method to produce the laminates were described in detail in chapter 3, section 3.2.1.

4.2.2 Sample preparation

The ultrasonic welding process was described in detail in chapter 3, section 3.2.2. The same procedure was followed in this chapter with some slight deviations, which are described below.

Owing to the thin weldline (ca. 100 µm) – which would, in turn, cause several indentations to be performed on fibres or very close to fibres – the vibration phase was not stopped at the optimum travel but at the beginning of stage 4. At the end of stage 3 the whole energy director is molten and it starts to flow. The squeeze flow of ED continues at stage 4 until the weldline thickness decreases significantly [1][19]. Thus, by terminating the vibration phase at the beginning of stage 4 a thicker weldline (ca. 150 µm) could be obtained.

Three different sets of welding force and vibration amplitude were used to study the effect of the ultrasonic welding process parameters on crystallinity of PPS at the weldline and the adherends. Each of the three sets consisted of two samples. The first two sets represent the fast process, of vibration times less than 400 ms, while the third set represents the slower process, of vibration times around 1500 ms. The solidification time was 4000 ms and the solidification force remained constant, and equal to the welding force, for all the welded joints produced in this study. In addition, a fourth series, consisting of only one sample, was prepared by thermally treating (annealing) the consolidated welded joint for 2 hours at 200 °C inside an oven, in order to obtain a weldline of high crystallinity degree. It must be noted that the samples were "free-standing" in the oven (no applied pressure) during the annealing process. The sample IDs and the details of each set of welding parameters are listed in Table 4.1. The samples that were not thermally treated are denoted by F, representing the fast welding processes, and S, representing the slow welding process. The annealed sample is denoted by A (for annealed).

Table 4.1. Preparation conditions of nanoindentation samples.

Sample	Force (N)	Vibration Amplitude (µm)	Travel (mm)	Thermal Treatment (post welding)
F1, F2	*1500*	*86.2*	*0.06*	-
F3, F4	*1000*	*86.2*	*0.06*	-
A1	*1000*	*86.2*	*0.06*	*2 hours, 200°C*
S1, S2	*300*	*51.8*	*0.06*	-

Samples F1 and F2 were welded using the same vibration amplitude – 86.2 μm – with samples F3 and F4 but with a higher welding force, 1500 N as compared to 1000 N. Although it is as not as critical as the vibration amplitude, the welding force can also alter the cooling rates. In the brief description of the vibration phase of ultrasonic welding process, given in chapter 3, it was indicated that a higher welding force can lead to shorter vibration times due to the increased contact between the ED and the substrates. This could have an implication on the cooling rates during the consolidation phase. The cooling rates of samples welded using 1500 N welding force and 86.2 μm vibration amplitude were measured following the same approach described in chapter 3 (section 3.2.3) and were found to be equal to 63.6 °C/s. For simplicity and to allow the discussion to be centred exclusively on the nanoindentation measurements, the temperature profile during ultrasonic welding of samples welded under 1500 N and 86.2 μm is presented below (ETC_F2). For comparison, the temperature profile of ED PPS during welding under 1000 N and 86.2 μm is also shown (ETC_F1).

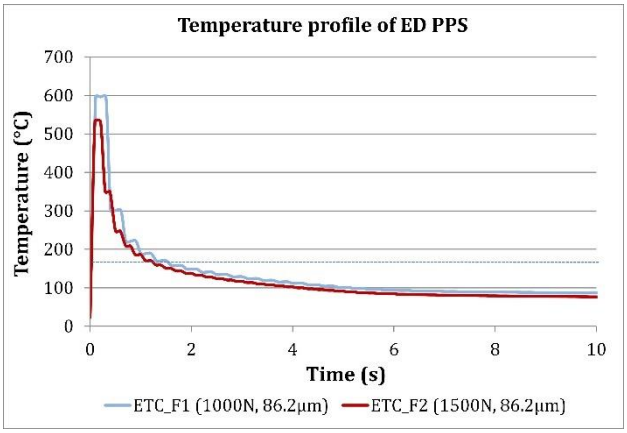

Figure 4.1. Temperature evolution during ultrasonic welding under high welding force (1000 N and 1500 N) and high vibration amplitude (86.2 μm). Only one specimen per series is illustrated for clarity purposes.

The samples were cut from the central region of the overlap areas of the welded joints (Figure 4.2) using a water-cooled diamond saw and were, subsequently, embedded in a two-component methyl-methacrylate based resin (Technovit 4071), supplied by Kulzer Technique. The inner side of the cut area of the overlap was subjected to polishing in order to eliminate surface asperities, minimise the uncertainty in surface determination and decrease the measurement error [4][20]. The polishing was performed using silicon carbide grinding papers up to 1200/P4000 grit size (grain size 5 μm) to obtain a flat and smooth surface. All samples were cleaned with ethanol and rinsed thoroughly with distilled water, after each polishing step, in order to remove any residues on their surface.

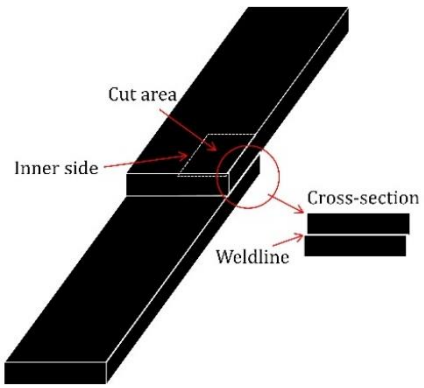

Figure 4.2. Schematic of UW CF/PPS joint. The dashed rectangle highlights the area of the joint overlap which was cut in order to produce the samples for the nanoindentation experiments. The inner side of the cut area of the overlap was subjected to polishing in all samples. Dimensions are not to scale.

Figure 4.3 illustrates the convention used to describe the location of the plies with respect to the weldline. "Inner" plies refers to the plies towards the weldline and "outer" plies refers to the ones away from the weldline.

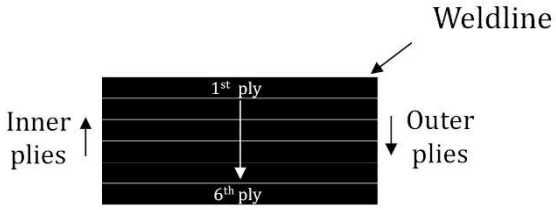

Figure 4.3. Location of the plies with respect to the weldline. The 1st ply is the ply adjacent to the weldline and the 6th ply is the ply farthest away from the weldline.

4.2.3 Nanoindentation

The elastic modulus and hardness of PPS in the weldline and in the resin rich areas of the adherends, were determined through nanoindentation measurements.

4.2.3.1 Nanoindenter

The nanoindentation tests were performed using an Agilent Nano Indenter G200 (Keysight, SantaRosa, CA, USA), equipped with a three-sided Berkovich pyramidal diamond tip. The angle between the three pyramid faces and the centreline was 65.03°. The oscillation displacement amplitude was 2 nm and the amplitude frequency was 45 Hz. The tip was calibrated before the measurements by indenting a standard quartz sample. All measurements were carried out in a vibration-free laboratory, at room temperature (RT) and 40-50% relative humidity (RH).

4.2.3.2 Procedure

This section presents the theoretical background for the calculation of the elastic modulus and the hardness using the nanoindentation technique. While this information is widely available in literature [4][8]-[10][21], it is also presented in this chapter in order to facilitate the reader and to provide a detailed description of the procedure followed.

The elastic modulus of the sample, E, can be calculated by applying the Oliver-Pharr model [8][21]:

$$\boldsymbol{E = \left(1 - v_s^2\right) \cdot \left[\frac{1}{E_r} - \frac{1-v_i^2}{E_i}\right]^{-1}} \qquad \textbf{(4.1)}$$

where E_i and v_i are the elastic modulus and the Poisson's ratio of the indenter (tip) respectively, v_s is the Poisson's ratio of the sample and E_r is the reduced elastic modulus. The latter can be considered as the "combined modulus" of the system, representing the elastic deformation occurring in both the sample and the indenter [9][22] . For the calculation, Poisson's ratio of the neat PPS was taken as 0.36. E_r, can be obtained from the following equation:

$$\boldsymbol{E_r = \frac{S}{2\xi} \cdot \sqrt{\frac{\pi}{A_c}}} \qquad \textbf{(4.2)}$$

where S is the contact stiffness, ξ is a constant which is equal to 1.034 for a Berkovich tip [4] and A_c is the projected area of the indenter tip based on indentation displacement. The details for the calculation of the projected area can be found in literature [4][10].

The hardness, H, of the material is expressed as:

$$H = \frac{F_i}{A_c} \tag{4.3}$$

where F_i is the indentation force.

The deformation pattern during indentation and after load removal is sketched in Figure 4.4, where the initial surface, the surface under load and the surface after load removal are shown: h_s is the plastic deformation after load removal, h_c is the contact depth, and r is the contact radius. During indentation, both elastic and plastic deformation occur and after load removal only the elastic part is recovered, while the plastic deformation leaves a permanent impression on the material's surface.

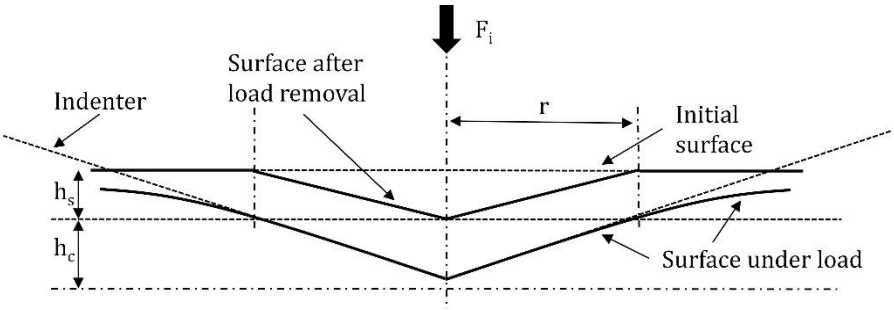

Figure 4.4. Schematic illustration of deformation pattern during indentation and after load removal, adapted from [9] [21].

For the basic mode of nanoindentation, the contact stiffness, S, is determined from the slope of the load-displacement curve at the onset of the unloading stage. A schematic illustration of a typical load-displacement curve of a nanoindentation measurement is shown in Figure 4.5. The classical indentation theory states that the initial unloading portion of the load-displacement curve represents an elastic response, therefore, the slope of the upper portion of the unloading curve is defined as the contact stiffness. However, the unloading part of the load-displacement curve exhibits a more convex curvature, a characteristic of viscoelastic materials as compared to elastic materials. This could lead to errors in the calculation of the apparent contact stiffness. The contact area between indenter and sample continuously changes during unloading causing nonlinear unloading curves [8].

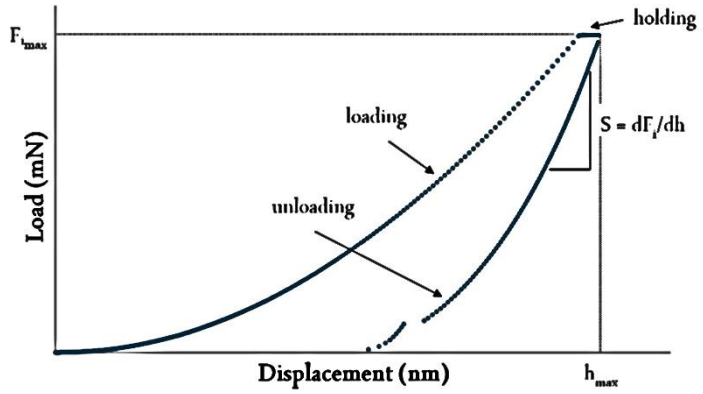

Figure 4.5. Schematic illustration of a typical load-displacement curve, adapted from [10].

In order to mitigate the uncertainties in the slope measurements caused by the non-linearity of the unloading curves, the continuous stiffness measurement (CSM) testing mode was used in this study [4]. The CSM method relies on the application of a small oscillating force on top

of the static force during loading (Figure 4.6) and allows for the continuous measurement of elastic modulus and hardness throughout the loading stage. The superimposed oscillatory force, F_{os}, and the corresponding displacement, h_{os}, are given by:

$$\boldsymbol{F_{os} = F_o \cdot e^{i\omega_o t}} \quad \textbf{(4.4)}$$

$$\boldsymbol{h_{os} = h_o \cdot e^{i\omega_o t - \varphi}} \quad \textbf{(4.5)}$$

where F_o is the oscillatory force amplitude, h_o is the oscillatory displacement amplitude, ω_o is the oscillation frequency, φ is the phase angle between force and displacement responses, and t is the time. The contact stiffness, S, is given by:

$$\boldsymbol{S = \left[\frac{1}{\frac{F_o}{h_{os}}cos(\varphi) - (K_s - m_i\omega^2)} - \frac{1}{K_f}\right]^{-1}} \quad \textbf{(4.6)}$$

where m_i is the mass of the indenter, K_f represents the indenter frame stiffness and K_s represents the stiffness of the springs that support the indenter. Further details on the dynamic indentation model and the calculation of the contact stiffness can be found in literature [4][9]. The CSM method has many advantages over the basic (classic) mode of nanoindentation such as: (i) capability to provide continuous modulus and hardness measurements at any depth during loading, (ii) no dependency on the unloading curves for the calculation of the contact stiffness and (iii) accurate determination of the initial contact between the indenter and the sample.

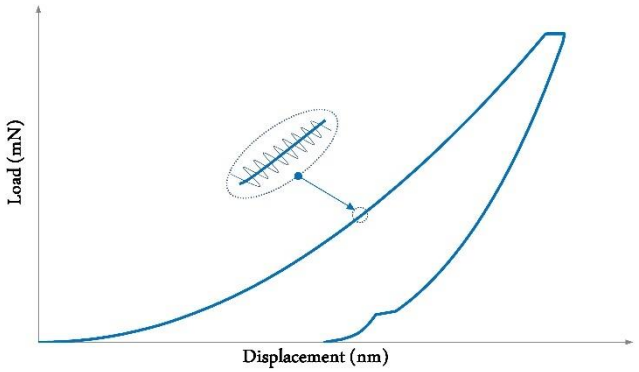

Figure 4.6. Schematic illustration of superimposed oscillating force on the nominally increasing static force.

To account for surface roughness and other surface effects such as sample curvature that are known to influence the measurements [3][10], relatively large displacements were used at which the influence of the surface effects are negligible. The maximum displacement was selected at 5000 nm. In this study, only displacements between 800 nm and 5000 nm were considered in the calculations. It is noted that the indentations in samples F3 and A1 (Table 4.1) reached displacements of 3000 nm instead of 5000 nm due to time constraints during the period of the experiments. The experiments were performed with a constant strain rate of 0.05 s^{-1}. A minimum of 100 μm distance was kept between each indentation in order to prevent interaction between the plastic regions around the indentations.

4.2.3.3 Validation of indentations

Prior to the measurements, the location of each indentation was selected by using the built-in imaging technique of the Agilent Nano Indenter G200. However, the indentations did not

always occur at the selected locations. Abnormally high values of elastic modulus, or increasing modulus with increasing depth were a first indication of possible fibre presence close to the indentations. Therefore, at the end of each indentation test, all indentations for each sample were scrutinised using optical microscopy. The main focus of the microscopy evaluation was to identify the valid indentations and reject the indentations that occurred on fibres or very close to fibres or other defects. Figure 4.7 illustrates one example of valid (acceptable) indentations and one example of an invalid (rejected) indentation (the residual impression of the Berkovich tip can be seen next to the carbon fibres).

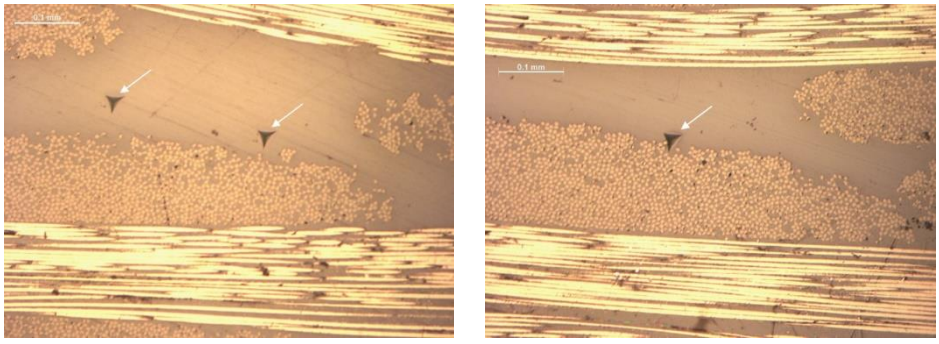

Figure 4.7. Examples of indentations at resin rich areas of an adherend. The left image is an example of two valid indentations while the right image an example of an invalid indentation. Optical microscopy was used to scrutinise every sample in order to ensure that each indentation was performed in a resin rich area.

Table 4.2 presents the number of valid indentations per sample. As it can be seen, the number of indentations was not always equal from sample to sample and from ply to ply because several measurements were rejected following the microscopy evaluation. The valid indentations within the plies of the adherends were normally lower than the ones within the weldline, mainly due to the resin rich area present in the weldline. The size of the resin rich areas within the plies was sometimes a limiting factor because some indentations could not be performed in large enough fibre-free areas (for example, only 4 indentations were valid in the 2nd ply of sample F2).

Table 4.2. Number of valid indentations per sample.

Sample	Valid indentations					
	Weldline	1st Ply	2nd Ply	3rd Ply	4th Ply	5th Ply
F1	*15*	*7*	-	*12*	-	*13*
F2	*20*	-	*4*	*9*	-	-
F3	*19*	-	-	-	-	-
F4	*22*	*6*	*14*	-	-	-
A1	*24*	*17*	*11*	*7*	-	-
S1	*18*	*5*	*10*	-	*15*	-
S2	*11*	*18*	*6*	-	-	-

4.3 Results – Discussion

In this section the results from the nanoindentation measurements are presented and discussed, followed by a brief evaluation of the nanoindentation technique as a characterisation method for thermoplastic composites welded joints.

4.3.1 Weldline

Figure 4.8 and Figure 4.9 show representative curves of E and H, as a function of displacement. As a reminder: F represents the fast processed samples, S the slow processed samples and A the annealed sample (Table 4.1). As it can be seen, the slower welding process resulted in a higher elastic modulus and higher hardness of PPS at the weldline compared to the faster welding process. Annealing also resulted in higher modulus and hardness. Another distinguishable feature in the two figures is the sharp increase of both E and H at very shallow indentations (around 50 nm). This behaviour can be better seen in Figure 4.10 where a "magnified" version of Figure 4.8 is shown (the "magnification" for hardness was omitted since the behaviour is the same).

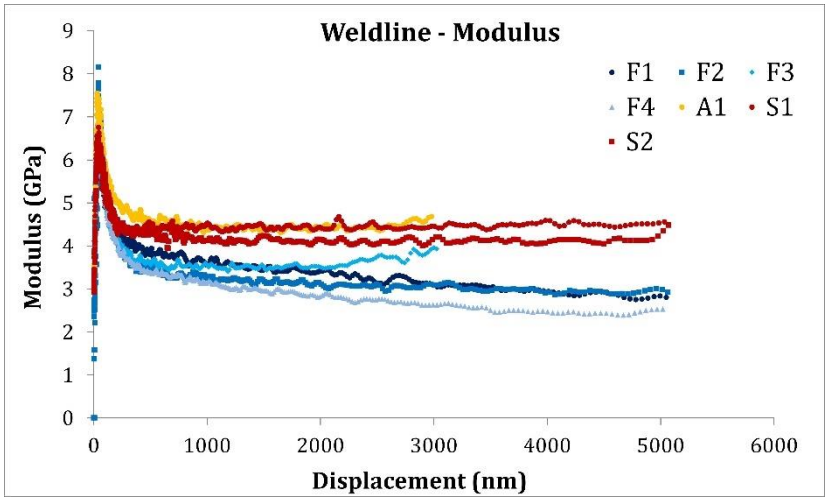

Figure 4.8. Elastic modulus as a function of displacement for all samples at the weldline. Each curve represents one indentation per sample.

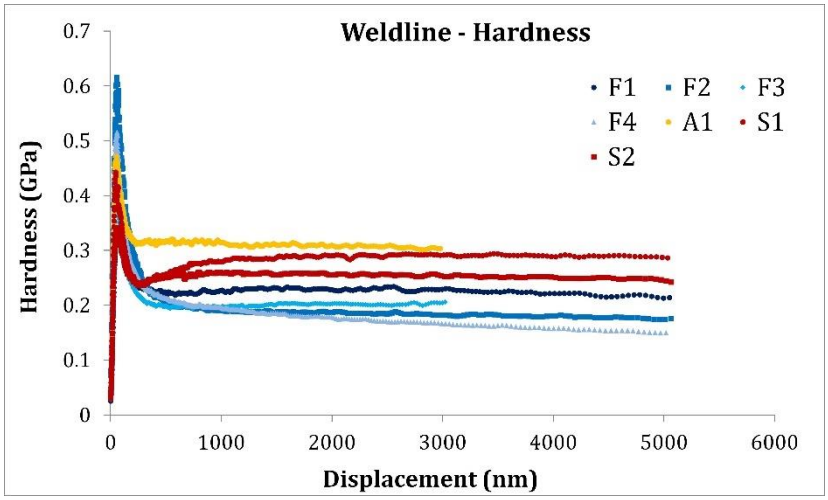

Figure 4.9. Hardness as a function of displacement for all samples at the weldline. Each curve represents one indentation per sample.

At depths larger than 50 nm both E and H started to decrease abruptly until displacements of 100-150 nm, while afterwards they decreased more gradually, becoming virtually constant at penetrations deeper than 500 nm for most of the samples. Surface roughness, surface determination, defects of the tip geometry and indentation size effects (ISE) are known factors that can cause this initial sharp increase [3][5][23]. The shape of the asperities and the distribution of the heights can have a big impact on the measurements by causing large scatter and adding uncertainties to the final result. In addition, the sample preparation, such as grinding and polishing, can cause (local) changes of surface properties.

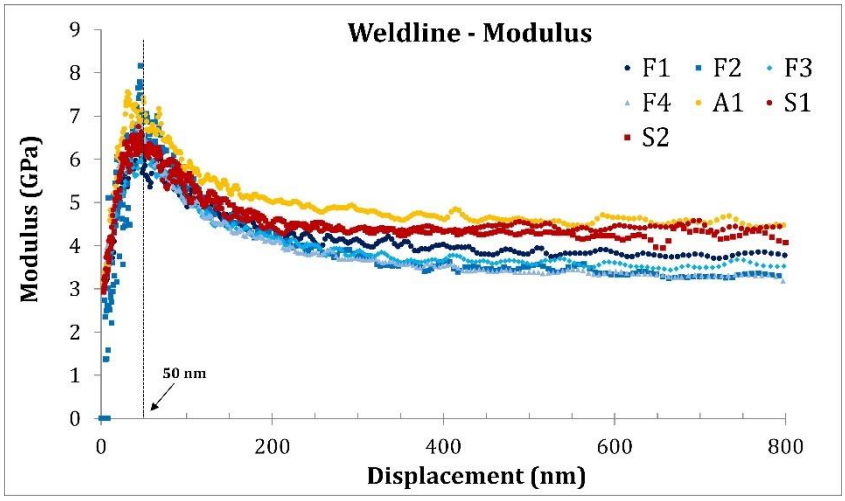

Figure 4.10. "Magnification" of Figure 4.8, showing the sharp increase of elastic modulus at shallow depths.

In some samples, though, both modulus and hardness increased with displacement, even up to 5000 nm (for example, F1, F2, F4 in Figure 4.8). In order to account for the influence of the displacement on the elastic modulus and allow for this influence to be better illustrated in the results, the average values of elastic modulus were calculated every 1000 nm, within a range of ±200 nm, for example, between 800-1200 nm for 1000 nm. Displacements at 1000 nm were considered deep enough to avoid effects such as tip bluntness and surface roughness [4]. Table 4.3 lists the displacement range in which the values were calculated.

The elastic modulus as a function of displacement is illustrated in two figures, Figure 4.11 and Figure 4.12, instead of one, for better clarity. The elastic modulus of F1, F2 and F4 decreased with increasing displacement while for F3 the elastic modulus slightly increased, as shown in Figure 4.11. In the case of A1, S1 and S2 (Figure 4.12), E was virtually constant throughout the entire displacement range.

Table 4.3. Displacement range in which E and H values were calculated.

Displacement Reference	1000nm	2000nm	3000nm	4000nm	5000nm
Measurement Range (nm)	*800-1200*	*1800-2200*	*2800-3200*	*3800-4200*	*4600-5000*

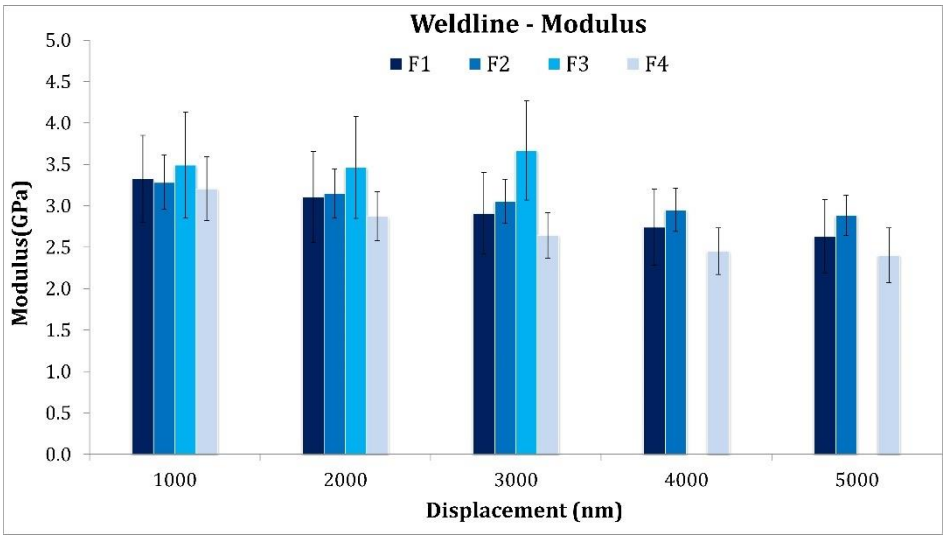

Figure 4.11. Elastic modulus as a function of displacement at the weldline of F1, F2, F3 and F4. The processing conditions in samples F1 and F2 were identical. Samples F3 and F4 were also identical in terms of processing conditions.

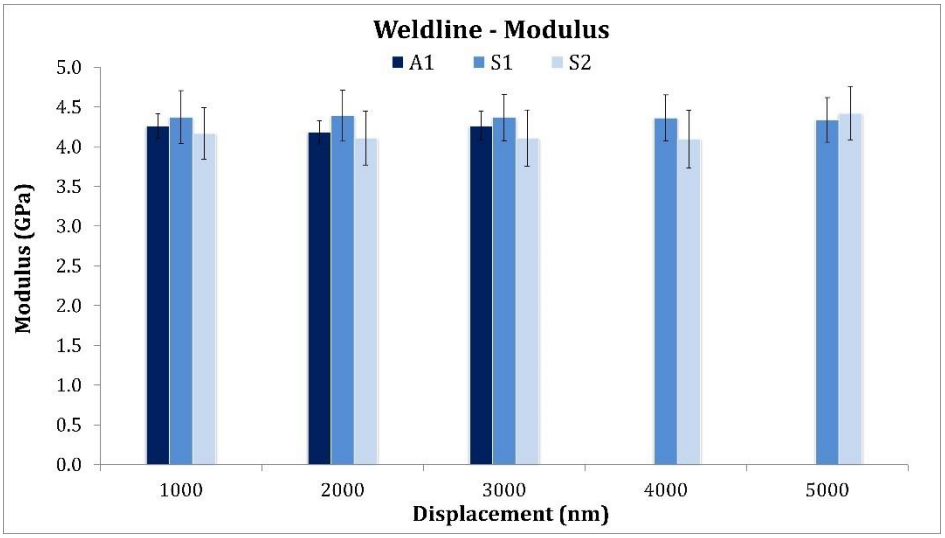

Figure 4.12. Elastic modulus as a function of displacement at the weldline of A1, S1 and S2. The processing conditions in samples S1 and S2 were identical.

The same approach was used for the hardness values (i.e. examination of hardness as a function of displacement), shown in Figure 4.13 and Figure 4.14. The hardness of F1 – F3 samples appeared to be independent of displacement while in F4 the hardness, just as the modulus, was displacement dependent. Similarly to the modulus-displacement relationship, H of S1 and S2 did not change significantly with increasing depth while H of A1 appeared to be slightly more dependent, but still not significantly (less than 10% relative difference).

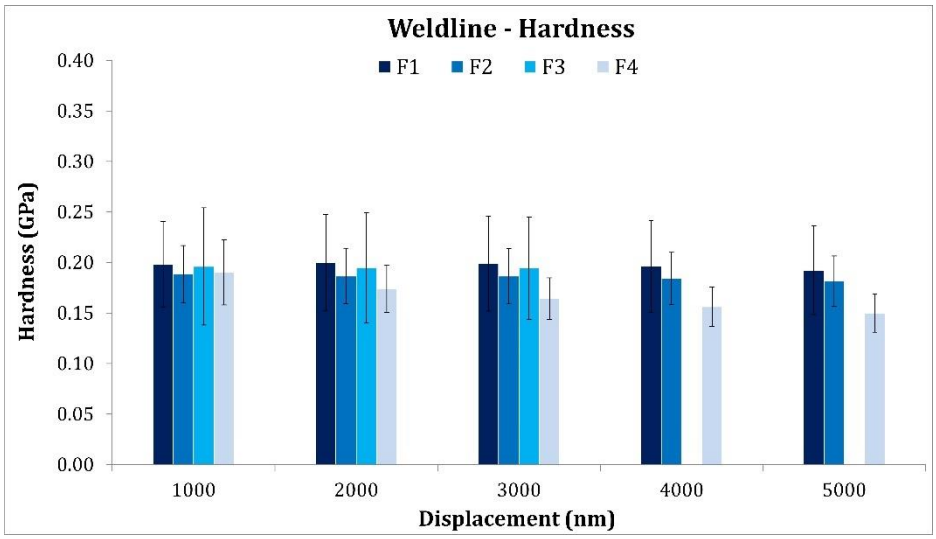

Figure 4.13. Hardness as a function of displacement at the weldline of F1, F2, F3 and F4.

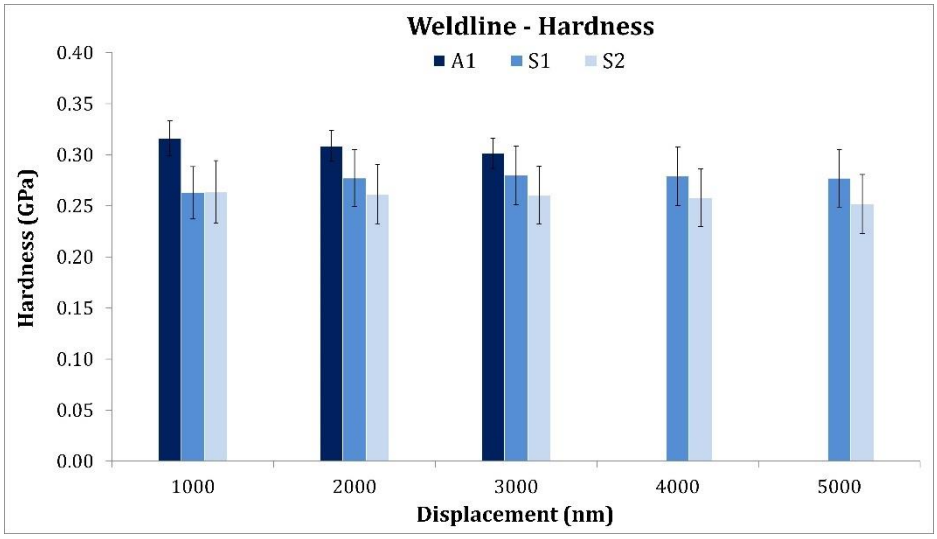

Figure 4.14. Hardness as a function of displacement at the weldline of A1, S1 and S2.

Although the decrease in E and H with increasing displacement was observed in weldlines with predominantly amorphous PPS, there is no strong evidence of a link between crystallinity and E or H – displacement dependency. At first glance, it seems that sample inhomogeneity related to crystallinity might have been the primary reason, considering that the decreasing trend was observed in samples welded under high welding force and high vibration amplitude. However, as shown in Figure 4.11 the modulus of F3 did not decrease with increasing displacement while in Figure 4.13 it was shown that the hardness of F2 and F3 were not displacement dependent. One reasonable explanation of the elastic modulus and hardness dependency on displacement could be based on the polymer deformation during indentation. The polymer will deform plastically while being in contact with the indenter, which can lead to either pile-up or sink-in of the material [22]. The former occurs when the deformed surface has risen higher than the original surface while the latter occurs when the deformed surface is lower than the original surface. Pile-up and sink-in phenomena are related to the ratio between the elastic modulus and yield stress. For high ratios pile-up can occur while for low ratios sink-in can occur [21]. Pile-up can lead to overestimating the elastic modulus while sink-in can lead to underestimation of the elastic modulus [7][24]. Hence, sink-in was considered as a potential reason for the continuous decrease in E. However, the micrographic investigation of the

contact impressions of all samples was inconclusive and could not unambiguously associate the E-h dependency to sink-in. Further investigation in a separate study could shed light upon this phenomenon.

The role of displacement can be quite critical in the comparison: at 1000 nm the ratio between the weldline E of F1 and S1 was 0.76, while at 5000 nm the ratio was 0.61. Therefore, depending on the displacement the differences between the results can vary, leading to different conclusions. Considering that indentations at 5000 nm might be too deep, allowing for effects such as polymer deformation to be aggravated, but also not discarding the influence of displacement simply as a test artefact, the data were re-processed and an analysis of the weldline measurements was conducted by averaging the measurements between 1000 nm and 3000 nm. The latter was selected as the upper limit because as a value it is between 1000 nm and 5000 nm. The same approach was adopted for the adherend measurements which are presented in section 4.3.2. Figure 4.15 summarises the average values of E and H within 1000 nm to 3000 nm for all samples. This comparison provides a more clear picture to the reader regarding the effect of process parameters on PPS elastic modulus and PPS hardness in the weldline.

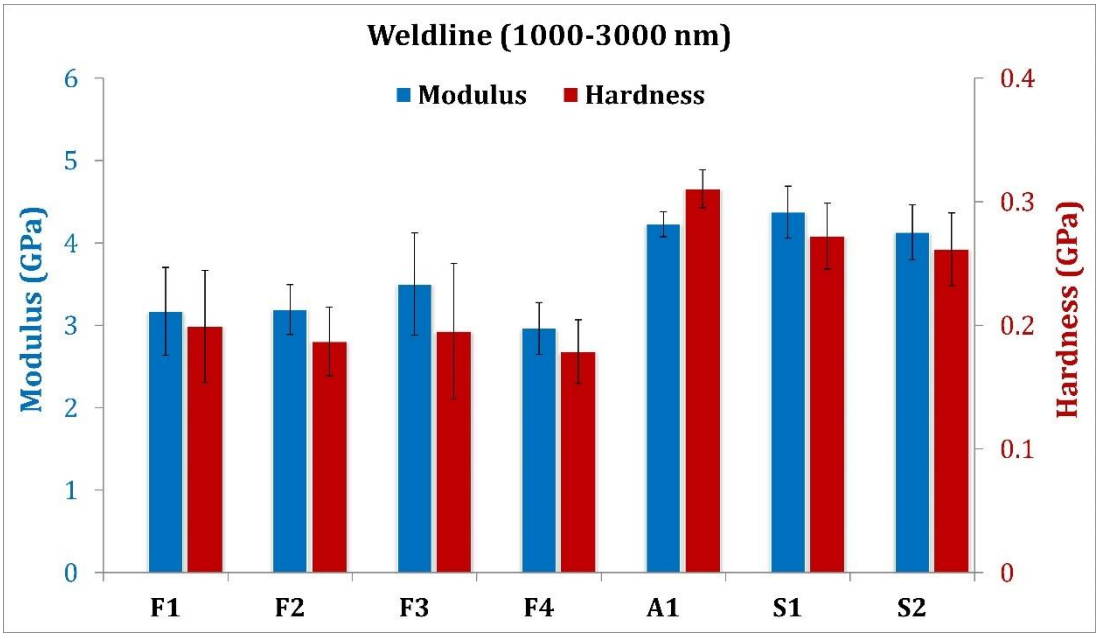

Figure 4.15. Average values of elastic modulus and hardness in the displacement range between 1000 nm and 3000 nm. The measurements were performed in the weldline of the samples.

The key point to be noted from Figure 4.15 is that the elastic modulus and the hardness of A1, S1 and S2 were consistently higher than the ones of F1 – F4 samples, throughout the entire displacement range. Hence, on the basis of the evidence illustrated in Figure 4.15, it seems that the findings of the nanoindentation tests are in good agreement with the results presented in 3. The slow welding process resulted in higher E and H than the faster welding process, suggesting a higher X_C, as also suggested by the DSC and WAXD measurements of the previous chapter. The higher E and H of the annealed sample also confirm the consistency of the nanoindentation measurements, since the annealed sample has a higher X_C than the fast processed samples (note: DSC results on annealed PPS are presented in detail in chapter 5).

An interesting point to be made here is that the elastic modulus of A1 was slightly lower than the elastic modulus of S1, although well within the scatter of the data (only 3% of relative difference), while the hardness of A1 was higher than the hardness of S1 by 14%. Figure 4.16

shows a micrograph taken at the weldline of sample A1, where the presence of a large void can be seen. Normally, the validation of indentations (as described in section 4.2.3.3) led to only accepting indentations such as the ones in Figure 4.16 (far away from voids). However, for areas such as the weldline of sample A1 it was not possible to detect any voids deeper in the surface (therefore, not visible) which might have been very close to the indentation-affected areas. The voids were mainly observed in the annealed sample and appeared to have been formed during the annealing process. It is suggested that E of A1 might have been affected by the presence of voids while it seems that H was not much affected by the voids. The potential causes of void formation in the annealed sample are beyond the scope of this study, nevertheless, a brief discussion speculating on the causes is given in chapter 5 (section 5.4).

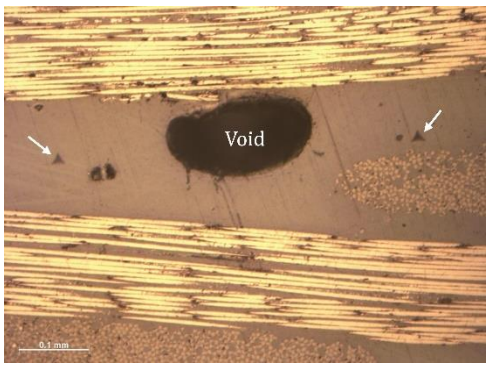

Figure 4.16. Large void in the weldline of sample A1. The arrows indicate the indentations.

An additional point to be made, though, is that at the beginning of stage 4, the polymer was already at its molten state which means that regardless of whether the ultrasonic welding process stopped at early stage 4 or continued beyond that point, the polymer would have cooled down from its melt. Perhaps, the only effect could be on the actual cooling rates encountered at the weldline since the vibration times were shorter. However, as it was previously explained in chapter 3, longer vibration times would only result in lower cooling rates, thus, even if the vibration phase was terminated at a later phase of stage 4, the crystallinity degree, if not the same, would only be higher. In this context, the higher elastic modulus of PPS in S samples compared to F samples is considered as a credible result. With regard to the larger scatter observed in the F1 – F4 samples a plausible explanation could be the sample inhomogeneity. As it was shown in chapter 3, the fast welding process resulted in predominantly (but not fully) amorphous PPS at the weldline. Depending on the average crystallite size and distribution, it could be possible that regions of different crystallinity and/or crystal size were indented, causing larger variations in the measured values.

4.3.2 Adherends

The elastic modulus and hardness of PPS were measured through indentations at the resin rich areas of the adherends. As mentioned in the experimental procedure, all indentations were meticulously examined in order to verify that the penetrations of the indenter took place in resin rich areas. Not all indentations were accepted depending on their location (e.g. very close to a fibre).

Following the approach used for the weldline measurements, Figure 4.17 and Figure 4.18 summarise the average values of elastic modulus and hardness within 1000 nm to 3000 nm for all samples. The results from the weldline measurements (already presented in Figure 4.15) are also included in order to provide the complete overview of the nanoindentation measurements.

The key points deduced from Figure 4.17 and Figure 4.18 are the following:

i. In all F samples, E and H of PPS in the adherends were significantly higher compared to the ones in the weldline.
ii. In S1 and S2, E and H of PPS in the adherends were virtually the same as the ones in the weldline.
iii. In A1, the PPS hardness in the adherends was virtually the same as the ones in the weldline but the PPS elastic modulus in the weldline was 12% lower.
iv. In most samples, E seemed to be fairly constant through the thickness of the adherends (from 1st ply to 5th ply). Only F4 exhibited a slight increase of 9% from 1st ply to 2nd ply.
v. In most samples the relative differences in PPS hardness between adjacent composite plies (1st, 2nd, 3rd ply) were slightly larger (up to 9%) than the ones in PPS elastic modulus. Through 3rd, 4th and 5th plies the hardness remained fairly constant in all samples.
vi. The average values of E and H of A1, S1 and S2 were always higher than the ones of the F samples, regardless the layer of the sample (weldline or composite ply).

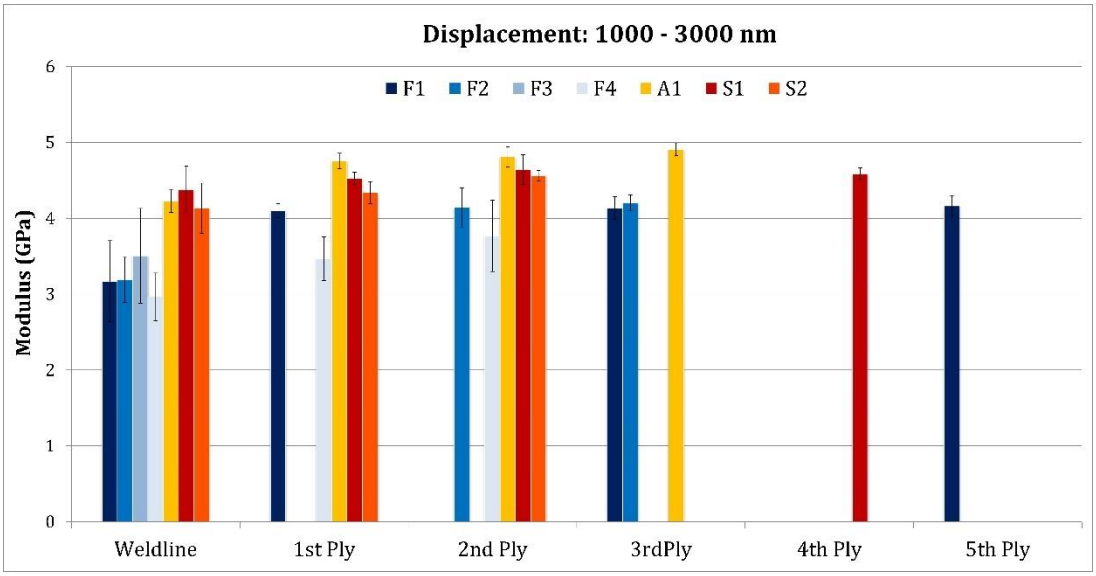

Figure 4.17. Average values of elastic modulus in the displacement range between 1000 nm and 3000 nm. The measurements were performed in the adherends of the samples.

The formation of a welded joint simply implies that the matrix in the 1st ply partially fuses during the vibration phase allowing for intermolecular diffusion to occur between the energy director and the matrix at the surface of the 1st composite ply. In the case of samples F1 – F4, the higher E and H of the 1st ply compared to the weldline suggests that the cooling rates in the former were somewhat slower, leading to higher X_C. The HAZ is an area within the bulk of the laminate that is affected by the welding process and, depending on the process parameters, it can extend to more than one layer of the laminate, so not just the surface of the 1st composite ply. With regard to the fast processed samples, the slightly higher hardness in the 2nd ply compared to the 1st ply could have been a result of a limited – to the 1st ply – HAZ. Possibly, the heat transfer to the 2nd ply and the outer plies was not sufficient to raise the temperature enough in order to melt the polymer crystals. Alternatively, if the melting temperature was reached then the cooling rates in the 2nd ply would be even slower than the ones in the 1st ply, resulting in higher crystallinity. In fact, if the latter occurred then measuring X_C (directly or indirectly) might not be sufficient to determine the extension of the HAZ area. More information on the material structure (e.g. lamellar thickness, average crystallite size) before and after welding would be needed, information that cannot be obtained via

nanoindentation measurements. Nevertheless, the hardness measurements were not always in line with the modulus measurements, as the latter showed a fairly constant value through the thickness of the laminate with the exception of sample F4. In addition, Villegas [1] has indicated that the HAZ of a joint welded using a welding force of 1500 N and a vibration amplitude of 86.2 μm (like in F1 and F2) was very small and restricted to the adjacent plies to the weldline. By removing the solidification phase from the welding process, Villegas showed that deconsolidation voids formed only at a very limited area (1st ply), indicating that no melt of PPS occurred in the next plies. Considering the very short processing times it could be argued that the heat transfer through the thickness of the laminate was insufficient, restricting the HAZ only to the 1st ply and, possibly, to the 2nd ply.

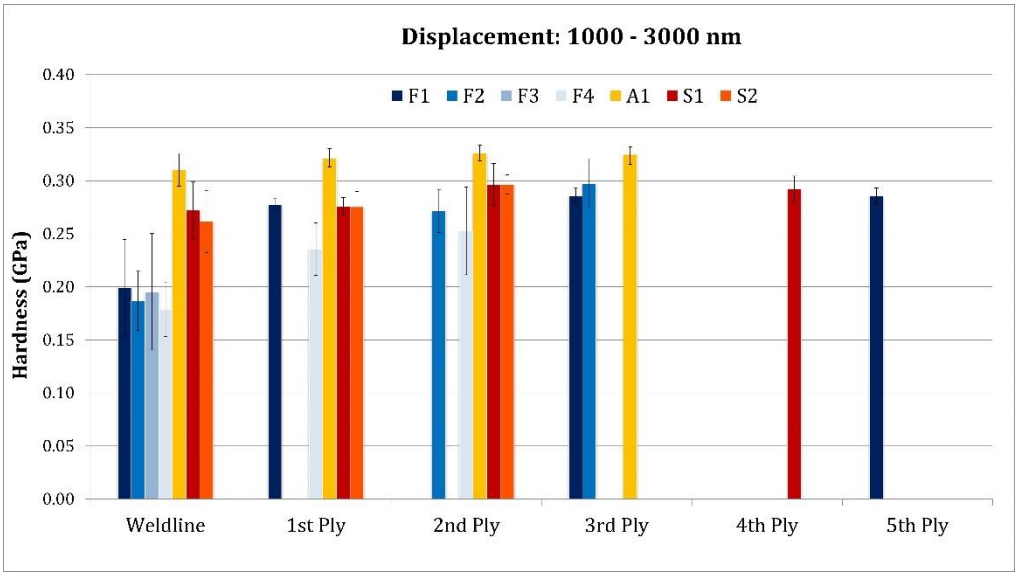

Figure 4.18. Average values of hardness in the displacement range between 1000 nm and 3000 nm. The measurements were performed in the adherends of the samples.

Heat can transfer from the weldline to the adherend due to the high transverse thermal conductivity of the carbon fibres. The longer welding times of the S samples due to the low force (300 N) and low vibration amplitude (51.8 μm) allowed for sufficient time for the heat to be transferred to the outer plies of the laminate and raise its temperature. This can have an impact on the HAZ size. The effect of long processing times was manifested in the work of Ageorges [2]; low power levels in resistance welding of CF/PEEK resulted in long processing times and heat transfer deep in the laminate. Contrarily, high power levels led to shorter processing times, higher temperatures in the plies adjacent to the weldline and lower temperatures in the plies far from the weldline. Similar effects from the processing times appear to occur in these experiments too, where the short welding times in the F samples seem to limit the HAZ mainly in the 1st ply. The data in Figure 4.17 and Figure 4.18 showed that the relative differences in E and H between adjacent plies in the S samples are similar to the equivalent ones in the F samples. This could have served as an indication of a restricted HAZ area to the 1st ply and, possibly, to the 2nd ply of S1 and S2. However, by referring again to the work of Villegas [1], it can be noticed that the slow processed samples might actually have a more extensive HAZ: in the same type of experiments (i.e. absence of solidification phase), the deconsolidation voids were present in several plies (at least in the first 3 plies) of a joint welded under 300 N force and 51.8 μm vibration amplitude (like in S1 and S2). Furthermore, as mentioned in the discussion on the adherends of F samples, similar values of E and/or H do not necessarily mean that there is no HAZ. The cooling rates could have been decreasing throughout the laminate, being slow enough to allow for PPS crystallization to occur and, consequently, to achieve high modulus and hardness. Keeping in mind that the cooling rates

in the weldline already yielded PPS of moderate crystallinity, it is likely that slower cooling rates would lead to higher degree of crystallinity for PPS in the outer plies.

A closer look at the data in Figure 4.17 revealed an unexpected discrepancy: the average modulus values in the 2nd and further plies were higher in S1 and S2 than in the F1 – F4 samples. A similar discrepancy was also observed for the hardness values, in F2 and F4 with respect to S1 and S2. Sample F1, however, showed almost equal hardness to S1 and S2 regardless the layer of the laminate. Considering the limited HAZ extension in the fast processed samples, the logical result would be that in their outer plies E and H were equal or even higher than the ones of the slow processed samples, depending on the extent of the HAZ in S1 and S2 and the cooling rates. If the extent of the HAZ was limited to the 1st and, perhaps, to the 2nd ply of the S samples, then one would expect that the average values in the outer plies (3rd – 6th plies) would be equal in all samples (fast and slow processed). If the extent of the HAZ in S1 and S2 was larger, reaching the 3rd or even the 4th ply, then one would expect that the cooling rates deep in the laminates of S1 and S2 would not cause a higher crystallinity degree than the one caused by the cooling rates occurring during the consolidation of the CF/PPS laminates (prior to welding). During press consolidation, the cooling rates are slow (around 15 °C/min) and favourable for obtaining PPS of optimum crystallinity and, consequently, of high elastic modulus and hardness. Hence, this discrepancy in the measured values cannot be explained in terms of process and/or material properties. The reasons for this discrepancy remain unclear and, while the possibility of a process/material related phenomenon cannot be completely ruled out, it is suggested that it was mainly due to the limitations of nanoindentation as a technique. The results in this study were inconclusive regarding the true extent of the HAZ area. A larger number of measurements in all plies of a laminate prior to welding are required in order to create a true benchmark while additional information on the material structure before and after welding, such as crystal size, could be necessary.

The final objective of this study was to evaluate the potential of nanoindentation as a characterisation technique of thermoplastic composites welded joints. Some uncertainties in the results in the resin rich areas of the adherends, together with the modulus-displacement dependency, raised some concerns about test artefacts and their effect on the measurements. One limitation of the technique is that the presence of fibers in the vicinity of the indentations could artificially enhance the local stiffness. In addition, the typical gradient in the matrix properties observed in fibre reinforced polymers due to the fibre/matrix interface and interphase makes it difficult to determine whether a property has been influenced by the welding process or not. The results also indicated that the hardness measurements were possibly less dependent on displacement and less susceptible to defects like voids compared to the modulus measurements.

Nonetheless, for obtaining reliable measurements in the weldline, nanoindentation appears to be a useful and effective technique. The resin rich weldline and the large distance between the indentations and the fibres of the 1st plies allow for a reliable evaluation of modulus, hardness and, ultimately, crystallinity, "free" of the aforementioned uncertainties. The evidence presented in this study suggest that nanoindentation should be utilised for qualitative and comparative purposes, for instance, to determine relative differences between samples. While nanoindentation can be an effective tool to determine whether a polymer is amorphous or semi-crystalline, it might not be capable of comparing two polymers that have small differences in crystallinity degree.

4.4 Conclusions

The effect of the ultrasonic welding process parameters on the PPS modulus and hardness in the weldline and adherends of CF/PPS welded joints was evaluated by nanoindentation experiments. The main objective of this work was to investigate the influence of the welding process on the elastic modulus and the hardness of PPS in the weldline and in the adherends and compare the findings with the results in 3.

It was demonstrated that low welding force (300 N) and low vibration amplitude (51.8 μm) resulted in higher modulus and hardness at the weldline of CF/PPS welded joints compared to high welding force (1000 N and 1500 N) and high vibration amplitude (86.2 μm). Furthermore, it was shown that annealing of the fast processed welded joints resulted in weldline modulus similar to that of the slow processed welded joints and in higher weldline hardness compared to the latter. These findings confirm the conclusions of chapter 3 that slower welding processes can yield PPS of moderate crystallinity while faster welding processes can yield predominantly amorphous PPS.

In most of the samples, the modulus appeared to be fairly constant through the thickness of the adherends, while the hardness seemed to be increasing more gradually away from the weldline, yet, not significantly. However, it was not possible to determine whether the stable modulus and hardness were a result of a limited HAZ or a result of slow cooling rates inside the adherends that allowed enough time for crystallization to occur. The limitations of the nanoindentation technique and the experimental procedure followed in this study could not provide sufficient and unambiguous evidence of the true extent of the HAZ. Further investigation is required to determine whether the outermost plies of the adherends (i.e. 3rd to 6th ply) were also affected by the welding process.

The findings of this study suggest that the nanoindentation technique should be used with caution when evaluating anisotropic materials, especially fiber reinforced polymers. Factors such as the crystal size distribution, the presence of fibres that can enhance stiffness locally, and the gradient in material properties in areas like the interphase between the fibres and the bulk matrix, can enlarge the uncertainty and scatter in the modulus and hardness measurements. Meticulous sample preparation and data analysis are required to ensure that each measurement is relevant and free of test artefacts or other undesired effects. In thick (rich) resin areas like the weldline, the experimental error is smaller but in areas within the adherends where the indentations can be near the fibres, the data analysis can be challenging, time consuming and inconclusive. Overall, it is recommended to use nanoindentation as a qualitative technique for modulus, hardness and crystallinity evaluation.

Bibliography

[1] Villegas IF. Strength development versus process data in ultrasonic welding of thermoplastic composites with flat energy directors and its application to the definition of optimum processing parameters. Composites: Part A 2014; 65: 27-37.

[2] Ageorges C, Ye L. Fusion Bonding of Polymer Composites. London: Springer, 2002.

[3] Iqbal T, Briscoe BJ, Yasin S, Luckham PF. Nanoindentation response of PEEK surfaces — A semicrystalline bimodal behaviour. J Appl Polym Sci 2013; 130: 4401-4409.

[4] Voyiadjis GZ, Samadi-Dooki A, Malekmotiei L. Nanoindentation of high performance semicrystalline polymers: A case study on PEEK. Polymer Testing 2017; 61: 57-64.

[5] Voyiadjis GZ, Malekmotiei L, Samadi-Dooki A. Indentation size effect in amorphous polymers based on shear transformation mediated plasticity. Polymer 2018; 137: 72-81.

[6] Enrique-Jimenez P, Quiles-Diaz S, Salavagione HJ, Fernandez-Blasquez JP, Monclus MA, Guzman de Villoria R, Gomez-Fatou M, Ania F, Flores A. Nanoindentation mapping of multiscale composites of graphene-reinforced polypropylene and carbon fibres. Composites Science and Technology 2019; 169: 151-157.

[7] Hardiman M, Vaughan TJ, McCarthy CT. The effects of pile-up, viscoelasticity and hydrostatic stress on polymer matrix nanoindentation. Polymer Testing 2016; 52: 157-166.

[8] Oliver WC, Pharr GM. An improved technique for determing hardness and elastic modulus using load and displacement sensing indentation experiments. J. Mater. Res. 1992; 6: 1564-1583.

[9] Li X, Bhushan B. A review of nanoindentation continuous stiffness measurement technique and its applications. Mater. Char. 2002; 48(1): 11-36.

[10] Klapperich C, Komvopoulos K. Nanomechanical properties of polymers determined from nanoindentation experiments. Journal of Tribology 2001; 123: 624-631.

[11] Das B, Prasad KE, Ramamurty U, Rao CNR. Nano-indentation studies on polymer matrix composites reinforced by few-layer graphene. Nanotechnology 2009; 20 (12): 125705.

[12] VanLandingham MR, Villarrubia JS, Guthrie WF, Meyers GF. Nanoindentation of polymers: An overview. Macromol. Symp. 2001; 167: 15-43.

[13] Diez-Pascual AM, Gomez-Fatou MA, Ania F, Flores A. Nanoindentation in polymer nanocomposites. Progress in Materials Science 2015; 67: 1-94.

[14] Regis M, Bellare A, Pascolini T, Bracco P. Characterization of thermally annealed PEEK and CFR-PEEK composites: Structure-properties relationships. Polymer Degradation and Stability 2017; 136: 121-130.

[15] McKeen LW. Fatigue and Tribological Properties of Plastics and Elastomers. Elsevier, 2nd edition, 2010.

[16] Menyhárd A, Suba P et al. Direct correlation between modulus and the crystalline structure in isotactic polypropylene. Express Polymer Letters 2015; 9(3): 308-320.

[17] Talbott MF, Springer GS, Berglund LA. The effects of crystallinity on the mechanical properties of PEEK polymer and graphite fiber reinforced PEEK. J Comp Mater 1987; 21: 1056-1081.

[18] Spruiell JE, Janke CJ. A review on the measurement and development of crystallinity and its relation to properties in neat poly(phenylene sulfide) and its fiber reinforced composites. Technical Report, Oak Ridge National Laboratory, 2004.

[19] Villegas IF. In situ monitoring of ultrasonic welding of thermoplastic composites through power and displacement data. J Thermoplast Compos Mater 2015; 28: 66-85.

[20] Shen L, Liu T, Lv P. Polishing effect on nanoindentation behavior of nylon 66 and its nanocomposites. Polymer Testing 2005; 24: 746-749.

[21] Oliver WC, Pharr GM. Measurement of hardness and elastic modulus by instrumented indentation: Advances in understanding and refinements to methodology. J. Mater. Res. 2004; 19(1): 3-20.
[22] Fischer-Cripps AC., Nanoindentation. New York: Springer, 2002.
[23] Alisafaei F, Han CS. Indentation Depth Dependent Mechanical Behavior in Polymers. Advances in Condensed Matter Physics 2015; Article ID 391579.
[24] Briscoe BJ, Savio Sebastian K. The elastoplastic response of poly(methyl methacrylate) to indentation. Proc. R. Soc. Lond. A 1996; 452: 439-457.

5 Thermal effects on the strength of UW CF/PPS joints and their correlation to the crystallinity degree

Science is a way of thinking much more
than it is a body of knowledge.

(Carl Sagan)

In this work, both of the research questions of this thesis are addressed. First, the overall effects of temperature on the mechanical performance and failure mechanisms of UW CF/PPS joints are analysed, followed by the correlation of the performance to the degree of crystallinity of PPS at the weldline. Single lap shear tests were carried out at temperatures ranging from -50 °C to 120 °C to determine the overall trend of the lap shear strength with respect to temperature. The assessment was carried out on three series: two as-welded series, one with an amorphous and one with a semi-crystalline weldline, and one annealed series which had the weldline with the highest possible crystallinity degree, between the three series. The failure mechanisms were identified through fractographic inspection. Thermal analysis was performed in order to gain better understanding of the effect of PPS crystallinity on the lap shear strength.

5.1 Introduction

To date, the effect of temperature on the mechanical performance of TPCs welded joints has not been studied extensively. The work presented in chapter 2 showed that the strength of RW GF/PPS joints was governed by the strength of fibre/matrix interface at all temperatures. Rohart et al [1] found that RW CF/PPS joints exposed to a wide range of temperatures above RT primarily failed at the interface between the heating element and the matrix. In both studies, the largest reduction in lap shear strength occurred at temperatures higher than the glass transition temperature of PPS. To the author's knowledge, no studies on the effect of temperature on UW TPCs have been published. Thus far, much research has been published focusing on the fundamental phenomena of the process [2]-[5] and on the optimisation of the process [6]-[10]. Fracture of UW TPCs joints at room temperature conditions primarily occurs within the composite substrates as broken fibres bundles can be seen on the fracture surfaces [6][7]. It is well known that increasing temperature can cause strength and modulus reductions in polymers [11][12], having also a detrimental effect on the fibre/matrix interfacial strength [13]-[16]. Considering the effect of temperature on the elastic modulus of the matrix and the fibre/matrix interfacial strength, as well as the effect of temperature on RW TPCs joints, it seems plausible to expect that temperature could have a detrimental effect on UW TPCs joints as well.

In the previous chapters, the physical state of PPS at the weldline of UW CF/PPS joints was examined, where a profound effect of the process parameters on the matrix crystallinity was observed. The changes in crystallinity can have a significant effect on properties such as elastic modulus, fibre/matrix interfacial strength and fracture toughness. Gao and Kim showed that increasing cooling rates had a negative effect on the interfacial shear strength of CF/PEEK composites [17][18]. Likewise, annealing of CF/PPS led to enhanced fibre/matrix interfacial shear strength [19][20]. On the contrary, a lower crystallinity degree was found to result in higher Mode-I interlaminar fracture toughness for CF/PEEK and CF/PPS laminates, as reported by several researchers [17][21][22].

Considering the wide range of operating temperatures of aircraft, the effect of temperature and crystallinity on fibre reinforced polymers, and the effect of the ultrasonic welding process on the crystallinity degree of the matrix at the weldline, it is important to investigate the influence of temperature on the strength and failure mechanisms of UW TPCs joints. This chapter discusses the effect of temperature on the lap shear strength and the failure mechanisms of UW CF/PPS joints by linking the weld performance to the degree of crystallinity of PPS at the weldline. A thorough experimental research plan consisting of three series of UW CF/PPS single lap joints, of varying crystallinity degrees at the weldline, was carried out at a wide range of temperatures by measuring the lap shear strength of the joints, accompanied by micrographic analysis of the fracture surfaces.

5.2 Experimental procedure

5.2.1 Materials & laminate manufacturing

The materials used in this study together with the manufacturing method to produce the laminates were described in detail in chapter 3, section 3.2.1.

5.2.2 Ultrasonic welding

The ultrasonic welding process was described in detail in chapter 3, section 3.2.2, and the same procedure was followed in this chapter.

As mentioned in the chapter introduction, three series of single lap joints of varying crystallinity degrees at the weldline were prepared under different conditions. First, the two as-welded series are introduced: one series was prepared using a set of high welding force and high vibration amplitude, (1000 N, 86.2 µm), representing the fast welding process, and one using a set of low welding force and low vibration amplitude, (300 N, 51.8 µm), representing the slow welding process. According to the results shown in chapters 3 and 4, the former yields predominantly amorphous PPS at the weldline (2.4%) and lower modulus compared to the latter, which yields a weldline of moderate PPS crystallinity (14.6%) and higher modulus. A third series was prepared by annealing the welded joints obtained with the fast welding process, for 2 hours at 200 °C inside an oven. It should be noted that the specimens were "free-standing" in the oven (no applied pressure) during the annealing process. The welding and annealing conditions for the three series of joints used in this study are summarised in Table 5.1. Regarding the nomenclature of the specimen series, ASW stands for as-welded, ANN stands for annealed, F stands for fast welding process and S stands for slow welding process.

Table 5.1. Preparation conditions of single lap joints.

Specimen Series	Welding Force (N)	Vibration Amplitude (µm)	Optimum Travel (mm)	Thermal Treatment (post welding)
ASW_F	*1000*	*86.2*	*0.15*	-
ASW_S	*300*	*51.8*	*0.13*	-
ANN_F	*1000*	*86.2*	*0.15*	*2 hours, 200°C*

5.2.3 Characterisation of welded joints

5.2.3.1 Single Lap Shear Tests

Single lap shear tests based on the ASTM D1002 standard [23] were performed at different temperatures within the -50 °C to 120 °C range. A 250 kN Zwick/Roell universal testing machine operating at 1.3 mm/min cross-head speed and a temperature chamber were used for the tests. Prior to each test, the temperature chamber was pre-heated for 1 hour at the test temperature. All specimens were maintained at each test temperature for 10 minutes prior to the tests in order for the entire specimen to reach thermal equilibrium. The tests at -50 °C were performed using liquid nitrogen to reach cryogenic temperatures. The apparent lap shear strength of the welded joints was calculated as the maximum load divided by the average overlap area (25.4 mm x 12.7 mm). A minimum of 5 specimens were tested per joint type and testing temperature. The total number of specimens tested at each temperature are summarised in Table 5.2.

Table 5.2. Number of single lap joint specimens tested at each temperature.

Specimen Series	# of specimens per temperature					
	-50 °C	**20 °C**	**50 °C**	**70 °C**	**90 °C**	**120 °C**
ASW_F	*5*	*5*	*5*	*6*	*14*	*10*
ASW_S	*7*	*6*	*6*	*6*	*7*	*6*
ANN_F	*9*	*5*	*8*	*10*	*10*	*8*

5.2.3.2 Fractography

Fractographic analysis was conducted through a stereo microscope (Zeiss stereo Discovery V8) and a SEM from JEOL (JSM-7500F) in order to investigate the failure mechanisms of the welded joints. The macroscopic images of the fracture surfaces were captured using the stereo microscope while the detailed images at high magnification were captured using the SEM. Prior to the SEM analysis, the fracture surfaces were sputter coated with a thin layer of gold to prevent charging. For the sake of brevity, only specimens tested at -50 °C and 120 °C are shown in this chapter. The two temperatures represent two extreme cases, which could capture and clearly demonstrate the temperature effects (i.e. difference of 170 °C between the two temperatures, while 120 °C is higher than the glass transition temperature of PPS (as shown in chapter 2). In addition, only one mating fracture surface per specimen is shown, again for conciseness purposes, since no differences between mating fracture surfaces were observed in this study. The stereo-microscope images illustrate the full length of the overlap (12.7 mm) while the width of the overlap area is not completely shown (about 5% not shown) due to limitations in the size of the captured image.

5.2.4 Thermal analysis

Differential Scanning Calorimetry was used in order to determine the degree of crystallinity of PPS specimens prepared under different conditions. All DSC measurements were carried out following the procedure described in section 3.2.4.2 (chapter 3). The degree of crystallinity, X_C, was calculated using equation (3.3).

Table 5.3 presents the DSC series investigated in this study. The first three series of Table 5.3 were tested and presented in chapter 3, while the other three series were prepared and tested during this study. A brief description of the preparation of each series follows: (i) ED_Ref, taken from an energy director in its initial state (prior to welding), used as a reference material. (ii) ED_F, being an ED film removed from the weldline under 1000 N and 86.2 μm, representing the weldline of ASW_F. (iii) ED_S, being an ED film removed from the weldline after welding under 300 N and 51.8 μm, representing the weldline of ASW_S. (iv) ANN_Ref, consisting of one PPS film annealed from its amorphous (initial) state inside an oven for 2 hours at 200 °C, representing the weldline of ANN_F. (v) CON_F, being an ED_F sample annealed inside an oven for 10 minutes at 120 °C. (vi) CON_S, being an ED_S sample annealed inside an oven for 10 minutes at 120 °C. Both CON_F and CON_S were prepared in order to examine the influence of conditioning – prior to the SLS tests – for 10 minutes at 120 °C on the crystallinity degree of PPS since 120 °C is higher than the Tg of PPS. The abbreviation CON stands for "conditioned". It must be noted that due to the lack of ASW_F samples at the time of the DSC tests, the annealing effect was studied on fully amorphous PPS films (same PPS films used to produce the ED). Considering the very low crystallinity of ASW_F (2.4% as reported in chapter 3), it was expected that annealing at 200 °C for 2 hours should yield similar levels of crystallinity. Nonetheless, the main objective of this study was to compare specimens of crystallinity levels that differ significantly and not by just below 5%. The ED films were easily removed from the weldline due to the presence of Kapton films between each adherend and the ED: prior to ultrasonic welding, two 25 μm thick Kapton films were fixed with an adhesive tape to each adherend and the ED was sandwiched between them. The method to remove the ED films after welding has been described in detail in chapter 3.

Table 5.3. DSC specimens.

Series ID	Welding Force (N)	Vibration Amplitude (μm)	Thermal Treatment
ED_Ref[1]	*n/a*	*n/a*	-
ED_F[1]	*1000*	*86.2*	-
ED_S[1]	*300*	*51.8*	-
ANN_Ref	*n/a*	*n/a*	*2 hrs, 200 °C*
CON_F	*1000*	*86.2*	*10 min, 120 °C*
CON_S	*300*	*51.8*	*10 min, 120 °C*

[1] *Specimens measured and presented in chapter 3.*

Dynamic Mechanical Analysis was carried out using a Pyris Diamond DMA from Perkin Elmer in order to determine the glass transition temperature and the evolution of the storage and loss moduli of neat PPS films and CF/PPS composites with temperature. One amorphous PPS film and one annealed PPS film, were tested in tension while the composite coupon was tested in three-point bending (3PB). All tests were performed within the temperature range of -50 °C to 200 °C, at a frequency of 1 Hz and a heating rate of 2 °C/min. The dimensions of the neat PPS films were 20 mm x 10 mm x 0.08 mm and of the CF/PPS composites were 40 mm x 8 mm x 1.9 mm. The CF/PPS composite coupon was cut from the same CF/PPS laminates used for the production of the welding adherends, using a water-cooled diamond blade.

Thermomechanical Analysis was performed to measure the coefficient of thermal expansion of neat PPS films, since the thermal expansion of PPS could change with crystallinity and influence the weld performance at elevated temperatures. The TMA specimens were cut in 15 mm x 3 mm x 0.08 mm films and the experiments were performed at a heating rate of 2 °C/min in a Diamond TMA from Perkin Elmer. Like in the DMA tests, the films tested were amorphous PPS, within the -50°C to 150°C temperature range, and annealed PPS (2 hours at 200 °C), within the 20 °C to 150 °C temperature range. Liquid nitrogen was used in both DMA and TMA tests in order to reach the cryogenic temperatures, however, at the moment of performing the TMA tests on annealed PPS it was not possible to reach cryogenic temperatures due to technical issues.

It must be noted that it was not possible to test the removed ED films on TMA and DMA since the films were physically distorted from the welding process (i.e. showing creases and being slightly buckled), which could have had an effect on the accuracy of the DMA and TMA measurements. Therefore, it was decided to proceed with testing only amorphous and annealed PPS films, as the two extreme cases of crystallinity degree. The behaviour of ASW_F was considered to be closer to the one of amorphous PPS, due to the low crystallinity degree of the former, and the behaviour of ASW_S somewhere in between amorphous PPS and annealed PPS due to its moderate value of crystallinity degree.

5.3 Results

5.3.1 Thermal analysis

Figure 5.1 illustrates the degree of crystallinity as obtained from the DSC measurements on the PPS films listed in Table 5.3. It can be seen that ANN_Ref had a similar crystallinity degree (23.4%) to ED_Ref (26%) while ED_S showed a moderate crystallinity degree (14.6%) and ED_F was predominantly amorphous exhibiting a degree of crystallinity of 2.4%. Annealing for 10 minutes at 120 °C brought about a significant increase in the crystallinity of the removed ED films, as demonstrated by CON_F and CON_S, which both exhibited a crystallinity degree of

21.3%. In addition, annealing for 10 minutes at 120 °C also resulted in lower scatter. As presented in chapter 3, the scatter in the crystallinity degree of the removed ED films was relatively high, a phenomenon which was attributed to the non-homogeneity of PPS crystallization during welding.

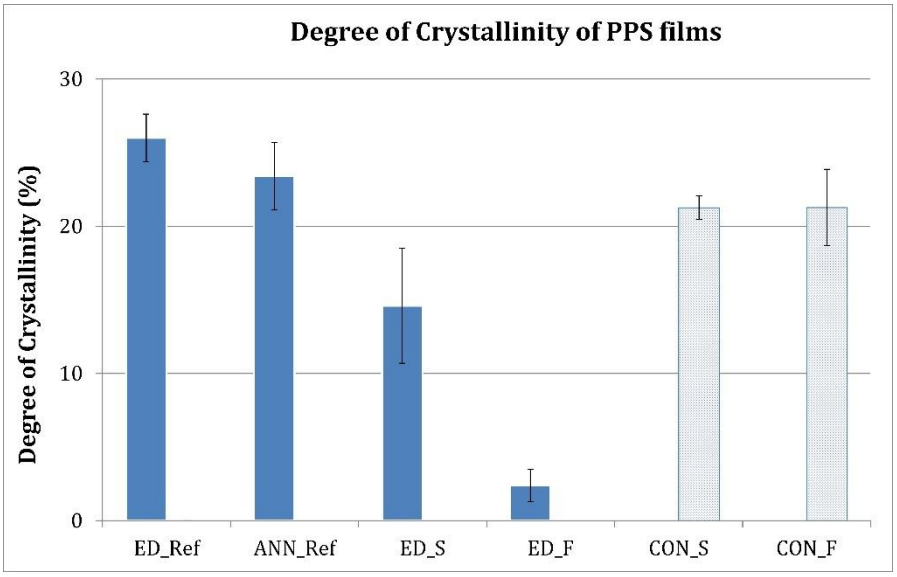

Figure 5.1. Crystallinity degree of PPS films calculated from DSC measurements.

The DMA measurements on amorphous and annealed PPS are shown in Figure 5.2, where the storage modulus (E′) and loss modulus (E′′) curves of both specimens are presented. Obtained from the E′′ peak, the Tg of ANN_Ref was found to be higher than the Tg of amorphous PPS, 108 °C and 91 °C, respectively. The difference in the glass transition temperature is also demonstrated in the E′ curves, as the drop in E′ corresponding to the Tg, occurred below 90 °C in amorphous PPS and close to 100 °C in annealed PPS. In addition, the drop in E′ for annealed PPS was more gradual than the one in amorphous PPS which was abrupt. Furthermore, the E′ of amorphous PPS started to increase around 120 °C, an increase that continued until 130 °C, where E′ reached a plateau. On the contrary, the E′ of annealed PPS continuously decreased until it reached a plateau around 130 °C. Such behaviour is related to cold crystallization of PPS around 120 °C, which caused an increase in the modulus. Another feature of Figure 5.2 is the slight increase in E′ of both films, just before the drop in E′ that corresponds to the Tg. This increase is not very unusual as it has been observed before [25][19]. Barnes and Byerly [25] observed similar small humps in the storage modulus curves of an amorphous composite just below the Tg, but were not able to explain the origin of the phenomenon. They considered it as a test artefact, having a negligible effect on their results. A plausible explanation of the phenomenon has been provided by Kevin P. Menard in his book "Dynamic Mechanical Analysis" [26]. Menard attributed the phenomenon to molecular rearrangement causing stress relief at the glass transition temperature. These stresses are frozen in the glassy state but during heating (up to the glass transition temperature) the molecular chains obtain enough mobility due to the increased free volume at the glass transition. Nevertheless, this phenomenon, either being simply a test artefact or molecular rearrangement, did not interfere with the interpretation of the DMA results, having a negligible effect on them. Therefore, the data obtained from the DMA tests were considered reliable.

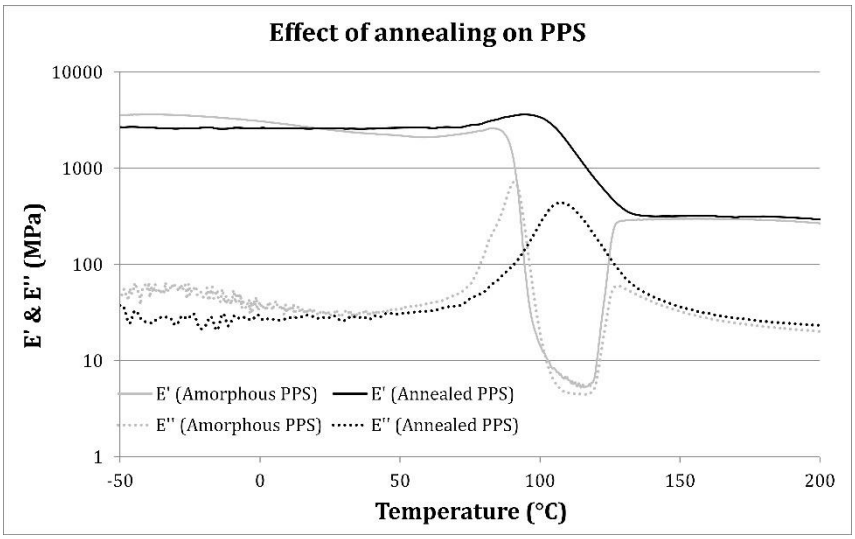

Figure 5.2. Dynamic mechanical analysis of amorphous PPS and annealed PPS (2 hours at 200 °C).

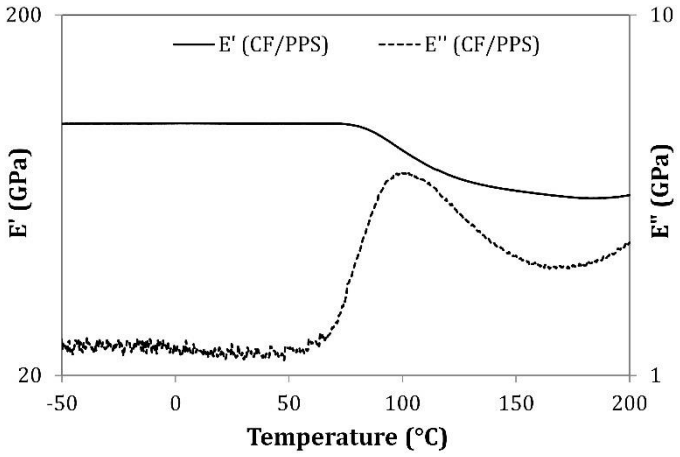

Figure 5.3. E′ and E″ of CF/PPS as a function of temperature.

Figure 5.3 illustrates the thermal evolution of E′ and E′′ of CF/PPS. The Tg was obtained from the E″ peak and was found to be equal to 102 °C, while the drop in E′ started slowly at temperatures around 80 °C. At 90 °C the drop in E′ with respect to 23 °C was only 7% whereas at 120 °C the drop with respect to 23 °C was 24%. Moreover, no secondary transitions were detected by the DMA.

The thermal expansion of amorphous and annealed PPS measured through TMA are illustrated in Figure 5.4. It can be seen that the amorphous PPS expanded significantly above 83 °C, while the annealed PPS exhibited an increase in its expansion rate at a higher temperature (above 92 °C), an increase that was much smaller than the one in amorphous PPS. Two additional points to be noted from this graph are the shrinkage at 110 °C in the amorphous specimen, a behaviour that was not observed in the annealed specimen and could be attributed to cold crystallization, and the significant decrease in thermal expansion rate following the shrinkage.

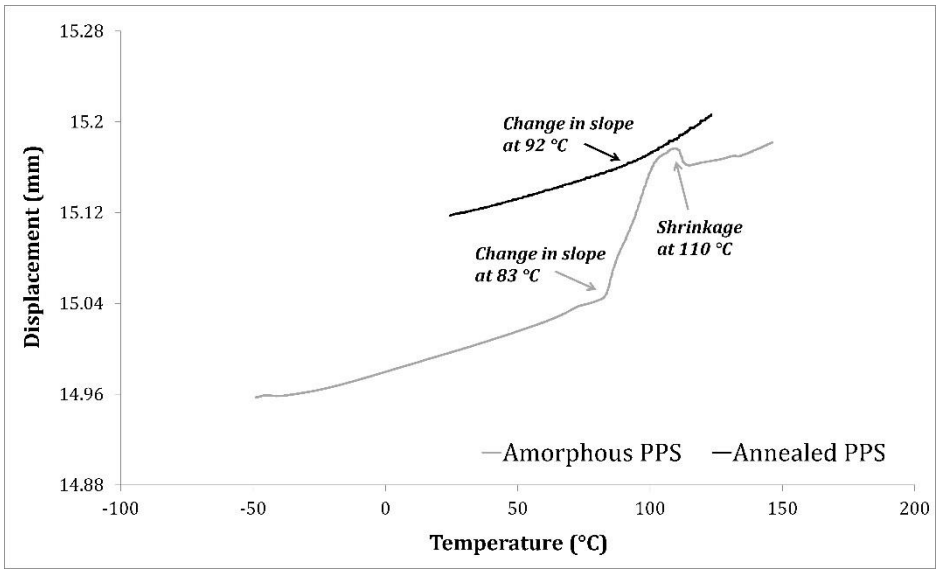

Figure 5.4. Thermal expansion of amorphous PPS and annealed PPS obtained through TMA tests. The glass transition is indicated by the change in slope which is caused by the increase of the expansion rate.

5.3.2 Single lap shear tests

5.3.2.1 Lap shear strength

In the present section, the results of the single lap shear tests are presented, illustrated in three separate graphs (Figure 5.5 - Figure 5.7), and summarised in Table 5.4.

Figure 5.5 illustrates the temperature dependence of the lap shear strength of the ASW_F specimens with 95% confidence intervals. The highest LSS was obtained at -50 °C, it being 28% higher than the LSS at RT. The LSS decreased linearly between RT and 70 °C, however, at 90 °C the reduction in LSS was significant and did not follow the linear trend: it was about 60% of the strength at RT. Further increase in temperature did not lead to a further strength reduction, as the LSS at 120 °C was equal to the LSS at 90 °C. Another notable feature in this figure is the relatively high scatter of LSS at 90 °C, having a CoV of 15%, while the CoV at 120 °C was lower than 10% and at the other testing temperatures lower than 4%. The ASW_S series displayed similar trends to the ASW_F series as demonstrated in Figure 5.6, where the average LSS with 95% confidence intervals is illustrated. As in the ASW_F case, the highest LSS was measured at -50 °C, which was 14% higher than at RT. In addition, the LSS decreased with increasing temperature, exhibiting an almost linear decrease between RT and 70 °C, although having a smaller slope than ASW_F which indicates a more gradual decrease in LSS up to 70 °C. The drop at 90 °C was significant and outside the linear trend: compared to the LSS at room temperature the drop was about 47% which, however, was smaller than the corresponding one in ASW_F (60%). Increasing the temperature to 120 °C, only resulted in a minor decrease in LSS with respect to 90 °C. Moreover, the scatter was below 10% at all testing temperatures, with the highest CoV amounting to 9% measured at -50 °C.

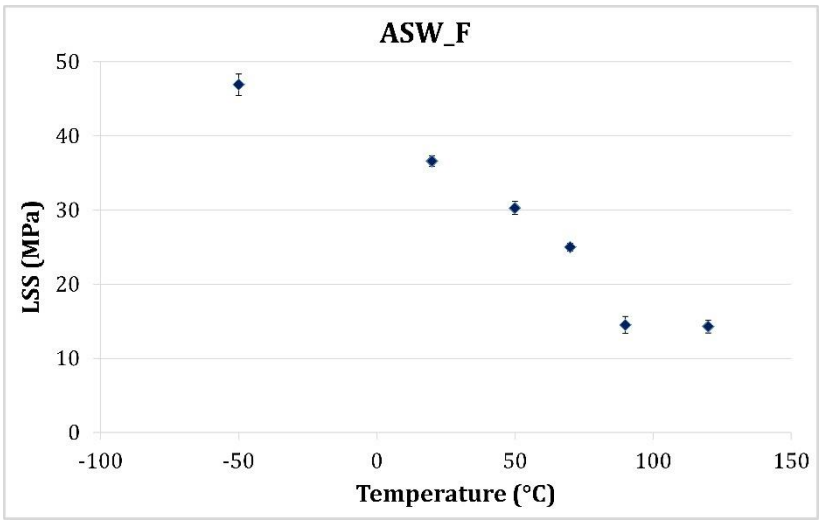

Figure 5.5. Temperature dependence of LSS of ASW_F with 95% confidence intervals.

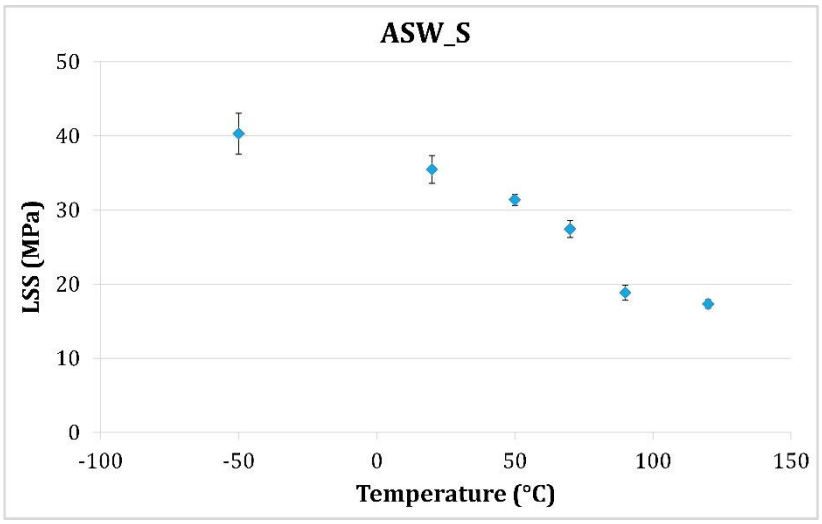

Figure 5.6. Temperature dependence of LSS of ASW_S with 95% confidence intervals.

Figure 5.7 illustrates the LSS of ANN_F as a function of temperature with 95% confidence intervals. It can be seen that the behaviour of the annealed series differs notably from the behaviour of both as-welded series. The LSS of the annealed series between -50 °C and 50 °C remained almost constant, while the reduction at 90 °C with respect to RT (24%) was not as significant as in the other two series (60% and 47% for ASW_F and ASW_S, respectively). Furthermore, increasing the temperature to 120 °C brought about a LSS reduction of 22% with respect to 90 °C, as opposed to the minor or negligible reduction found in the other two series (Figure 5.5 and Figure 5.6). Moreover, the scatter of the annealed series was relatively high at most temperatures (i.e. CoV higher than 10%) except at specimens tested at RT and 120 °C (CoV lower than 7%).

The comparison of the LSS at each temperature among the three series (Table 5.4), shows that at -50 °C and at RT, ASW_F exhibited the highest LSS followed by ASW_S. At 50 °C and above, the ANN_F specimens exhibited the highest LSS among the three series, while the ASW_F exhibited the lowest.

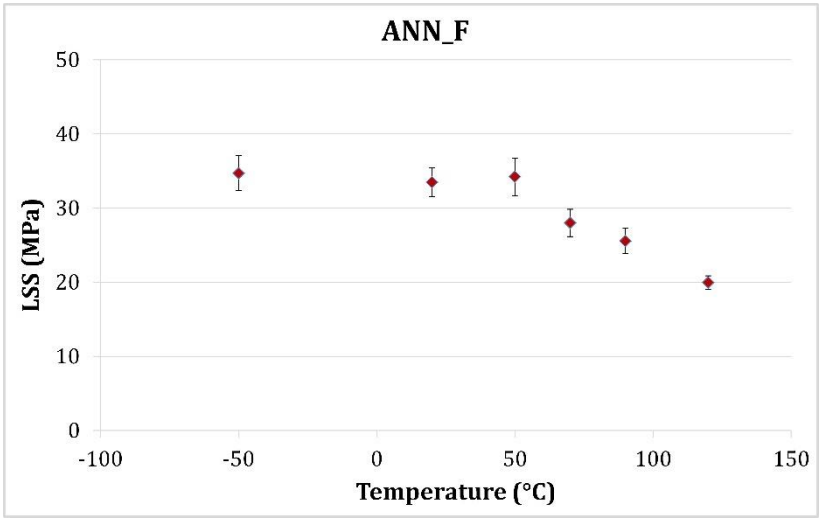

Figure 5.7. Temperature dependence of LSS of ANN_F with 95% confidence intervals.

Table 5.4. Summary of single lap shear tests results on UW CF/PPS joints showing the average LSS together with the standard deviation at each temperature.

Specimen Series	Lap Shear Strength (MPa)					
	-50 °C	**RT**	**50 °C**	**70 °C**	**90 °C**	**120 °C**
ASW_F	46.9 ± 1.6	36.6 ± 0.8	30.3 ± 1.0	25.0 ± 0.7	14.5 ± 2.2	14.3 ± 1.4
ASW_S	40.3 ± 3.8	35.5 ± 2.4	31.4 ± 0.9	27.4 ± 1.4	18.8 ± 1.4	17.3 ± 0.7
ANN_F	34.7 ± 3.6	33.5 ± 2.3	34.2 ± 3.7	28.0 ± 3.0	25.6 ± 2.7	20.0 ± 1.3

5.3.2.2 Fractography

In this part of chapter 5, the results from the fractographic inspection are presented. Representative fracture surfaces at -50 °C and 120 °C are shown for each series which represent the extreme cases of this study.

ASW_F

From the inspection of the fracture surfaces at temperatures equal to or higher than RT, it was observed that the main failure mechanism of the ASW_F specimens was fibre/matrix debonding, which became more prominent with increasing temperature (from RT to 120 °C). Furthermore, the failure locus was always in the 1st ply. At -50 °C, fibre/matrix debonding was less pronounced and many areas with fibres having matrix remnants on their surfaces were observed, suggesting matrix fracture as the main failure mechanism. Regarding failure location, both 1st ply and 2nd ply failure were observed at -50 °C. With respect to the ductile failure of the matrix, it was found to be more pronounced with increasing temperature, especially at 90 °C and 120 °C, where limited brittle failure could be observed.

Figure 5.8 illustrates the fracture surface of an ASW_F specimen, tested at -50 °C. 1st ply failure and 2nd ply failure were observed in all specimens tested at this temperature. The 2nd ply failure appeared to occur in approximately half of the fracture surface and was observed only in the specimens tested at -50 °C. A closer look at the fracture surface in Figure 5.8 with the assistance of a SEM, revealed areas of broken fibres with residual matrix on their surfaces (Figure 5.9A) as well as areas of extensive fibre/matrix debonding (Figure 5.9B), all representing areas with 1st ply failure. However, the fractographic features in Figure 5.9A were more dominant throughout the entire fracture surface than the features in Figure 5.9B.

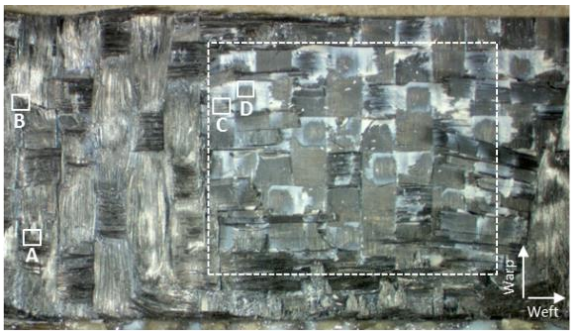

Figure 5.8. Fracture surface of an ASW_F specimen tested at -50°C showing 1st ply failure and 2nd ply failure (the 2nd ply failure is enclosed within the dashed square). A-D represent the locations at which the SEM micrographs were captured.

An additional point to be made is the simultaneous occurrence of both ductile and brittle matrix failure. Examples of ductile failure are illustrated in Figure 5.9B where the matrix has been considerably drawn, resulting in bare fibres surrounded by plastically deformed matrix ("elongated" features), and in Figure 5.9C where deformed matrix was smeared across the fracture surface. Figure 5.9D shows an example of brittle failure of a resin-rich area which was signified by the limited plastic deformation of the matrix. It is interesting to note that brittle failure features were mainly found in areas where failure occurred in the 2nd ply.

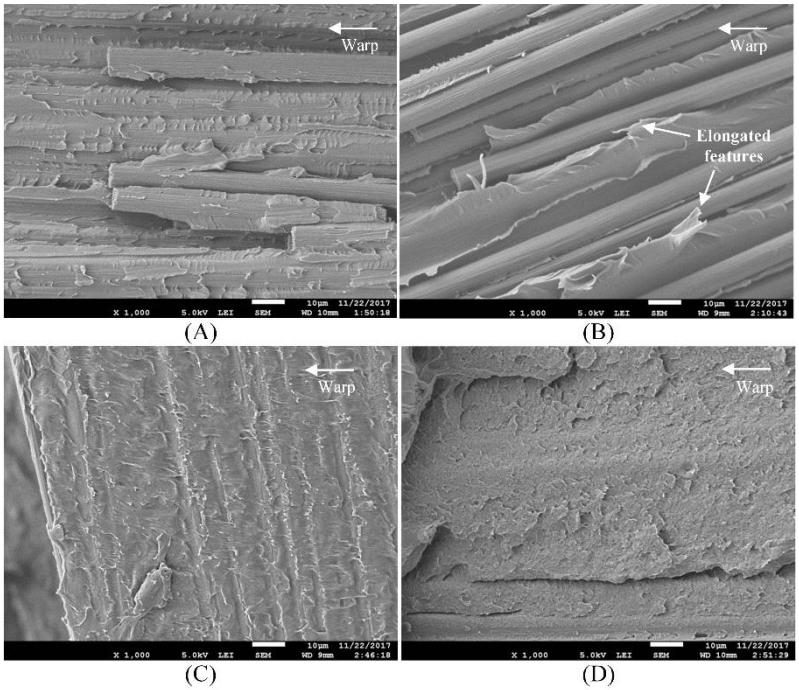

Figure 5.9. SEM micrographs of locations A-D of **Figure 5.8**: (A) Broken and exposed fibres that still have matrix remnants on their surfaces. (B) Fibre distortion and extensive fibre/matrix debonding accompanied by considerable matrix drawing. (C) Smeared matrix indicating ductile failure. (D) Brittle failure as indicated by the limited plastic deformation. The arrow at the top right of each image indicates the warp direction.

A representative fracture surface of ASW_F tested at 120 °C is depicted in Figure 5.10. Failure occurred only in the 1st ply. In addition, the presence of voids in some areas was also observed. It is important to note, that voids were present at the edges of the overlap at all temperatures, however, at 120 °C their presence was extended to other areas of the overlap as well. Regarding the main failure mechanism of the specimens tested at 120 °C, it appears that fibre/matrix debonding was prevalent throughout the entire fracture surface. Figure 5.11A and Figure

5.11B show SEM micrographs taken from two different locations in Figure 5.10, exhibiting extensive fibre/matrix debonding with no residual matrix left on the surfaces of the carbon fibres. The occurrence of fibre/matrix debonding is demonstrated once more in Figure 5.11D where the fibre imprints on the matrix can be seen. In fact, the imprint of the carbon fibres is so clear that even the pattern of the crenulations on the CF surfaces can be observed. Figure 5.11C shows a large amount of voids, accompanied by ductile failure of the matrix. Although "Location C" is at the overlap edges, which are usually exposed to higher temperatures during the welding process causing the occurrence of voids, it is emphasized that voids were present in other areas of the fracture surface as well (Figure 5.10). The ductile failure is better illustrated in Figure 5.11D through extensive matrix drawing. The characteristic features of ductile failure were seen throughout the entire fracture surface, while fractographic features associated to brittle failure, like cusps or limited plastic deformation, were observed in limited areas.

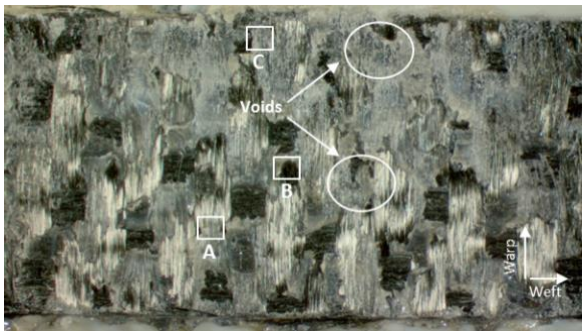

Figure 5.10. Fracture surface of an ASW_F specimen tested at 120°C showing 1st ply failure accompanied by extensive areas of voids (e.g. the two circled areas). A-C represent the locations at which the SEM micrographs were captured.

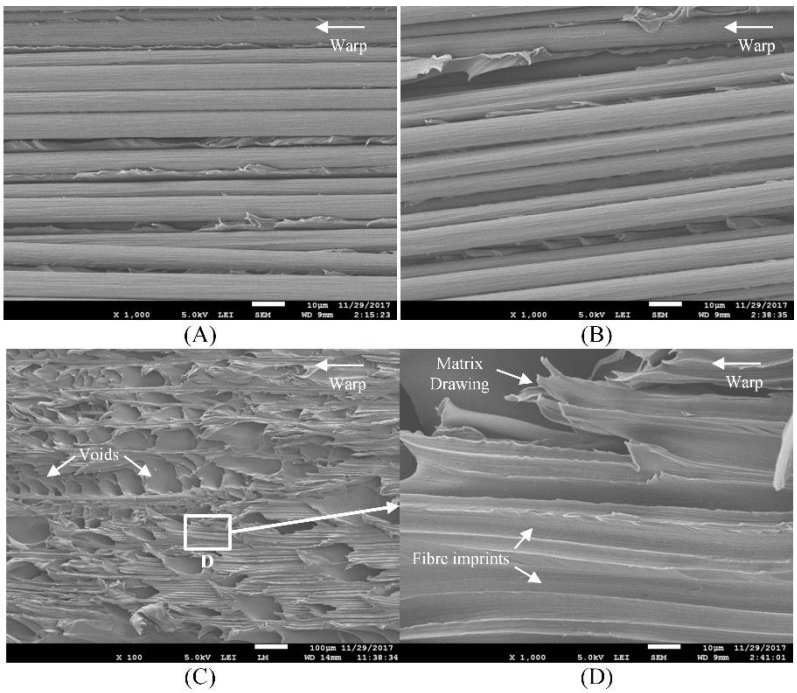

Figure 5.11. SEM micrographs of locations A-C of **Figure 5.10**: (A) & (B) Extensive fibre/matrix debonding accompanied by matrix drawing. (C) Large amount of voids accompanied by ductile failure. (D) Magnification of location D of **Figure 5.11C**, showing substantial matrix drawing and fibre imprints. The arrow at the top right of each image indicates the warp direction.

ASW_S

The fracture surfaces of the ASW_S specimens were inspected at all temperatures and were found to be quite similar to the fracture surfaces of the ASW_F specimens. Fibre/matrix debonding was identified as the main failure mechanism at temperatures between RT and120 °C, becoming more prominent as the temperature increased. Fibre/matrix debonding occurred at -50 °C but to a much lesser degree since most of the carbon fibres still had residual matrix on their surfaces. Increasing temperature also rendered the matrix more ductile, as the occurrence of ductile failure increased, especially at 90 °C and 120 °C where brittle failure was limited. With respect to the failure location, similarly to ASW_F, 1st ply failure was observed at all testing temperatures and 2nd ply failure only at -50 °C.

At -50 °C, the ASW_S specimens exhibited 1st ply and 2nd ply failure (Figure 5.12), similar to ASW_F specimens. A secondary feature of the fracture surface is the presence of voids in some areas at the overlap edges.

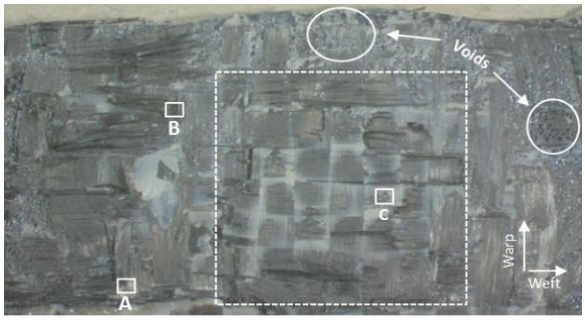

Figure 5.12. Fracture surface of an ASW_S specimen tested at -50°C showing 1st ply failure and 2nd ply failure (the 2nd ply failure is enclosed within the dashed square). In addition, voids were also observed (e.g. the two circled areas). A, B and C represent the locations at which the SEM micrographs were captured.

The SEM micrographs (Figure 5.13) revealed exposed carbon fibres, which indicated the occurrence of fibre/matrix debonding, however, in most areas the carbon fibres had matrix remnants on their surfaces. A typical example is Figure 5.13A where, apart from only one broken fibre (bottom of the SEM micrograph) that has very little amount of matrix left on its surface, all other carbon fibres are still covered with matrix. Figure 5.13B also shows a similar fracture surface as most of the fibres of the broken fibre bundle have residual matrix on their surfaces, and only few areas of carbon fibres are exposed (i.e. fibres partially stripped of resin). Similarly to ASW_F specimens at -50 °C, both ductile and brittle matrix failure modes were identified. Matrix ductility was signified by deformed matrix which was drawn over the carbon fibres surfaces, a fractographic feature that was observed in several locations (Figure 5.13B for example). However, brittle failure appeared to occur more frequently than ductile failure, as the fractographic analysis revealed. Brittle failure was distinguished from ductile failure by characteristic features like cusps (Figure 5.13A) and by limited plastic deformation (Figure 5.13C and Figure 5.13D). In comparison to the ASW_F specimens, brittle failure in ASW_S specimens appeared to have occurred more frequently.

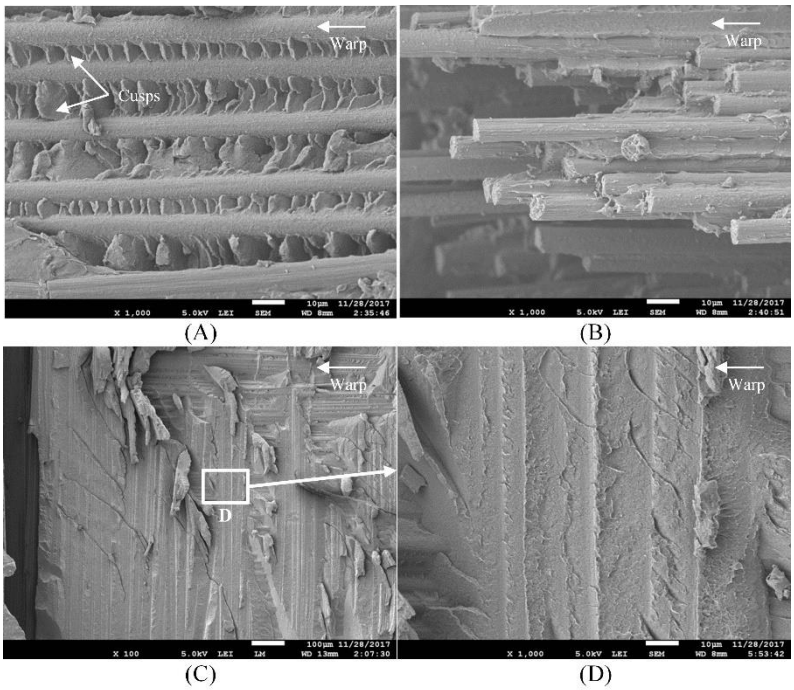

Figure 5.13. SEM micrographs of locations A and B of **Figure 5.12**: (A) Cusps, indicating brittle failure, and fibres still covered with resin. (B) Broken fibre bundle with most fibres still covered with resin. (C) Resin rich area dominated by brittle failure. (D) Magnification of location D of Figure 5.13C, showing a resin rich area. The arrow at the top right of each image indicates the warp direction.

Figure 5.14 illustrates a representative fracture surface of an ASW_S specimen tested at 120 °C, showing 1st ply failure, accompanied by areas of voids. The SEM micrographs (Figure 5.15A and Figure 5.15B) illustrate extensive fibre/matrix debonding where bare fibres can be seen. In addition, Figure 5.15B shows considerable matrix drawing, which indicates ductile failure.

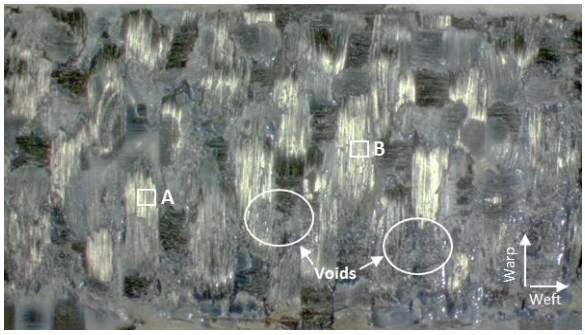

Figure 5.14. Fracture surface of an ASW_S specimen tested at 120°C showing 1st ply failure accompanied by areas of voids (e.g. the two circled areas). A and B represent the locations at which the SEM micrographs (Figure 5.15) were captured.

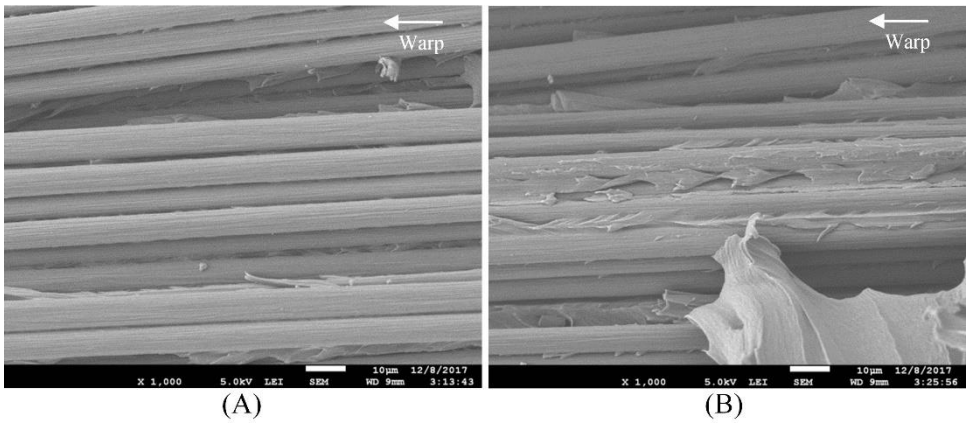

Figure 5.15. SEM micrographs of locations A and B of **Figure 5.14**: (A) & (B) Extensive fibre/matrix debonding accompanied by ductile failure. The top right of each image indicates the direction of the fibres. The arrow at the top right of each image indicates the warp direction.

ANN_F

Similar to the two as-welded series, the fracture surfaces of the annealed specimens were investigated at all temperatures. Cohesive failure (i.e. failure within the resin rich area of the weldline) and 1st ply failure were identified in all specimens at all temperatures. Cohesive failure was the dominant failure mechanism at -50 °C but its occurrence diminished with increasing temperature, while fibre/matrix debonding became more pronounced. Similar to the other two series, matrix ductility was also more pronounced with increasing temperature. Furthermore, a significant amount of voids was observed in all cases and these did not seem to be affected by the testing temperature. It is suggested that the voids were a consequence of the annealing process as the amount of voids in ANN_F was much higher than the amount of voids in ASW_F (both series were welded using the same conditions). Only at 120 °C, did the ASW_F specimens exhibit similar void formation to ANN_F. However, this was probably due to the 10 minutes pre-conditioning at 120 °C of the single lap joints prior to testing, which, in fact, supports the idea that the voids were a product of the annealing process.

Figure 5.16 illustrates the fracture surface of an ANN_F specimen tested at -50 °C where 1st ply failure and cohesive failure at the weldline can both be observed. The fracture surface appears to have a substantial amount of resin rich areas, and the occurrence of cohesive failure was confirmed by the SEM micrographs (Figure 5.17). An important point to be made from Figure 5.16 is the significant amount of voids that are present. A more detailed view of the voids is shown in Figure 5.17A and Figure 5.17B, where small and large voids are randomly distributed. Most fibres were covered by thick resin layers (Figure 5.17C), however, fibre/matrix debonding was also observed (Figure 5.17D). The latter was not the most dominant failure mode as most of the failure occurred within the bulk matrix of the weldline (cohesive failure). Ductile matrix failure took place as the smeared matrix (Figure 5.17C) and the localised matrix drawing (Figure 5.17D) demonstrate, however, brittle matrix failure was more prevalent, as the overall limited plastic deformation of the matrix signified. An example of brittle failure can be seen in Figure 5.17A and Figure 5.17B, where cracks were formed within resin-rich areas of the weldline.

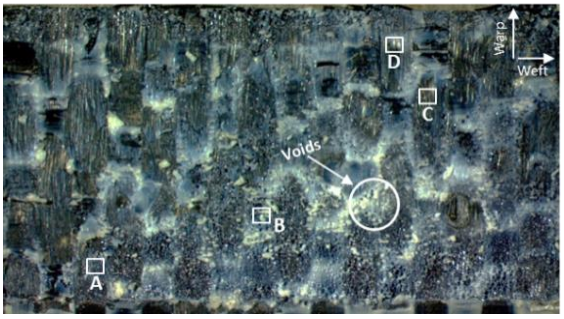

Figure 5.16. Fracture surface of an ANN_F specimen tested at -50°C showing cohesive failure accompanied by extensive areas of voids (e.g. circled area). A-D represent the locations at which the SEM micrographs were captured.

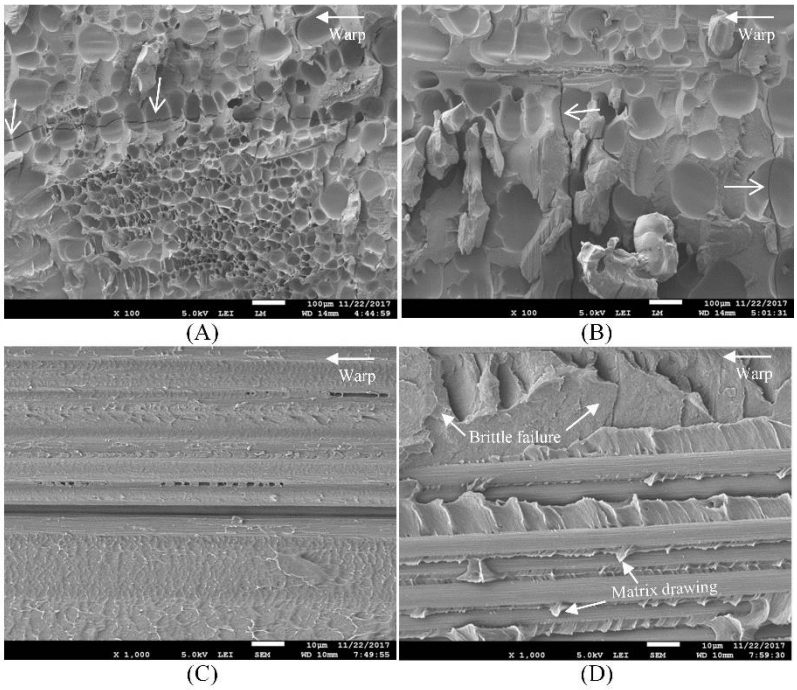

Figure 5.17. SEM micrographs of locations A-D of **Figure 5.16**: (A) & (B) Extensive areas of small and large voids, randomly distributed. Arrows point at cracks formed with limited plastic deformation. (C) Smeared matrix indicating ductile failure. (D) Combination of brittle failure, as it can be seen at the top of the picture, and ductile failure indicated by matrix drawing. Some exposed fibres can also be observed indicating fibre/matrix debonding. The arrow at the top right of each image indicates the warp direction.

The fracture surface of an ANN_F specimen, tested at 120 °C, is illustrated in Figure 5.18 where both 1st ply and cohesive failures at the weldline can be seen. The failure was accompanied by extensive areas of voids, similarly to specimens tested at all the other temperatures (including -50 °C). Contrary to the specimens tested at -50 °C, at 120 °C fibre/matrix debonding was more prevalent, as Figure 5.19A and Figure 5.19B demonstrate. Ductile failure of the matrix was also prevalent at this temperature; an example of ductile failure can be seen in Figure 5.19A in which a large area of matrix between the fibres is deformed.

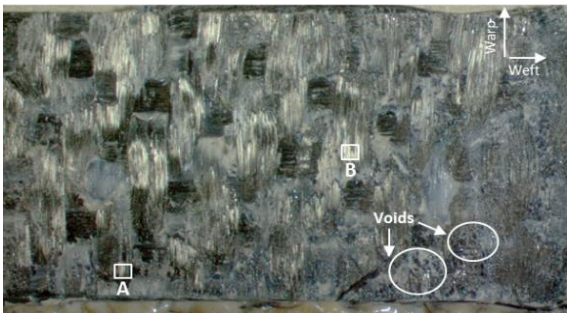

Figure 5.18. Fracture surface of an ANN_F specimen tested at 120°C showing cohesive failure accompanied by extensive areas of voids (e.g. the two circled areas). A and B represent the locations at which the SEM micrographs were captured.

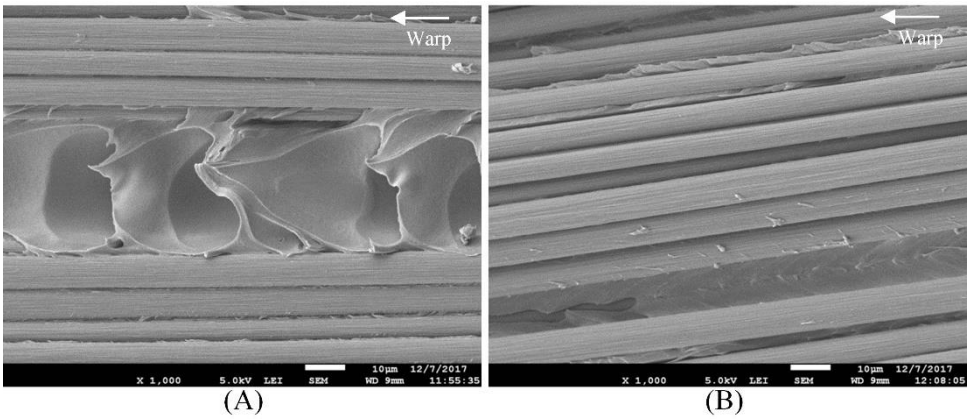

Figure 5.19. SEM micrographs of locations A and B of **Figure 5.18**: (A) & (B) Extensive fibre/matrix debonding accompanied by ductile failure. The arrow at the top right of each image indicates the warp direction.

5.4 Discussion

In this section, the influence of temperature on the lap shear strength and the failure mechanisms of UW CF/PPS joints are discussed, followed by the correlation of the degree of crystallinity of PPS to the lap shear strength and to the failure mechanisms.

The overall trend of the single lap shear tests was decreasing lap shear strength with increasing temperature. In order to summarise the results and facilitate the reader, Figure 5.20 unifies the three previous LSS graphs (Figure 5.5 – Figure 5.7) into one chart. The main points deduced from Figure 5.20 are the following:

(i) The highest LSS was obtained at -50 °C by ASW_F.
(ii) At -50 °C and RT, ASW_F showed higher LSS compared to the other two series, while at 50 °C and above, ANN_F exhibited higher LSS than the two as-welded series.
(iii) At 90 °C, the LSS of ANN_F was substantially higher than the LSS of both as-welded series, namely 43% higher than ASW_F and 26% higher than ASW_S.
(iv) The LSS of ASW_F and ASW_S remained virtually constant at 90 °C and 120 °C, while the LSS of ANN_F showed a further decrease. At 120 °C, the difference between the LSS of ANN_F and the two as-welded series decreased significantly with respect to 90 °C; the LSS of ANN_F was 28% and 13% higher than those of ASW_F and ASW_S, respectively.

(v) At high temperatures (90 °C and 120 °C) the specimens welded with the slowest welding process (ASW_S) exhibited better mechanical performance than the ones with the fastest welding process (ASW_F).

In section 5.3.2.2 a fractography analysis was conducted, classifying the failure mechanisms according to failure locations and type of fracture. The main failure mechanism at all temperatures was identified as fibre/matrix debonding except for -50 °C where the failure mechanism was primarily matrix fracture. In the case of the annealed joints, cohesive failure co-occurred, however, its presence diminished with increasing temperature. The fracture morphologies of bare fibres or fibres with little amount of residual matrix on their surfaces indicate that the failure can be associated with the strength of the fibre/matrix interface. Such fractographic features were even more prevalent at higher temperatures. On these grounds, it seems fair to suggest that the lap shear strength of UW CF/PPS joints can be related to the fibre/matrix interfacial strength and that the latter deteriorated with increasing temperature, contributing to the reduction in LSS.

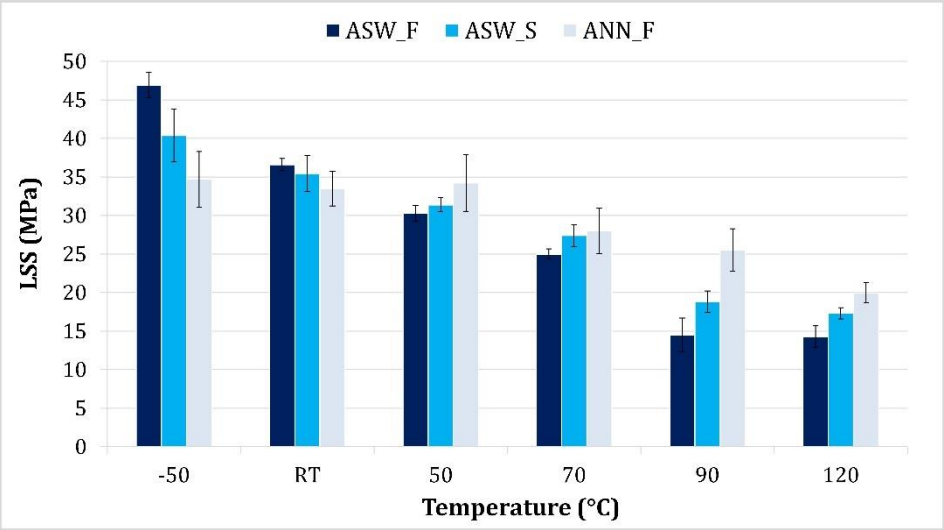

Figure 5.20. Temperature dependence of LSS of ASW_F, ASW_S, and ANN_F.

In chapter 2 a similar result was observed, where the overall behaviour of LSS of RW GF/PPS joints was to decrease with increasing temperature. The main mechanism governing the carbon fibre/matrix interfacial strength is the same as in the glass fibre/matrix interfaces and is of physical (mechanical) nature. During cooling the matrix shrinks more than the fibres due to the higher CTE of the matrix [27][28], resulting in the formation of compressive radial stresses around the fibres. The asperities of the fibre surfaces allow for better "mechanical gripping" of the fibres by the matrix, promoting static frictional stresses during loading and, therefore, enhancing the mechanical interlocking [13][14][16][27][29]. As it was suggested in chapter 2, the increase in testing temperature (which decreases the ΔT) may partially relieve the residual thermal stresses that were formed during cooling between the fibres and the matrix, and weaken the mechanical interlocking. This phenomenon is also demonstrated by the failure at -50 °C where fibre/matrix debonding was less pronounced and many areas with fibres having residual matrix on their surfaces were observed, indicating matrix fracture. Most likely, the strength of the fibre/matrix interface at -50 °C was high enough due to the high ΔT that failure occurred within the bulk matrix of the resin rich areas of the adherends because the matrix strength was reached first. In addition, the static frictional stresses at the fibre/matrix interface will decrease due to the reduction of the compressive radial stresses (since the frictional stresses are proportional to the radial stresses) and further reduce the interfacial shear strength (IFSS) [13][16]. The increase of temperature also diminished the

ability of the matrix to transfer load to the fibres, by causing a significant drop in the elastic modulus of the matrix at T ≥ Tg (Figure 5.2). An effective stress transfer between the matrix and the fibres is vital for a high IFSS and is directly related to the matrix elastic modulus, as it has been previously demonstrated in literature [14][15][30][31]. All series showed a large drop in LSS at high temperatures, a drop that was in line with the evolution of the elastic modulus of PPS with temperature (Figure 5.2); this phenomenon demonstrates the heavy dependence of LSS on the elastic modulus of the matrix. However, the elastic modulus of the matrix is not only influenced by the temperature but by the crystallinity degree of the matrix as well [11][12]. The latter varied substantially among the three series (Figure 5.1) and as it was shown in Figure 5.2 and in Figure 5.20, the temperature dependence of elastic modulus and LSS were also different among the three series. The next paragraphs attempt to connect the LSS of the three series to the crystallinity degree of PPS at the weldline.

The role of crystallinity on the weld performance appeared to be more critical at low and high temperatures (-50 °C, 90 °C and 120 °C). In Figure 5.20 it was shown that between RT and 70 °C there were small differences in LSS among the three series at each temperature, while at the extreme temperatures significant differences were observed. At -50 °C, the higher toughness and ductility of amorphous PPS [22] was probably favourable for the lap shear strength. The examination of the fracture surfaces revealed that at -50 °C matrix failure was both ductile and brittle. The ASW_F specimens showed more areas of ductile failure at -50 °C than the ASW_S specimens, which could be attributed to the amorphous state of PPS in the ASW_F specimens. Compared to the ASW_F specimens, the annealed specimens also showed less areas of ductile matrix failure, reinforcing the idea that the ductile failure was a result of the amorphous state of PPS, which was more prevalent in ASW_F. It is noted though, that the occurrence of brittle fracture can also be promoted by a number of additional factors: (i) in the as-welded joints the failure progressed in the 2nd ply, where the cooling rate during welding could have been lower than it was in the weldline and, therefore, the degree of crystallinity would have been higher, leading to a stiffer and more brittle matrix; and (ii) the failure in a single lap shear test is sudden, thus, a more unstable crack occurred promoting brittle fracture [32]-[34], especially at low temperatures where the failure loads were high. Regarding the LSS of ANN_F at -50 °C it seems that it was also compromised by the presence of voids which most likely formed during annealing. The failure propagated easier through the voids, instead of occurring in the 1st and 2nd plies as in the as-welded joints, resulting in lower strength. In addition, the presence of voids was most likely the reason for the high scatter in the LSS of the ANN_F specimens at most temperatures since the size and location of the voids were distributed across the overlap, leading to variations in strength. The cause of void formation remains unclear, however, two possibilities are the shrinkage due to crystallization, and/or the absence of pressure during the annealing process. Further investigation is required to determine the origin of the voids, however, it goes beyond the scope of this study.

At high temperatures (90 °C and 120 °C) the presence of crystallinity appeared to be beneficial. The decrease in LSS at 90 °C with respect to RT was smaller for ANN_F, than the one for ASW_F (Figure 5.20), a behaviour that could be associated to the higher crystallinity of the former, as explained in what follows. As it was discussed previously, the significant drop in the elastic modulus of the matrix at temperatures higher than the Tg can deteriorate the stress transfer between the matrix and the fibres and eventually cause a reduction in LSS. As illustrated in Figure 5.2, the Tg of annealed PPS is higher than the Tg of amorphous PPS. Thus, in the vicinity of 90 °C, the stress transfer between PPS and CF would be more efficient for ANN_F than ASW_F, resulting in a stronger fibre/matrix interfacial strength for the former and, essentially, in a higher LSS. However, the glass transition temperature is closely related to the crystallinity degree of the matrix: in Figure 5.1 and Figure 5.2 it can be seen that higher

crystallinity degree is linked to a higher Tg. The shift of the glass transition to higher temperatures with increasing crystallinity has been observed by other researchers as well [35]-[40]. The mobility of the non-crystalline chain segments is hindered by the crystalline lamellae, especially in polymers with a semi-rigid backbone like PPS [39].

Another demonstration of the influence of crystallinity degree on the weld performance in relation to temperature, is the thermal expansion behaviour of PPS: the increase in the thermal expansion rate, which can weaken the mechanical interlocking between the matrix and the fibres, was not so significant for annealed PPS as it was for amorphous PPS. In addition, the increase in thermal expansion rate of annealed PPS took place around 92 °C due to the restrictions imposed by the crystalline domains on the chain mobility. On the contrary, the significant thermal expansion of amorphous PPS occurred at a lower temperature, around 83 °C, contributing to the reduction in LSS of ASW_F at 90 °C. The effect of crystallinity on LSS was also demonstrated in the LSS of ASW_S at 90 °C (Figure 5.20), which was in between the LSS of ASW_F and ANN_F. The slower welding process resulted in PPS of moderate crystallinity degree, lower than that of ED_Ref. Considering that the glass transition temperature is related to the crystallinity degree it seems plausible to assume that the Tg and the increase in the thermal expansion rate of ASW_S would be between those of ASW_F and ANN_F, hence, resulting in a LSS between the two other series, at high temperatures.

The impact of crystallinity on the LSS is also shown at 120 °C. It is suggested that the negligible LSS reduction of ASW_F, with respect to 90 °C, occurred primarily due to the cold crystallization of PPS at 120 °C (during conditioning of the welded joints prior to mechanical testing). Figure 5.1 shows a major increase in the degree of crystallinity due to conditioning of the welded joints at 120 °C for 10 minutes, Figure 5.2 shows a sharp increase in the elastic modulus of PPS around 120 °C, and Figure 5.4 illustrates a decrease in the thermal expansion rate of PPS right after the shrinkage corresponding to cold crystallization. On the basis of this evidence, and taking into consideration the earlier discussion on the mechanisms governing the IFSS, it can be argued that the increase in the degree of crystallinity of PPS due to cold crystallization acted as a competing mechanism against the negative effect of the further decrease in ΔT, by increasing the elastic modulus of PPS. A similar behaviour was observed for the ASW_S specimens at 120 °C, which displayed a minor decrease in LSS of 8% with respect to 90 °C. The ASW_S specimens were cold-crystallized as well during conditioning prior to testing (Figure 5.1), however, contrarily to the ASW_F specimens which changed from an amorphous state to a semi-crystalline state, the former already possessed moderate crystallinity, therefore, the increase in the crystallinity degree was probably not as pivotal as it was for the LSS of ASW_F specimens. On the contrary, no changes in crystallinity were expected for ANN_F; already annealed at a high temperature and for a long duration (200 °C, 2 hours), 10 minutes of conditioning at 120 °C would not bring significant changes in the PPS state. Hence, as the Tg of annealed PPS occurred well below 120 °C (close to 100 °C, taken from the drop in storage modulus shown in Figure 5.2), a sharp reduction in the LSS of ANN_F took place at 120 °C (which is in line with the analysis on the effect of Tg on the LSS).

As previously mentioned, the higher toughness and ductility of amorphous PPS were proven to be beneficial for the LSS at -50 °C, however, their impact at high temperatures appeared to be negligible. The effects of toughness and ductility at high temperatures have been studied by other researchers who reported that the mode-I critical strain energy release rate (G_{IC}) propagation values increased with temperature due to increased matrix ductility [41]-[43]. However, since the failure in single lap shear tests is sudden and since the joint is mainly loaded in shear in the middle of the overlap [44], the G_{IC} initiation values are considered to be more relevant for the single lap shear tests than the G_{IC} propagation values. With respect to the former, Kim et al [41] found that at high temperatures the initiation values decreased, a

phenomenon that they attributed to the weakened IFSS. Therefore, it is suggested that the beneficial effect of higher matrix ductility on the Mode-I interlaminar fracture toughness at high temperatures was negated by the poor IFSS.

Taking into account the discussion on the benefits of an amorphous PPS state and a semi-crystalline PPS state at the weldline, it is suggested that between RT and 70 °C the higher toughness and ductility of amorphous PPS counterbalanced the higher stiffness and higher IFSS of semi-crystalline PPS, resulting in minor differences in LSS among the three series.

A final remark about the temperature dependence of the welded joints concerns the effect of the single lap joint geometry on the reduction of LSS. In chapter 2, the stress state at the joint overlap during single lap shear testing was described and is also mentioned here as a reminder. The single lap shear test induces secondary bending to the joint because of the load eccentricity which exacerbates the peel stresses at the edges of the overlap. Similarly, the longitudinal deformation of the adherends and the weldline can influence the uniformity of shear stress distributions at the joint overlap. Higher adherend stiffness and/or lower weldline stiffness can lead to more uniform shear stress distributions.

Looking at the LSS results in Figure 5.20, it can be seen that the largest differences between the series occurred at -50 °C, at 90 °C and at 120 °C. Between -50 °C and 70 °C the matrix modulus remained fairly constant, a trend observed in both amorphous and semi-crystalline PPS. Therefore, it could be argued that the stress state was virtually the same within this temperature range for each series and did not contribute to the LSS reduction with increasing temperature. With respect to the annealed series, the LSS seemed to be mainly weakened by the porosity of the weldline. The stress state at the overlaps of ANN_F joints probably remained the same up to 90 °C, considering that the Tg of annealed PPS was higher than 90 °C (Figure 5.2).

At 90 °C, the stress state at the joint overlap could be a key factor for the LSS reduction of ASW_F. The abrupt drop in the elastic modulus of amorphous PPS at 85 °C implies that the weldline modulus of ASW_F would be substantially lower at 90 °C compared to 70 °C. This could lead to more uniform shear stress distributions at the weldline, however, its effect could be counteracted by the lower weldline shear strength as well as by the reduction in the adherend modulus around 90 °C, as seen in the DMA curve of CF/PPS (Figure 5.3). The lower adherend modulus could, instead, lead to less uniform shear stress distributions and could enhance secondary bending in ASW_F, exacerbating the peel stresses. While this modulus reduction was not significant (around 7% with respect to RT), it might have been larger for ASW_F compared to the other two series. The lower PPS modulus in the 1st ply of the ASW_F adherends compared to the respective ones in ASW_S and ANN_F (as shown in chapter 4), indicates a lower crystallinity and Tg of PPS and, therefore, the modulus reduction can be expected to be larger than 7%.

The role of the stress state on the mechanical performance of the welds became more critical at 120 °C where the secondary bending was probably much more pronounced, for all series. As the DMA curve of CF/PPS in Figure 5.3 shows: the storage modulus reduction at 120 °C was 28% with respect to RT. At 120 °C, the beneficial effect of the lower weldline modulus on the stress distributions was most likely marginalised or completely eliminated by the combined effects of the lower matrix shear strength, lower adherend modulus and, most importantly, of the enhanced peel stresses due to pronounced secondary bending.

5.5 Conclusions

This study elucidated the effect of temperature on the lap shear strength and the failure mechanisms of UW CF/PPS joints by linking the weld performance to the degree of crystallinity of PPS at the weldline. Single lap shear tests were performed at temperatures ranging from -50 °C to 120 °C on two series of welded joints (as-welded), one with an amorphous and one with a semi-crystalline weldline, and on one series of annealed welded joints which had the weldline with the highest possible crystallinity degree, among the three series.

The single lap shear tests showed an overall trend of decreasing lap shear strength with increasing temperature, with the exception of two temperature regions, -50 °C to 50 °C for the annealed series, and 90 °C to 120 °C for the two as-welded series, where the LSS remained virtually constant. The highest LSS was measured at -50 °C for the joints with amorphous weldline, being 26% and 14% higher than the LSS of the annealed joints and of the as-welded joints with semi-crystalline weldline, respectively. Contrarily, at 120 °C the highest LSS was found in the annealed series, 28% and 13% higher than the LSS of the as-welded joints with amorphous and with semi-crystalline weldline, respectively. The detailed fractographic analysis carried out through SEM, revealed that at -50 °C, in both as-welded series, the fibres were mainly or partially covered with residual matrix. At room temperature and above, more exposed fibres were observed with very little or zero amount of matrix left on their surfaces, features that became more pronounced with increasing temperature, especially at and above the glass transition temperature of PPS. On the basis of this evidence it was suggested that the main failure mechanism of the two as-welded series at all temperatures, except -50 °C, was fibre/matrix debonding, a failure mode that became more prevalent with increasing temperature, especially at and above the glass transition temperature of PPS. The annealed series exhibited cohesive failure in all specimens at all temperatures but its occurrence diminished with increasing temperature, while fibre/matrix debonding became more pronounced. It was also found that the annealed specimens exhibited porosity in the weldline, which was related to the annealing process, and played a primary role in causing cohesive failure.

A higher degree of crystallinity of PPS at the weldline was found to be beneficial at high temperatures (90 °C and 120 °C), probably due to the higher elastic modulus and, hence, due to the higher fibre/matrix interfacial strength compared to amorphous PPS. Cold crystallization of both as-welded series due to conditioning at 120 °C prior to mechanical testing was found to have a profound effect on the LSS, causing the LSS of both series to remain virtually constant at 90 °C and 120 °C. However, at low temperatures (-50 °C) amorphous weldlines were proven to be more beneficial, most likely due to the higher toughness and ductility of amorphous PPS compared to semi-crystalline PPS, since at -50°C the matrix failure became the most predominant failure mode as opposed to fibre/matrix debonding. Furthermore, between room temperature and 70 °C only minor differences in LSS were observed amongst all series, indicating that there was little effect of the degree of crystallinity above room temperature to just below the glass transition temperature.

The stress state at the joint overlap appeared to be critical only at elevated temperatures (90°C and 120°C) mainly because of the more pronounced secondary bending that can result in enhanced peel stresses. In addition, it was suggested that the secondary bending effect was more critical in the as-welded joints with amorphous weldline.

In conclusion, this study has demonstrated that both states of PPS – amorphous and semi-crystalline – can be beneficial for the performance of UW CF/PPS joints in dry conditions,

depending on the service temperature. Arguably, a semi-crystalline PPS would allow joints to be used at higher temperatures while an amorphous PPS, as long as the service temperature remained below the glass transition temperature, could be preferable due to its even better performance at low temperatures. Please note that these conclusions refer exclusively to welded joints in dry conditions and not exposed to moisture or any chemical environments. Hence, further studies on the chemical resistance of UW CF/PPS joints are required to identify the material limits.

Bibliography

[1] Rohart V, Dubé M, Laberge Lebel L. Effects of temperature on the apparent lap shear strength of resistance-welded carbon fibre/thermoplastic composite joints. In: International SAMPE technical conference 2018-May; 1-10.
[2] Tolunay MN, Dawson PR, Wang KK. Heating and bonding mechanisms in ultrasonic welding of thermoplastics. Polym Eng Sci 1983; 23(13): 726-33.
[3] Benatar A, Gutowski TG. Ultrasonic welding of PEEK graphite APC-2 composites. Polym Eng Sic 1989; 29(23): 1705-21.
[4] Potente H. Ultrasonic welding – principles and theory. Mater De 1984; 5(5): 228-34.
[5] Levy A, Le Corre S, Villegas IF. Modeling of the heating phenomena in ultrasonic welding of thermoplastic composites with flat energy directors. J Mater Process Technol 2014; 214: 1361-1371.
[6] Villegas IF. Strength development versus process data in ultrasonic welding of thermoplastic composites with flat energy directors and its application to the definition of optimum processing parameters. Composites: Part A 2014; 65: 27-37.
[7] Villegas IF. In situ monitoring of ultrasonic welding of thermoplastic composites through power and displacement data. J Thermoplast Compos Mater 2015; 28: 66-85.
[8] Palardy G, Villegas IF. On the effect of flat energy directors thickness on heat generation during ultrasonic welding of thermoplastic composites. Comp Interfaces 2017; 24:2, 203-214.
[9] Villegas IF, Palardy G. Ultrasonic welding of CF/PPS composites with integrated triangular energy directors: melting, flow and weld strength development. Composite Interfaces 2017; 24(5): 515-528.
[10] Zhao T, Palardy G, Villegas IF, Rans C, Martinez M, Benedictus R. Mechanical behaviour of thermoplastic composites spot-welded and mechanically fastened joints: a preliminary comparison. Composites Part B: Engineering 2017; 112: 224-234.
[11] Talbott MF, Springer GS, Berglund LA. The effects of crystallinity on the mechanical properties of PEEK polymer and graphite fiber reinforced PEEK. J Comp Mater 1987; 21: 1056-1081.
[12] Spruiell JE, Janke CJ. A review on the measurement and development of crystallinity and its relation to properties in neat poly(phenylene sulfide) and its fiber reinforced composites. Technical Report, Oak Ridge National Laboratory, 2004.
[13] Thomason JL, Yang L. Temperature dependence of the interfacial shear strength in glass-fibre polypropylene composites. Composites Science and Technology 2011; 71: 1600-1605.
[14] Rao V, Drzal LT. The temperature dependence of interfacial shear strength for various polymeric matrices reinforced with carbon fibers. Journal of Adhesion 1992; 37: 88-95.
[15] Rao V, Drzal LT. The dependence of interfacial shear strength on matrix and interphase properties. Polymer Composites 1991; 12 (1): 48-56.
[16] Di Landro L, Pegoraro M. Evaluation of residual stresses and adhesion in polymer composites. Composites Part A 1996; 27A: 847-853.
[17] Gao SL, Kim JK. Cooling rate influences in carbon fibre/PEEK composites. Part 1. Crystallinity and interface adhesion. Composites: Part A 2000; 31: 517-530.
[18] Gao SL, Kim JK. Correlation among crystalline morphology of PEEK, interface bond strength, and in-plane mechanical properties of Carbon/PEEK composites. Journal of Applied Polymer Science 2002; 84: 1155-1167.

[19] Schulz E, Kalinka G, Auersch W. Effect of transcrystallization in carbon fiber reinforecd poly(p-phenylene sulfide) composites on the interfacial shear strength investigated with the single fiber pull-out test. J Macromol Sci Part B 1996; 35(3-4): 527-546.
[20] Liu B, Wang X, Long S, Yang J. Interfacial micromechanics of carbon fiber-reinforced polyphenylene sulfide composites. Composite Interfaces 2014; 21(4): 359-369.
[21] Gao SL, Kim JK. Cooling rate influences in carbon fibre/PEEK composites. Part II: interlaminar fracture toughness. Composites: Part A 2001; 32: 763-774.
[22] Sacchetti F, Grouve WJB, Warnet LL, Villegas IF. Effect of cooling rate on the interlaminar fracture toughness of unidirectional carbon/PPS laminates. Eng Fract Mech 2018; 203: 126-136.
[23] ASTM Standard D 3518/D 3518M – 94, 2001, "Standard Test Method for In-Plane Shear Response of Polymer Composite Materials by Tensile Test of a ±45° Laminate", ASTM International, West Conshohocken, PA.
[24] Huo P. Cebe P. Effects of thermal history on the rigid amorphous phase in poly(phenylene sulfide). Colloid Polym Sci 1992; 270: 840-852.
[25] Barnes JA, Byerly GE. The formation of residual stresses in laminated thermoplastic composites. Composites Science and Technology 1994; 51: 479-494.
[26] Menard KP. Dynamic Mechanical Analysis. A practical introduction. CRC Press 3rd edition, 2008.
[27] Parlevliet PP, Bersee HEN, Beukers A. Residual stresses in thermoplastic composites – A study of the literature – Part I: Formation of residual stresses. Composites: Part A 2006; 37: 1847-1857.
[28] Tanaka K, Hosoo N, Katayama T, Noguchi Y, Izui K. Effect of temperature on the fiber/matrix interfacial strength of carbon fiber reinforced polyamide model composites. Mechanical Engineering Journal 2016; 3(6): 1-8.
[29] Kim JK, Mai YW. Engineered Interfaces in Fiber Reinforced Composites. Elsevier, 1998.
[30] Zhang Q, Liang S, Sui G, Yang X. Influence of matrix modulus on the mechanical and interfacial properties of carbon fiber filament wound composites. RSC Adv 2015; 5: 25208-25214.
[31] Sottos NR, Li L, Agrawal G. The effects of interphase properties on interfacial shear strength in polymer matrix composites. J. Adhesion 1994; 45: 105-124.
[32] Purslow D. Matrix fractography of fibre-reinforced thermoplastics, Part 1. Peel failures. Composites 1987; 18(5): 365-374.
[33] Purslow D. Matrix fractography of fibre-reinforced thermoplastics. Part 2. Shear failures. Composites 1988; 19(2): 115-126.
[34] Greenhalgh E. Failure analysis and fractography of polymer composites. CRC Press, 2009.
[35] Huo P. Cebe P. Effects of thermal history on the rigid amorphous phase in poly(phenylene sulfide). Colloid Polym Sci 1992; 270: 840-852.
[36] Ferrara JA, Seferis JC, Sheppard CH. Dual-mechanism kinetics of polyphenylene sulfide (PPS) melt-crystallization. J Thermal Analysis 1994; 42: 467-484.
[37] Scobbo JJ, Hwang CR. Annealing effects in poly(phenylene sulfide) as observed by dynamic mechanical analysis. Polymer Engineering and Science 1994; 34(23): 1744-1749.
[38] Zhang RC, Li R, Lu A, Jin Z, Liu B, Xu Z. The glass transition temperature of poly(phenylene sulfide) with various crystallinities. Polymer Int 2013; 62: 449-453.
[39] Krishnaswamy RK, Geibel JF, Lewis BJ. Influence of semicrystalline morphology on the physical aging characteristics of poly(phenylene sulfide). Macromolecules 2003; 36: 2907-2914.

[40] Jonas A, Legras R. Relation between PEEK semicrystalline morphology and its subglass relaxations and glass transition. Macromolecules 1993; 26: 813-824.
[41] K.Y. Kim, L. Ye, K.M. Phoa. Interlaminar fracture toughness of CF/PEI and GF/PEI composites at elevated temperatures. Applied Composite Materials 2004; 11: 173-190.
[42] K.D. Cowley, P.W.R. Beaumont. The interlaminar and intralaminar fracture toughness of carbon-fibre/polymer composites: The effect of temperature. Composite Science and Technology 1997; 57: 1433-1444.
[43] S. Hashemi, A.J. Kinloch, and J.G. Williams. The effects of geometry, rate and temperature on the Mode I, Mode II and Mixed-Mode I/II interlaminar fracture of carbon-fibre/poly(ether-ether ketone) composites. Journal of Composite Materials 1990; 24(9): 918-956.
[44] da Silva LFM, Öchsner A. Modeling of Adhesively Bonded Joints. Heidelberg: Springer, 2008.

6 Comparative analysis of the behaviour of RW GF/PPS and UW CF/PPS joints

It matters that you don't just give up.

(Stephen Hawking)

The previous chapters presented the results from the exposure of RW GF/PPS joints and UW CF/PPS joints to a wide range of temperatures, while the weldline structure of the latter was meticulously characterised. The focus of this thesis is to evaluate the strength of the welded joints while having a closer look into the failure mechanisms in order to determine the material properties of the weldline and of the adherends that dominate the mechanical performance of the welds at low and high temperatures. Two different welding techniques and two different fibre types were studied, thus, an analysis connecting the results shown in this thesis is clearly needed to broaden our understanding of the thermal effects on thermoplastic composites welded joints. The objective of this chapter is to compare the two welding techniques, resistance welding and ultrasonic welding, and the two types of polymer composites, GF/PPS and CF/PPS, with respect to the weld performance at a wide range of temperatures. Literature data is also used to complement the data presented in this thesis and to reach more solid conclusions.

Before comparing the results in chapter 2 and chapter 5, it is useful to look into existing literature data regarding resistance welding and ultrasonic welding. In separate studies, GF/PEI RW joints and CF/PEI UW joints were found to exhibit similar levels of LSS at room temperature [1]-[3]. Table 6.1 summarises the main findings of those studies and the basic information of the materials used to demonstrate the relevance of the comparisons. The reported LSS values of GF/PEI RW joints were around 32-33 MPa and both studies used similar materials (heating element and adherends). In [3] the LSS of CF/PEI RW joints was also measured, however, the CF/PEI adherends were unidirectional (UD) laminates and hence different to the GF/PEI adherends which were made from woven fabric (8HS). Hence, the LSS of the RW CF/PEI joints was much higher (47 MPa) most likely because of the stiffer adherends (i.e. 50% more fibres in the loading direction and a higher Young's modulus of CF compared to GF) [3]. The work of Villegas [1] on UW CF/PEI joints provides a better comparison though, since the CF/PEI adherends used in that study were made of woven fabric (5HS), a reinforcement type very similar to the one of GF/PEI adherends. For optimum travel values, and depending on the process parameters (welding force, vibration amplitude), the LSS of the CF/PEI welded joints was found between 35 and 37 MPa. In all three studies, the failure primarily occurred within the adherends. The LSS of the CF/PEI welded joints was higher than the GF/PEI welded joints but the relative difference was below 15%. These results suggest that the two types of welded joints and the two types of thermoplastic composites were relatively close in performance, although the CF/PEI welded joints were slightly stronger. Considering the type of failure (i.e. failure within the composite substrate) and the low relative difference between the LSS in both types of joints, it is difficult to determine whether the difference was due to the welding technique or due to the composite type. Nevertheless, a first conclusion from the comparison shown in Table 6.1, is that both techniques, resistance welding and ultrasonic welding, are capable of producing high performance welds. The material compatibility (fibre/matrix and heating element/matrix) seems to play a critical role.

Table 6.1. Comparison of different studies on the LSS of GF/PEI and CF/PEI welded joints.

Study (reference)	LSS (MPa)	Welding Technique	TPC Type	Fibre architecture	HE[1] material	HE[1] dimensions
[3]	33	Resistance Welding	GF/PEI	8 HS[2] Weave	Stainless steel	Diameter (0.04 mm) Open gap width (0.09 mm)
[2]	32	Resistance Welding	GF/PEI	8 HS[2] Weave	Stainless steel	Diameter (0.04 mm) Open gap width (0.09 mm)
[1]	35-37	Ultrasonic Welding	CF/PEI	5 HS[2] Weave	n.a.	n.a.

[1] *HE stands for Heating Element.*
[2] *HS stands for Harness Satin.*

The same comparison can be made between the RW GF/PPS joints (chapter 2) and the UW CF/PPS joints (chapter 5). At room temperature, the former showed an average LSS of approximately 13 MPa while the latter showed an average LSS between 34 and 37 MPa, depending on the process parameters (reminder: the LSS of the annealed joints was lower, 34 MPa, possibly due to the porosity observed at the weldline). In other words, the LSS of the UW CF/PPS joints was more than 150% higher than the LSS of the RW GF/PPS joints. The failure mechanism of the two weld types was similar and identified as fibre/matrix debonding, indicating that the fibre/matrix interfacial strength was dictating the weld performance. On the basis of this evidence, it is suggested that the CF/PPS interfacial strength

was superior than the GF/PPS interfacial strength. In line with this observation is the comparison between the work of Rohart et al [4] and the results presented in chapter 2. Rohart et al. performed single lap shear tests on RW CF/PPS at a wide range of temperatures; they reported consistently higher LSS than the LSS presented in chapter 2, regardless the testing temperature. Both studies used the same type of heating element, however, the fibre architecture was different. In chapter 2, an 8HS GF/PPS weave was used while in [4], a UD CF/PPS tape was used for the production of a quasi-isotropic laminate ($[0/90/\pm45]_{2s}$). A key difference was observed in the failure mechanisms. In the case of GF/PPS welded joints the failure mechanism was primarily fibre/matrix debonding whilst in the case of CF/PPS welded joints it was primarily at the interface of the heating element with the matrix. Hence, the reason for the higher LSS values of the RW CF/PPS joints could be found in the stronger interfacial strength between the carbon fibres and the PPS matrix. Possibly, the LSS of the RW GF/PPS joints would have been higher if the interfacial strength between the glass fibres and PPS was higher.

At this point, in order to manage all the experimental data of the previous chapters as well as the available literature data useful to this discussion, Table 6.2 was compiled. It presents a comprehensive overview of the different welded joints tested at various temperatures, from which the welded CF/PPS composites could be compared with the welded GF/PPS composites. A comparison between the two welding techniques is also possible to be made. For the sake of brevity, the resistance welding series of chapter 2 is denoted by RWGF and the resistance welding series presented in [4] is denoted by RWCF. The three ultrasonic welding series are denoted as in chapter 5.

Table 6.2. Overview of LSS of the experimental data presented in chapters 2 & 5 and of experimental data presented in [4]. The crystallinity degree per weld is also shown when available.

Test Temperature (°C)	Lap Shear Strength (MPa)					Crystallinity Degree (%)			
	Resistance Welding		Ultrasonic Welding			Resistance Welding	Ultrasonic Welding		
	RWGF	RWCF	ASW_F	ASW_S	ANN_F	RWGF	ASW_F	ASW_S	ANN_F
-50	*16.8*	-	*46.9*	*40.3*	*34.7*				
23	*13.1*	*28.5*	*36.6*	*35.5*	*33.5*				
50	*11.5*	-	*30.3*	*31.4*	*34.2*				
62	-	*24.9*	-	-	-				
70	*11.6*	-	*25.0*	*27.4*	*28.0*	*16*	*2.4*	*14.6*	*23.4*
82	-	*21.1*	-	-	-				
90	*11.1*	*18.1*	*14.5*	*18.8*	*25.6*				
120	*9.8*	*14.3**	*14.3*	*17.3*	*20.0*				
150	*8.5*	*11.2*	-	-	-				

** RWCF was tested at 118 °C.*

Prior to any data comparison, a brief explanation on why the crystallinity degree was not considered as a governing factor in this comparison, follows. In chapter 3, section 3.3.2, it was estimated through equation (3.6) that the crystallinity degree of PPS at the weldline of RW GF/PPS joints would be around 16%. Comparing the LSS of RWGF with the LSS of ASW_F (weld with the lowest weldline crystallinity) it can be seen that the latter was always higher at all temperatures. Either in amorphous or in semi-crystalline state, PPS formed a stronger interface with carbon fibres than with glass fibres. Hence, by taking into account the estimated crystallinity degree of PPS at the weldline of RWGF, crystallinity could be excluded from the main factors causing the lower LSS of RWGF. With respect to RWCF, no crystallinity degree was estimated because the temperature profile was unknown. Assuming the same temperature profile as in RWGF would be wrong, due to the different thermal conductivities and fibre architectures of CF/PPS and GF/PPS adherends. Nonetheless, considering the longer welding times of resistance welding (Rohart et al [4] reported a heating time of 60

seconds and a cooling time of 30 seconds) compared to the welding times of ultrasonic welding, it can be assumed that RWCF had a crystallinity degree at least similar to the one of ASW_S.

Coming back to the comparison of the composite types (CF/PPS vs GF/PPS), Figure 6.1 illustrates the LSS ratio of RWGF to the CF/PPS welded joints using the data of Table 6.2. The following can be deduced from Table 6.2 and Figure 6.1:

- At temperatures below and including 70 °C there was a significant difference between the LSS of GF/PPS welded joints and the LSS of CF/PPS welded joints. The ratio between RWGF and any of the CF/PPS welded joints (resistance and ultrasonically welded) was below 0.5.
- At 90 °C the ratio between the LSS of RWGF and ASW_F was around 0.77, much closer than any other series. However, this was most likely a consequence of the lower glass transition temperature of amorphous PPS, for reasons analysed in chapter 5.
- At 150 °C the ratio between RWGF and RWCF was also around 0.76. Overall, the ratios of RWGF with RWCF, ASW_F and ASW_S was higher than 0.5 at 90 °C and above. From these results it could be argued that while the CF/PPS interfacial strength diminished significantly at temperatures above Tg, it still remained superior than the GF/PPS interfacial strength. As the temperature increased, the significant reduction in the elastic modulus of the matrix most likely dominated the interfacial strength in both fibre/matrix systems, minimizing their differences. Furthermore, it is expected that at high temperatures such as 120 °C and 150 °C, the secondary bending due to the lower modulus will also be more pronounced, having a detrimental effect in both welded joint systems.

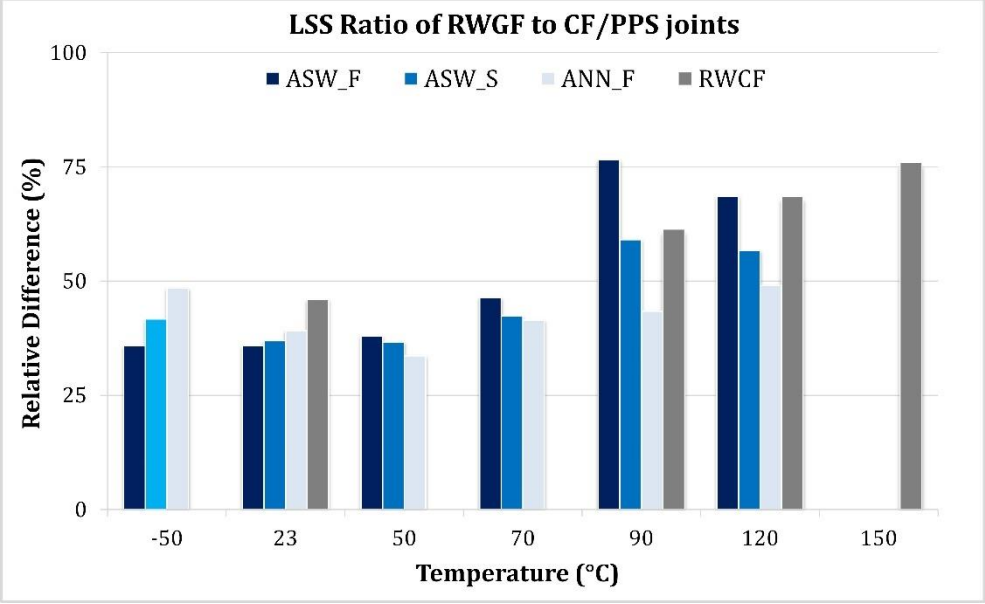

Figure 6.1. LSS Ratio of RWGF to CF/PPS welded joints.

Another observation worthy of mention, is that the LSS of RWGF between 50 °C and 90 °C was fairly constant while for all UW CF/PPS joints, the LSS decreased continuously in that temperature region. This "strength plateau" observed in the case of the RW GF/PPS joints was attributed to the lowering of shear stress concentrations and the distribution of stresses over a larger area. This phenomenon was linked to the decrease in the IPS modulus of GF/PPS which was in line with the premature decrease in the storage modulus of GF/PPS at around 50 °C,

observed in DMA measurements. A secondary peak in the loss modulus of GF/PPS was observed with onset at around 50 °C as well. However, the DMA curve of CF/PPS did not show any secondary transitions. To facilitate the reader, Figure 6.2 illustrates the DMA curves of both GF/PPS and CF/PPS (shown in chapters 2 and 5, respectively). As can be seen, the drop in E' of CF/PPS only started at around 80 °C while the drop in E' of GF/PPS at 50 °C and at 70 °C with respect to 23 °C was already 5% and 17%, respectively. From this standpoint, the continuous LSS reduction of the UW CF/PPS joints between 50 °C and 90 °C, in conjunction with the absence of any secondary transitions in the DMA curve of CF/PPS, seem to confirm the hypothesis about the "strength plateau" in RWGF. Overall, the largest differences between the three UW CF/PPS joints were observed at -50, 90 and 120 °C. Considering the stability of PPS and CF/PPS elastic modulus between -50 °C and 70 °C, it can be argued that the stress state was virtually the same within this temperature range in each series and, therefore, did not contribute to the LSS reduction with increasing temperature.

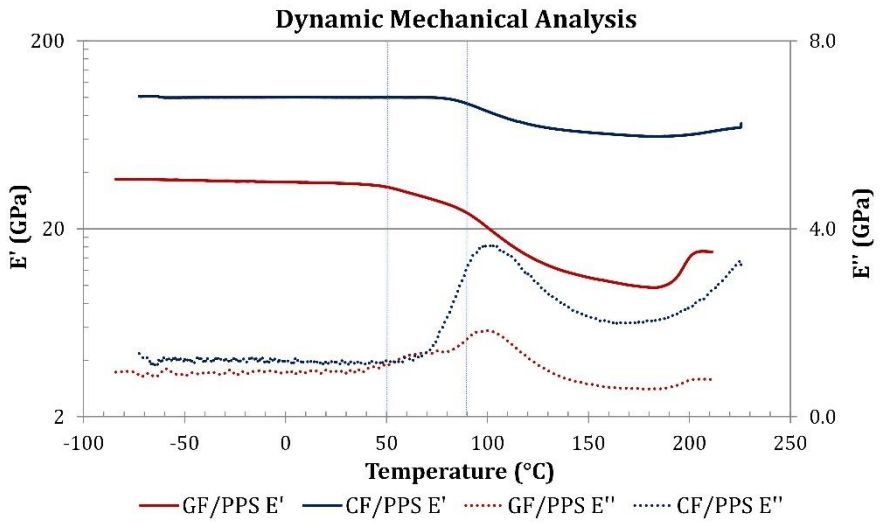

Figure 6.2. Comparison of DMA curves of GF/PPS and CF/PPS. The vertical dashed lines highlight the temperature region between 50 °C and 90 °C.

Using the results from the work of Rohart et al [4] on resistance welding of CF/PPS laminates, a preliminary comparison between resistance welding and ultrasonic welding can also be made. Table 6.2 shows that the LSS of UW CF/PPS joints was higher than the LSS of RW CF/PPS joints at room temperature and at elevated temperatures up to 70 °C. At 90 °C and above, the comparison shows that only the annealed series (ANN_F) had a clearly higher LSS than the LSS of RWCF. The LSS ratio between RWCF and ANN_F at 90 °C and 120 °C was around 0.7. The ratio between RWCF and ASW_F at 90 °C was 1.25 while at 120 °C it was 1.0, most likely due to the cold crystallization of PPS at 120 °C. The ratio between RWCF and ASW_S at 90 °C was 0.96 while at 120 °C it was 0.83. These results indicate that at temperatures at and above 90 °C the mechanical performance of ultrasonically welded CF/PPS joints is not superior than the mechanical performance of resistance welded CF/PPS joints unless the processing conditions account for obtaining a semi-crystalline weldline structure.

Taking into account the failure mechanism of the RWCF joints (i.e. heating element/matrix interface), it can be argued that the RWCF could potentially have a higher LSS if the connection between the stainless steel mesh and the PPS matrix became stronger. This could be the main reason for the lower LSS compared to the UW CF/PPS joints. Further evidence supporting this argument may lie in the findings of a more recent study by Rohart et al [5]. In this study, the adhesion between the stainless steel heating element and the PPS matrix in resistance welding

of CF/PPS was improved by surface modification and evaluated by single lap shear tests at room temperature. The LSS of RW CF/PPS joints increased substantially, reaching similar or higher levels than the LSS of UW CF/PPS joints presented in chapter 5. The surface treatment of the heating element also resulted in changes in failure mechanisms: fibre remnants were seen on the heating element, indicating that the failure occurred within the adherends and not exclusively at the interface of the non-treated heating element with the matrix.

In both welding methods, resistance and ultrasonic, the weldline structure played an important role in the mechanical performance of the welds. Optimizing the process parameters can result in weldlines of desired properties, for example, a weldline consisting of amorphous matrix for higher ductility and toughness. Both welding methods seem to face certain challenges in controlling the weldline structure. In the case of ultrasonic welding the processing window that allows modification of the material structure without any post-welding treatment is relatively narrow. In resistance welding, surface treatment of the heating element is required to increase the interfacial strength between the heating element and the matrix. Obviously, the choice of the fibre-matrix system is critical as the difference between the LSS of GF/PEI and GF/PPS resistance welded joints shows. A final remark on the comparison between resistance welding and ultrasonic welding would be that the presence of a foreign material at the weldline of the former adds complexity to the process. While literature studies have shown that it is possible to solve problems such as current leakage by insulating the heating element [6] and lower strength via modifying the heating element [5], all these solutions are additional steps in the manufacturing process. Hence, the total manufacturing time of resistance welded joints will increase whilst ultrasonic welding remains a much faster process. Taking into account the narrow, but still effective, processing window that allows better control of the final properties, it seems that ultrasonic welding could be a more attractive technique once the continuous ultrasonic welding process becomes an industrial reality.

Bibliography

[1] Villegas IF. Strength development versus process data in ultrasonic welding of thermoplastic composites with flat energy directors and its application to the definition of optimum processing parameters. Composites: Part A 2014; 65: 27-37.

[2] Shi H, Villegas IF, and H.E.N. Bersee HEN. Strength and failure modes in resistance welded thermoplastic composite joints: Effect of fibre-matrix adhesion and fibre orientation. Composites: Part A 2013; 55: 1-10.

[3] Dubé M, Hubert P, Gallet JNAH, Stavrov D, Bersee HEN, Yousefpour A. Metal mesh heating element size effect in resistance welding of thermoplastic composites. Journal of Composite Materials 2011; 46(8): 911-919.

[4] Rohart V, Dubé M, Laberge Lebel L. Effects of temperature on the apparent lap shear strength of resistance-welded carbon fibre/thermoplastic composite joints. In: International SAMPE technical conference 2018-May; 1-10.

[5] Rohart V, Lebel LL, Dube M. Improved adhesion between stainless steel heating element and PPS polymer in resistance welding of thermoplastic composites. Composites Part B 2020; 188: 107876.

[6] Dubé M, Hubert P, Yousefpour A, Denault J. Current leakage prevention in resistance welding of carbon fibre reinforced thermoplastics. Composites Science and Technology 2008; 68: 1579-1587.

7 Conclusions & Recommendations

If I have seen further it is by standing on the shoulders of giants.

(Isaac Newton)

This last chapter summarises the main conclusions of this research, and presents the author's recommendations for future work. The primary objective of this thesis was to gain a comprehensive and in-depth understanding of the behaviour of TPCs welded joints at low and high temperatures. This study was carried out exclusively on resistance welded GF/PPS joints and ultrasonically welded CF/PPS joints, and a fully experimental approach through thermal, mechanical and micrographic analysis was followed. The weld strength at all temperatures was quantified through single lap shear tests. The crystallinity degree of PPS at the weldline of ultrasonically welded CF/PPS joints was thoroughly characterized through direct and indirect measurements. As a result, a qualitative relationship between the weld strength, the failure mechanisms and the constituents of the joints, namely the fibres, the thermoplastic matrix and the weldline was established. This thesis helped to better understand the roles of the weldline and the adherends in the weld performance and to examine the impact of the weldline structure on the temperature performance of TPCs welded joints.

7.1 Conclusions

This section is divided into three sub-sections which detail the conclusions drawn for:

(i) the temperature effects on the mechanical performance of resistance welded GF/PPS joints

(ii) the effect of the ultrasonic welding process on the physical state of PPS in the weldline and in the adherends of CF/PPS joints

(iii) the temperature effects on the mechanical performance of ultrasonically welded CF/PPS joints and their correlation to the crystallinity degree of PPS at the weldline.

7.1.1 Temperature effects on the performance of RW GF/PPS joints

The influence of temperature on the strength and failure mechanisms of RW GF/PPS joints was investigated and presented in Chapter 2. Special focus was given to the connection between the stainless steel mesh and the PPS matrix in an attempt to identify whether the mesh/matrix connection at the weldline was the weakest link at elevated temperatures.

The weld strength was evaluated via single lap shear tests carried out at a wide range of temperatures, the lowest being -50 °C and the highest being 150 °C. The highest LSS was observed at -50 °C, it being 28% higher than the LSS at room temperature, while the lowest LSS was observed at 150 °C, around 35% lower than the LSS at room temperature. The outcome of the single lap shear tests was an overall decreasing trend of LSS with increasing temperature, with the exception of the region between 50 °C and 90 °C, where the weld strength remained virtually constant.

The detailed fractographic analysis showed that the primary microscopic failure features were fibres with very little or no matrix remnants on their surfaces. This failure mechanism was classified as fibre/matrix debonding and was observed at all temperatures. Taking into consideration the decrease in IPS strength with increasing temperature, it is suggested that the fibre/matrix interfacial strength was the main factor affecting the strength of the RW GF/PPS joints at all temperatures. The weakening of the fibre/matrix interface at increasing temperatures was mainly attributed to the reduction in the residual compressive stresses formed between the glass fibres and the PPS matrix. The residual compressive stresses are directly proportional to the ΔT between the stress-free temperature (i.e. melt-crystallization temperature) and the testing temperature, thus, an increase in the testing temperature could be expected to cause a decrease in the stresses. Similarly, the residual compressive stresses are directly proportional to the elastic modulus of the matrix; this dependency had a profound effect on the LSS at temperatures above the glass transition temperature (Tg=103 °C) where the matrix modulus decreased significantly. It was also concluded that the connection between the stainless steel mesh and the PPS matrix was not the weakest link at the weldline of RW GF/PPS joints at any of the temperatures under study.

With regard to the fairly constant LSS in the temperature region between 50 °C and 90 °C, the stress state at the overlap was considered as a potential cause. It is suggested that the stresses could have been distributed over a larger area due to the reduction in IPS modulus, lowering the shear stress concentrations. This phenomenon could have acted as a competing mechanism against the reduction in fibre/matrix interfacial strength, resulting in the fairly constant LSS between 50 °C and 90 °C.

7.1.2 Effect of ultrasonic welding process parameters on the crystallinity degree of PPS

The impact of the ultrasonic welding process on the physical state of PPS in the weldline and adherends of CF/PPS joints was investigated in chapters 3 and 4. The study took into consideration two process parameters, the welding force and the vibration amplitude. Chapter 3 presented DSC and WAXD measurements carried out on ED films removed from the weldline, evaluating the crystallinity degree and crystal perfection of PPS. The temperature profile at the centre of the joint overlap during ultrasonic welding was also measured, allowing for the cooling rates to be calculated. Furthermore, in order to determine the cooling rate dependency of PPS crystallization, FSC measurements were performed. In chapter 4, the crystalline states of PPS in the weldline and in the adherends were evaluated, in order to confirm the findings of chapter 3 and to identify the size of the HAZ, respectively. For this purpose, the nanoindentation technique was employed to measure the modulus and hardness of PPS in the weldline and in the adherends of the CF/PPS welded joints. In addition, the nanoindentation technique was evaluated as a potential characterisation technique for thermoplastic composites welded joints.

The results of this study demonstrated that low welding force (300 N) and low vibration amplitude (51.8 μm) resulted in higher modulus, hardness and crystallinity degree at the weldline of CF/PPS welded joints as compared to high welding force (1000 and 1500 N) and high vibration amplitude (86.2 μm) which, instead, resulted in predominantly amorphous PPS at the weldline. A welding force of 300 N and a vibration amplitude of 51.8 μm were capable of yielding PPS of moderate crystallinity, as well as higher PPS crystal perfection, and resulted in lower cooling rates (around 17 °C/s) than the cooling rates under high welding force and high vibration amplitude (higher than 41 °C/s). However, the FSC measurements showed that the crystallization of PPS, in quiescent conditions, was suppressed at a cooling rate equal to 20 °C/s, exhibiting a degree of crystallinity of only 0.5%. This result was not in line with the DSC and WAXD measurements on the weldline matrix. After carefully considering a few potential factors that could cause this discrepancy, it was suggested that the capability of PPS to crystallize despite the very high cooling rates (at least 17 °C/s), could be attributed to strain-induced crystallization. The significantly high strain rates occurring during ultrasonic welding could orient the molecular chains in the melt, favouring the formation of nuclei and, ultimately, accelerate PPS crystallization. Despite the even higher strain rates encountered in samples welded under high vibration amplitude, PPS was predominantly amorphous, most likely because of the much shorter time available for the molecular chains to orient and form crystals. In conclusion, it was demonstrated that by appropriately modifying the welding force and the vibration amplitude it is possible to obtain a semi-crystalline matrix at the weldline.

The elastic modulus and hardness of PPS in the adherends of the slow processed samples (i.e. samples welded under low force and low vibration amplitude) were virtually the same as the ones in the weldline. On the contrary, in all fast processed samples (i.e. samples welded under high force and high vibration amplitude) the weldline modulus and hardness were significantly lower than the ones in the adherends. With regard to the size of the HAZ it was found that in most samples the PPS elastic modulus remained fairly constant through the thickness of the adherends, while the PPS hardness exhibited a gradual, but not significant, increase away from the weldline. In most samples, the relative differences in PPS hardness between adjacent composite plies (1st – 3rd plies) could reach up to 9%. However, deeper in the laminate (3rd – 5th plies) the PPS hardness remained fairly constant. On these grounds, it remains unclear whether a limited HAZ or slow cooling rates inside the adherends allowing enough time for crystallization to occur, were causing the stable modulus and hardness.

Hence, a definite conclusion regarding the true extent of the HAZ could not be drawn from these results.

The evidence presented in chapter 4, suggested that the nanoindentation technique should be used with caution in the evaluation of anisotropic materials, especially of fibre reinforced polymers. The presence of fibres in the vicinity of the indentations could artificially enhance the local stiffness of the matrix while the typical gradient in material properties such as the interphase between the fibres and the bulk matrix, could add to the uncertainty and scatter of the measurements. As a result, it becomes difficult to determine whether a property has been influenced by the welding process or not. In conclusion, it is suggested to use nanoindentation only for the qualitative and comparative evaluation of modulus, hardness and crystallinity.

7.1.3 Thermal effects on the performance of UW CF/PPS joints: How do they correlate to the crystallinity degree of PPS at the weldline

The mechanical performance of UW CF/PPS joints at temperatures ranging from -50 °C to 120 °C was investigated and the results were presented in chapter 5. The main objective of this study was to correlate the mechanical performance to the crystallinity degree of PPS at the weldline which was accomplished by studying three series of welded joints, all of different weldline crystallinities. The first two series were as-welded joints (i.e. welded joints without any post-welding treatment): one with amorphous weldline (produced under 1000 N and 86.2 μm) and one with semi-crystalline weldline (produced under 300 N and 51.8 μm). The third series was produced by annealing as-welded joints that had amorphous weldline to obtain the weldline with the highest possible crystallinity degree among the three series. The weld strength was assessed through single lap shear tests accompanied with a detailed fractographic inspection which elucidated the failure mechanisms. A strong correlation between the crystallinity degree of PPS in the weldline and the weld performance was eventually established, a correlation supported by the findings of chapters 3 and 4 and complemented by additional thermal testing.

The strength of the UW CF/PPS joints showed an overall decreasing trend with increasing temperature, with the exception of two temperature regions, -50 °C to 50 °C for the annealed series, and 90 °C to 120 °C for the two as-welded series where the LSS remained virtually constant. The highest LSS at all temperatures was measured at -50 °C, for the as-welded joints with amorphous weldline, which was found to be 26% higher than the LSS of the annealed joints and 14% higher than the LSS of the as-welded series with semi-crystalline weldline. The microscopic failure features at -50 °C were fibres mainly or partially covered with residual matrix, indicating matrix failure as the main failure mechanism. On the contrary, at 120 °C the LSS of both as-welded series were lower than the LSS of the annealed series, 28% and 13% for the as-welded joints with amorphous and semi-crystalline weldline, respectively. The microscopic failure features of all specimens as 120 °C were fibres with little or no residual matrix on their surfaces, indicating fibre/matrix debonding.

Overall, at and above room temperature, fibre/matrix debonding was found to be the main failure mechanism in both as-welded series, a failure mechanism that became more pronounced with increasing temperature, especially above the glass transition temperature. The fibre/matrix debonding and its relation to temperature is connected to the residual compressive stresses in the same manner as in the case of the RW GF/PPS joints. The increase in testing temperature most likely partially relieved the residual compressive stresses formed during cooling between the fibres and the matrix. Above the Tg, the drop in the matrix modulus was dramatic and contributed to the further decrease in LSS. The annealed series

exhibited cohesive failure in all specimens at all temperatures, although with increasing temperature fibre/matrix debonding became more pronounced, especially at 120 °C where it was extensive. The cohesive failure was a consequence of porosity at the weldline which was formed during the annealing process.

Higher degree of crystallinity of PPS at the weldline was proved to be advantageous at high temperatures (90 °C and 120 °C). In comparison with amorphous PPS, the semi-crystalline PPS has a higher elastic modulus which resulted in higher fibre/matrix interfacial strength. A remarkable observation was the virtually constant LSS at 90 °C and 120 °C for both as-welded series. This result was attributed to the cold crystallization of PPS at 120 °C which would increase the crystallinity and the elastic modulus of PPS and, ultimately, cause the LSS of both as-welded joints to remain virtually constant. On the contrary, at -50 °C the amorphous weldline was proven to be more beneficial, most likely due to the higher toughness and ductility of amorphous PPS compared to semi-crystalline PPS.

The findings of this study showed that both physical states – amorphous and semi-crystalline – of PPS at the weldline can be advantageous for the mechanical performance of UW CF/PPS joints in dry conditions, depending on the service temperature. In essence, an amorphous PPS weldline could be preferable as long as the operational temperature remained below the glass transition temperature, due to its superior performance at low temperatures. It is important to clarify, though, that the above statement refers exclusively to welded joints tested in dry conditions and not exposed to moisture or any chemical environments. The presence of chemicals such as hydraulic fluid, fuel, and de-icing fluid could potentially compromise the mechanical performance of welded joints with amorphous weldline more than with semi-crystalline weldline.

A final conclusion of this thesis, taking a more holistic approach, is drawn from the comparison between the weld performance of resistance welded GF/PPS joints and of ultrasonically welded CF/PPS joints within the same temperature range (-50 °C to 120 °C). The findings of chapter 2 and chapter 5 were thoroughly discussed in chapter 6. The LSS of all ultrasonically welded CF/PPS joints, either with amorphous or with semi-crystalline weldline, was consistently higher than the LSS of resistance welded GF/PPS joints, at all temperatures. Considering the similar failure mechanisms in both types of welded joints (fibre/matrix debonding), it was suggested that the interfacial strength between the carbon fibres and PPS matrix was higher than the interfacial strength between the glass fibres and PPS matrix. Moreover, it was also suggested that at 90°C and above, the significant reduction in the elastic modulus of the matrix dictated the interfacial strength in both composite systems, reducing the differences between the LSS of the two types of welds.

7.2 Recommendations

In this study the focus was on the thermal effects on the strength and failure mechanisms of RW GF/PPS joints and UW CF/PPS joints. A big part of the study was also dedicated to the influence of ultrasonic welding process on the degree of crystallinity of PPS and its impact on the weld performance. Clearly, no PhD research can cover an entire area of interest and while a PhD research can, sometimes, answer every initial research question, it will inevitably lead to unanticipated findings and generate new questions that would require further investigation. This section provides some recommendations for future research by taking into consideration the unanswered questions, the limitations of this study and the general need for improvements in material and weld performance. The recommendations are focused on three research areas: Mechanical Performance, Durability, and Methodology. The recommendations for future research focus on GF/PPS and CF/PPS welded joints as a direct continuation of this thesis. Nevertheless, it is important to note that the current study and the following recommendations can be extended to other thermoplastics as well such as PEEK, PEKK and PEI.

7.2.1 Mechanical Performance

The term "mechanical performance" refers to static mechanical properties of welded joints. The recommendations below arose from the findings and limitations of this study.

- One of the conclusions of this PhD thesis was that the weld strength of RW GF/PPS joints and UW CF/PPS joints were both governed by the fibre/matrix interfacial strength. Considering the much higher LSS of the latter, an improvement of the GF/PPS interfacial strength could lead to a higher LSS. This can be achieved either by applying fibre sizing of higher compatibility with PPS or by surface treatment of the glass fibres which could, potentially, enhance the mechanical interlocking of the matrix around the fibres. This future research should mainly focus on increasing the GF/PPS interfacial strength which could be evaluated on fibre level (e.g. fibre pull-out tests), laminate level (e.g. in-plane shear tests) and welded joint level (e.g. single lap shear tests).

- The stress distributions at the overlap of thermoplastic composites welded joints should also be investigated to better understand the relationship between the shear and peel stress distributions with the weld strength and failure mechanisms. This future research should be extended to a wide range of temperatures – not only room temperature – in order to complement the findings of this thesis. Furthermore, it is recommended to study the stress distributions using both experimental means such as Digital Image Correlation (DIC) and numerical means such as Finite Element Method (FEM).

- Annealing of UW joints was capable of increasing the crystallinity degree and the elastic modulus of PPS. As a result, the weld strength at 90°C and 120°C increased compared to non-annealed welded joints. A further investigation of the annealing effect focusing on three aspects could be carried out in a further research: First, the morphology of annealed PPS in terms of crystallinity, average crystallite size distribution and lamellar thickness. Second, the optimum set of annealing parameters (time, temperature and pressure). Third, the mechanism governing the void formation (i.e. the causes of porosity) and methods of eliminating them.

- The physical state of the matrix could also be altered by controlling the cooling rates at the weldline. This could be achieved, potentially, by heating up the adherends during the solidification phase of the ultrasonic welding process, making the heat transfer through the laminate less effective. This future research could focus on the processing part by developing a method and/or a customised jig to control the cooling rates, and on the material part by evaluating the physical state of the matrix and the weld strength.

7.2.2 Durability

- Typically, a PhD research should be extended to new fields aiming towards a complete understanding of static, dynamic and long-term behaviours. Properties of polymer composites such as creep and fatigue are very important and not well-understood yet, with many researchers around the globe working experimentally and numerically on these topics. For thermoplastic composites welded joints there is not much research published on creep and fatigue. Evidently, future work should investigate creep and fatigue of thermoplastic composites welded joints. As a direct continuation of this work and taking into account the effect of ultrasonic welding process parameters on the physical state of the matrix, the author recommends the investigation of the creep resistance of UW CF/PPS joints. The focus of the proposed research should be on both amorphous and semi-crystalline weldline, as the creep resistance can be affected by the physical state and the elastic modulus of the matrix.

- Another research topic worthy of investigation, is the chemical resistance of thermoplastic composites welded joints. Clearly, there is no way to perform a complete assessment of chemical resistance and compatibility of thermoplastic composites welded joints. It is an application-dependent and material-dependent research. Strictly speaking about aviation, fluids such as hydraulic fluid, de-icing fluid, and fuel, could be included in an extensive experimental programme on chemical resistance. During this PhD research, some experiments on the chemical resistance of UW CF/PPS joints were carried out using hydraulic fluid and an acidic mixture of hydraulic fluid with water. The preliminary, but unpublished, results indicated a potential dependency of the weld performance on the acidic mixture. No clear trend with crystallinity was observed, however, further investigation is required and together with an improved methodology, it could lead to conclusive and unambiguous results. This research could be combined with the research on creep resistance of UW CF/PPS joints since in real-life applications there is a combination of various factors influencing the material performance.

7.2.3 Methodology

As an experimental study, this work relied on the appropriate selection and application of test methods. Some of the limitations of this study stemmed from not using the most effective technique or from not modifying the technique accordingly. The following recommendations are presented:

- In this study, WAXD was employed to evaluate the morphology of PPS. Although an efficient and reliable technique, WAXD can only provide an estimation of the crystal size. As an alternative, small-angle X-ray scattering (SAXS) could be used as it can effectively measure the average crystalline lamellae thickness. In addition, the FSC

should be further employed in order to (i) examine in detail the PPS crystallization kinetics and (ii) evaluate the dependency of PPS crystallinity on non-constant cooling rates like the ones measured during ultrasonic welding. In such way, a complete assessment of the morphology of the matrix can be achieved.

- It was not possible to reach definite conclusions about the extent of the HAZ area in UW CF/PPS joints due to the lack of unambiguous evidence. Identifying the size of the HAZ will provide valuable information on how the ultrasonic welding process affects the adherends. Temperature measurements at locations of resin rich areas inside the adherends would allow for the measurement of the maximum temperature and the calculation of cooling rates. These experiments will require meticulous preparation in order to embed temperature sensors in the laminate prior to welding and to isolate them to eliminate any interactions with the carbon fibres. The morphology of the matrix in the resin rich areas of the adherends should also be studied in order to detect any morphological changes induced by the ultrasonic welding process.

Acknowledgments

This page is intentionally left blank.

The journey essentially started in 2012 when some of my colleagues at DSM encouraged me to do a PhD. To this day, I am sure they meant it as a compliment... On October 2013, I took the liberty to contact the secretary of the Group, Mrs. Gemma van der Windt and asked her to forward my details to the staff members. A few weeks later, Dr. Irene Fernandez Villegas emailed me saying that she would like to have an interview with me for a PhD position she had available. And a few months later I moved to Delft.

The first person I would like to thank is my daily supervisor, Irene. Thank you so much for offering me this role, giving me the opportunity to do a PhD at TU Delft. I did not know much about welding, I certainly learnt much more and I can ensure you that I will always be promoting welding as the joining method of thermoplastic composites. Thank you for being enthusiastic and for always willing to help me when I was stuck. Either by giving good ideas or by encouraging me to continue. Next to you I learnt how to do research in a more structured way and I also learnt how to write scientific articles. I wish I could say the same things about Yoga, but I guess I will have to try Yoga first...

To my promotor, Prof. Dr. Rinze Benedictus, thank you for giving me the opportunity to do a PhD at TU Delft. To my second supervisor, Dr. Roger Groves, thank you for supporting my work during the first couple of years, and for taking the time to thoroughly check my thesis and ensuring that the quality of my work would meet the Department's requirements and expectations.

To the person who supported every PhD candidate from day -100 to day +1500, Gemma, thank you for forwarding my email, giving me the chance to reach the department. Thank you for arranging my stay at DUWO for the first four months even in such a short notice. Thank you for always being there, helping all of us and providing us with the necessary and more.

I would like to thank the staff members, the technicians and the secretary of ASML. Special thanks to Gertjannis Mulder for not only being a great help in the lab for four years, but also for being a great guy to work with and creating a nice atmosphere in the lab. Kudos to Berthil Grasshof for being the calm force in the lab, and providing solutions to any sort of problems. Whatever the problem was. You deserve an honorary PhD. Frans, thank you so much for all the help with all kinds of equipment, from the microscopes to the thermal analysis instruments, from the diamond saw (that made my clothes black) to the polisher (that made the surfaces even rougher). I hope you are enjoying your time in Portugal, speaking with riddles to the locals. Johan Bijleveld, thank you for helping me in the chemical lab and giving me enough space to work and perform my experiments.

I would like to express my gratitude to Dr Nicolas Boyard and his PhD student, Juliana Amirdine for hosting me in the University of Nantes for five days. Thank you for guiding me with the Flash DSC experiments. I spent five wonderful days there and produced valuable work. Also thank you for assisting me with processing the data and with publishing my second journal paper. I would also like to thank Ben Norder, in Applied Sciences, who performed the XRD experiments and discussed the results with me. I am also very grateful to Dr. Branko Savija, Group of Materials and Environment, Faculty of Civil Engineering, for performing the nanoindentation tests with me and always trying to find an available timeslot for my experiments.

During my time as an office member of SIC, I met with many people from all over the world. Thank you all for creating a nice work environment. To Fabricio, Maria, Maruti, Prem and Hari, thank you for the great fun after work, especially at Atmosfeer, Doerak and Locus. Special thanks to my office mates: Daniel, Wandong, Pedro André Viegas Ochôa de Carvalho,

Freek, Hongwei Quan (who?), Nakash, Morteza, Davide and Chirag who did not have his own desk but was always there. You made the office environment a much better place to work, I enjoyed our serious or not discussions, had lots of fun every time there was a demonstration of a peculiar behaviour and you always helped whenever I had a problem or a serious question. Wandong you are my bro, thank you so much for tolerating my jokes and annoying comments, and for essentially creating "The Board". I'm sure you are the nicest guy in your current office. Pedro, I feel very lucky for having you as my office mate and becoming your friend. I tremendously miss your impersonations of our colleagues, and our political/philosophical discussions. I also want to thank you and Jildou for translating my propositions. John Wayne aka the artist formerly known as Hongwei Quan, thank you for being yourself, an endless source of inspiration. You are a nice person and a great guy to be around!

My gratitude is also shown to the Welding Group members for all their help and contribution during my PhD, especially with the temperature measurements (of chapter 3). Huajie, thank you for teaching me how to manufacture the laminates, how to use the resistance welding machine and for discussing with me my first experiments. Gen, thanks for providing support whenever needed, for taking care of the polishing equipment, and for helping me with the temperature measurements. Bram, thank you for translating the summary of my thesis. I am also grateful to the NovAMers for always supporting me whenever I asked for assistance. Vincenzo and Giacomo thank you for performing a couple of tests at a time I could not be physically present, I highly appreciate it!

Lucas, we both know that you didn't help much during my time at TU, however, you surely did help me afterwards. Thank you for recommending me to – still at the time – AOG back in 2018 and helping me get my current job. Although you probably caused a delay in my PhD so I shouldn't be thanking you, I want you to know that I am grateful for opening a (back) door for me. And I know you never open a back door to anyone...

David, thanks for guiding me through the PhD application process and for welcoming me to Delft, making my transition from Zwolle to Delft a very smooth one.

To Alexandre, my manager at Strohm, thank you so much for understanding my struggles, and making me feel comfortable when I needed to take some extra time to work on my thesis.

Didem, sevdiğim, thank you so much for being there for me, for listening to my frustrations and my occasional rants about train delays, for your delicious cooking, for selecting the softest cat, for your unconditional love, for checking my propositions, for designing the book cover, and for editing this paragraph. You know you've changed my life and made it complete and that between you and me I have the better deal... Σε αγαπώ κοριτσάκι...

To my family, I want to express my gratitude for providing me with your love, care and support throughout the years. Your contribution cannot be measured, only appreciated.

Nikos

Curriculum Vitae

Nikolaos Koutras

The author was born in the previous century, in the city of Patra, Greece, which is located on the northwestern coast of Peloponnese. The exact year remains unknown, however, the month was March, Greece was already a member of the EU (EEC), the O-rings of the Challenger had not failed yet, Germany was still divided, and Nelson Mandela was still in prison.

After a short but successful career during his teenage years at his father's shop, he moved to Athens to study at the Faculty of Applied Mathematical and Physical Sciences at the National Technical University of Athens (NTUA). After the first two weeks he realised that mathematics was no longer his favourite subject as he thought it was for 12 years. Physics was the next best thing, therefore, he selected Physics of Materials, and Optoelectronics as the two tracks to obtain his degree (which is a Diploma, equal to MSc outside Greece and not equal to MSc in Greece, no explanation provided). His thesis was on the study of thermal transitions in polymer nanocomposites containing multi-walled carbon nanotubes. That thesis was the turning point as he developed a genuine interest in Polymer Science.

He expanded his knowledge by obtaining an MSc in Polymers and Polymer Composites Science and Engineering from the University of Sheffield. His thesis was on friction and wear of polymers sliding on steel surfaces.

In 2010 he moved to The Netherlands, to work for DSM Composites Resins, in Zwolle. He spent three years working as an Associate Scientist, primarily on two projects: the development of high performance resins for automotive structural parts and the development of composite sandwich panels for a 45ft lightweight container.

In 2013 he decided to try his luck doing a PhD. Luckily, the opportunity arose and in February 2014 he started his PhD at the Faculty of Aerospace Engineering, in the Group of Structural Integrity & Composites.

Since September 2018 he is working for Strohm as a Materials Development Engineer.

List of publications

Journal Papers

3. **Koutras N**, Villegas IF, Benedictus R. Thermal effects on the performance of ultrasonically welded CF/PPS joints and its correlation to the degree of crystallinity at the weldline. Under review at the journal *Composites Part C*.
2. **Koutras N**, Amirdine J, Boyard N, Villegas IF, Benedictus R. Characterisation of crystallinity at the interface of ultrasonically welded carbon fibre PPS joints. *Composites: Part A* 2019; 125: 105574.
1. **Koutras N**, Villegas IF, Benedictus R. Influence of temperature on the strength of resistance welded glass fibre reinforced PPS joints. *Composites: Part A* 2018; 105: 57-67.

Conference Papers

2. **Koutras N**, Villegas IF, Benedictus R. Effect of ultrasonic welding process on the crystallinity at the welding interface of CF/PPS joints. Paper presented at: *18th European Conference on Composite Materials (ECCM18)*, 24-28 June 2018, Athens, Greece.
1. **Koutras N**, Villegas IF, Benedictus R. Influence of temperature on strength and failure mechanisms of resistance welded thermoplastic composites joints. Paper presented at: *20th International Conference on Composite Materials (ICCM20),* 19-24 July 2015, Copenhagen, Denmark.